Thesis

Interplay of Superconductivity and Spin Texture: application to spintronics and topological states

Rina Takashima

Department of Physics, Kyoto University

December, 2017

Abstract

Recently, the interplay between superconductivity and magnetism receives renewed interest in an even wider range of fields such as spintronics and topological phases of matter. The progress in these fields is also accelerated by recent experimental advances. For instance, the singlet and triplet superconducting proximity effects inside ferromagnets are experimentally observed. Such Cooper pairs in magnets are promising in the next generation of spintronics, "superconducting spintronics". Furthermore, magnetic adatoms or a nanowire on top of a superconductor experimentally realize the topological phase in superconductors. They can host Majorana fermions, whose non-Abelian statistics can be used for topological quantum computing.

In this thesis, we theoretically explore such interplay and propose applications for spintronics and topological states, especially focusing on the roles of spin textures in magnets, such as a domain wall, skyrmions, and helical orders. We study physics of spin textures intertwined with emergent degrees of freedom in superconductor; such as a superconducting phase and Bogoliubov quasiparticles. A spatial gradient of a superconducting phase describes a supercurrent flow, which is dissipationless, and Bogoliubov quasiparticles have peculiar band structures affected by superconducting pairing correlations.

Firstly, we show how a supercurrent acts on localized moments, and propose spin manipulation realized by a supercurrent. Current-induced spin torques, which can drive a magnetic texture, are of great interest due to its possible applications in spintronics such as magnetic memories. Spin-transfer torques induced by a supercurrent can be energetically efficient, and its controllability can be enhanced by different pairings of Cooper pairs. We show that a triplet supercurrent gives rise to a spin-transfer torque, and it may realize an efficient domain wall manipulation compared to the conventional spin-transfer torques. In the presence of the relativistic spin-orbit coupling in an inversion asymmetric system, a singlet supercurrent can also exert a spin torque. Considering a cubic chiral magnet, we reveal the basic properties of the spin torque, such as the parameters dependence. This torque can be applied to drive the motion of a magnetic skyrmion, a topological spin texture stabilized in cubic chiral magnets.

Secondly, we propose topological states in a chiral magnet with an s-wave pairing. We show that a cubic chiral magnet with the proximity-induced s-wave gap, hosts the Weyl quasiparticles, that is, a linear touching between two nondegenerate Bogoliubov bands. The

Weyl quasiparticles result in the nontrivial thermal response and surface states. We discuss that Weyl quasiparticles feel effective electromagnetic fields raised by a spin texture. Furthermore, the tilt of the Weyl cones can be tuned by the strength of the spin-orbit coupling and doping, and we propose a possible realization of type-II Weyl quasiparticles. Their physical properties are different to the conventional (type I) Weyl quasiparticles.

Thirdly, we show that a supercurrent can induce and control noncollinear spin textures in a correlated metal in proximity to a superconductor. It is known that noncollinear spin textures play a key role to engineer topological superconductors and to generate triplet Cooper pairs. So far, however, little is known about the controllability of noncollinear spin textures in the presence of superconductivity. We show that a supercurrent can lead to phase transitions from a paramagnetic state to noncollinear magnetic phases with helical or vortexlike spin textures.

Finally, we show a future direction of the current topic: quantum effects on spin textures. The spin textures discussed above are mostly classical, and it is also intriguing to study how the quantum mechanics changes the properties and dynamics of spin texture. In this thesis, we study the quantum effect on the magnetic skyrmion. We consider skyrmions in the vicinity of the skyrmion-crystal to ferromagnet phase boundary in two-dimensional magnets. Quantum effects give rise to a new intermediate phase, a quantum liquid phase of skyrmions, in which skyrmions are not spatially localized. We expect that this study opens up new directions to study their interplay and superconducting correlations.

Contents

List of publications **5**

1 Introduction: superconductivity and spin texture **7**

1.1 Overview of the thesis . . . 8
1.2 Cooper pair and Bogoliubov quasiparticle . . . 8
1.3 Spin texture . . . 14
1.4 Spin manipulation . . . 21

2 Spin-transfer torque induced by triplet supercurrent **25**

2.1 Introduction to this chapter . . . 26
2.2 Model . . . 27
2.3 Spin-transfer torque induced by triplet supercurrent . . . 28
2.4 Domain wall dynamics . . . 31
2.5 Summary and discussion . . . 34
2.6 Details . . . 35

3 Chiral magnet in proximity to singlet superconductor **38**

3.1 Introduction to this chapter . . . 39
3.2 Spin-orbit torque induced by supercurrent . . . 40
3.3 Skyrmion manipulation . . . 45
3.4 Weyl Bogoliubov quasiparticles . . . 47
3.5 Summary and discussion . . . 52
3.6 Details . . . 52

4 Generating noncollinear magnetism by supercurrent **56**

4.1 Introduction to this chapter . . . 57
4.2 Model . . . 58
4.3 Magnetic instability . . . 59
4.4 Magnetic phase diagram . . . 62
4.5 Summary and discussion . . . 65

4.6 Details 66

5 Quantum effects on skyrmion texture **69**
5.1 Introduction to this chapter 70
5.2 Single particle excitation in the saturated phase 71
5.3 Many body phase diagram 77
5.4 Summary and discussions 80
5.5 Details 81

6 Conclusion **84**

Acknowledgment **98**

List of publications

Papers related to the thesis

1. R. Takashima, Y. Kato, Y. Yanase, and Y. Motome
   Control of Noncollinear Magnetism by Supercurrent,
   arXiv: 1710.11349

2. R. Takashima, S. Fujimoto, and T. Yokoyama
   Adiabatic and nonadiabatic spin torques induced by a spin-triplet supercurrent,
   Physical Review B **96**, 121203(R) (2017).
   © 2017 The American Physical Society

3. R. Takashima and S. Fujimoto
   Supercurrent-induced skyrmion dynamics and tunable Weyl points in chiral magnet with superconductivity,
   Physical Review B **94**, 235117 (2016).
   © 2016 The American Physical Society

4. R. Takashima, H. Ishizuka, and L. Balents
   Quantum skyrmions in two-dimensional chiral magnets,
   Physical Review B **94**, 134415 (2016).
   © 2016 The American Physical Society

Papers which are not included in the thesis

5. Y. Shiomi, R. Takashima, D. Okuyama, G. Gitgeatpong, P. Piyawongwatthana, K. Matan, T. J. Sato, and E. Saitoh
   Spin Seebeck effect in a polar antiferromagnet α-$Cu_2V_2O_7$,
   Physical Review B **96**, 180414(R) (2017)

6. Y. Shiomi, R. Takashima and E. Saitoh
   Experimental evidence consistent with a magnon Nernst effect in the antiferromagnetic

insulator $MnPS_3$,
Physical Review B **96**, 134425 (2017)

7. R. Takashima and S. Fujimoto
Electrodynamics in Skyrmions Merging,
Journal of the Physics Society of Japan **83**, 054717 (2014)

Chapter 1

Introduction: superconductivity and spin texture

Superconductivity and magnetism are ones of the most interesting phenomena raised by correlations of electrons. The interplay between superconductivity and magnetism has been studied for decades, e.g., Yu-Shiba-Rusinov bound states and superconductors that originate from spin fluctuations. They sometimes mutually exclusive; at other times they show some combined effects that result in exotic phenomena.

Recently their interplay has been studied from new perspectives. One is to utilize superconductivity to spintronics. Superconductors show interesting transport properties and responses, which are different from those in normal systems. It is expected that they might realize new spintronics device. Experimentally, superconducting spin valves, which aim at 'infinite' magnetoresistance, are realized. Furthermore, spin injection and spin Hall effect in superconductors are also observed. Another direction is to engineer Cooper pairing or quasiparticle states by magnetism. With noncollinear magnetic moments, a singlet Cooper pair can be converted to a triplet pair at the interface between a superconductor and a magnet. Furthermore, some classes of topological superconductor can be also engineered by using spin textures.

Given such experimental and theoretical progress, we study physics emerged from the interplay between superconductivity and spin textures in this thesis. We aim to apply it for spintronics and also find new topological phenomena. To begin with, we review the theoretical and experimental backgrounds related to this thesis.

The organization of this chapter is as follows. In Sec. 1.1, we provide the organization of this thesis. In Sec. 1.2, we give an introduction on superconducting pairing and Bogoliubov quasiparticles. In Sec. 1.3, we review spin textures in magnets: a domain wall, a skyrmion, and a multiple-Q order. We also discuss the physical consequences when electrons couple with them. In Sec. 1.4, we give a review on dynamics of magnetic texture and spin torques, which drive a magnetic texture.

1.1 Overview of the thesis

We first overview the contents of this thesis. In Chap. 2, we study how a spin-triplet supercurrent acts on a localized moment. Spin-triplet pairs at the interface between a superconductor and a ferromagnet are experimentally observed in several setups. Since they carry spin, it is interesting to ask how they interact with a spin texture. We calculate spin transfer torques induced by a spin-triplet supercurrent. We show that spin-triplet correlations realize a new type of spin torque, and they can realize nontrivial domain wall dynamics. Related to this study, in this chapter, we give reviews on spin-triplet pairs in Sec. 1.2.2, a theoretical description of a supercurrent in Sec. 1.2.4, a domain wall in Sec.1.3.1, and spin torques in normal metals in Sec. 1.4.3.

In Chap. 3, we show that, in the presence of spin-orbit coupling, a singlet supercurrent can also exert a different type of spin torque. We consider cubic chiral magnets in proximity to an s-wave superconductor. Cubic chiral magnets include $\mathrm{Fe}_x\mathrm{Co}_{1-x}\mathrm{Si}$ and MnSi, where skyrmions are stabilized. We reveal the basic properties of the spin torque and show that this torque can drive a skyrmion motion. Furthermore, we also show that Weyl quasiparticles exist in the Bogoliubov de Gennes (BdG) spectrum in this system. Related to this, we give reviews on BdG quasiparticles and their topological states in Sec. 1.2.3, and a skyrmion in Sec.1.3.2.

In Chap. 4, we demonstrate that a supercurrent induces and controls noncollinear magnetic orders. It is known that a noncollinear spin texture is a key to realize topological superconductors and to generate triplet Cooper pairs as we review in this chapter. We show that a supercurrent leads to phase transitions from a paramagnetic state to noncollinear magnetic phases, such as a single-Q and a double-Q (vortexlike) orders. Related to this, we give a review on multiple-Q orders in Sec. 1.3.3 and the physical consequences of noncollinear orders in Sec. 1.3.4.

Chapter 5 presents a future direction of this thesis. We study quantum effects on a skyrmion and show that they result in a new quantum phase and critical phenomena. We consider magnetic skyrmions in the vicinity of the skyrmion-crystal phase to ferromagnetic phase boundary in two-dimensional magnets. When the size of a skyrmion is small, quantum effects become important. The quantum effects give rise to a new intermediate phase, a quantum liquid phase of skyrmions, in which skyrmions are not spatially localized. We believe that, they will further lead to versatile phenomena by intertwining with superconductivity.

Chapter 6 is dedicated to the conclusion of this thesis. In the remainder of this chapter, we review the theoretical and experimental backgrounds related to this thesis.

1.2 Cooper pair and Bogoliubov quasiparticle

In this section, we give a review on superconducting pairing and Bogoliubov quasiparticles.

1.2.1 Pairing symmetry

Superconductors are characterized by the gap function: $\Delta_{\sigma\sigma'} = \lambda\langle c_{-\boldsymbol{k}\sigma}c_{\boldsymbol{k}\sigma}\rangle$, where λ is the coupling constant for the attractive interaction to form the superconducting order, $c_{\boldsymbol{k}\sigma}$ is the electron operator with momentum $\boldsymbol{k}$ and spin σ. The Pauli principle requires the following form

$$\hat{\Delta}(\boldsymbol{k}) = \begin{pmatrix} \Delta_{\uparrow\uparrow}(\boldsymbol{k}) & \Delta_{\uparrow\downarrow}(\boldsymbol{k}) \\ \Delta_{\downarrow\uparrow}(\boldsymbol{k}) & \Delta_{\downarrow\downarrow}(\boldsymbol{k}) \end{pmatrix}, \tag{1.2.1}$$

$$= i(\psi(\boldsymbol{k}) + \boldsymbol{d}(\boldsymbol{k}) \cdot \boldsymbol{\sigma})\sigma^y, \tag{1.2.2}$$

where $\boldsymbol{\sigma} = (\sigma^x, \sigma^y, \sigma^z)$ denote the pauli matrices in spin space, $\psi(\boldsymbol{k}) = \psi(-\boldsymbol{k})$ parametrizes a singlet even-parity state, and $\boldsymbol{d}(\boldsymbol{k}) = -\boldsymbol{d}(-\boldsymbol{k})$ parametrizes a triplet odd-parity state.

In the presence of inversion symmetry, parity is a quantum number, and hence singlet and triplet components do not mix each other. On the other hand, the lack of inversion symmetry may lead to a mixed-parity state, where both components coexist.

1.2.2 Spin-triplet pairing

The interplay of superconductivity and magnetic moments is important especially with spin-triplet Cooper pairs [1, 2, 3, 4, 5, 6]. Inside a ferromagnet, a triplet Cooper pair shows the long-range proximity effect; triplet pairs can penetrate into the ferromagnet for a much longer distance compared to singlet Cooper pairs. In Chap. 2, considering the proximity effects of triplet pairs, we discuss spin-torques given by triplet pairs in magnets. In the following, we give some examples which have triplet pairs.

Bulk triplet superconductor

The number of triplet superconductors or its candidates is very limited compared to that of singlet superconductors. The superfluid ^{3}He is the oldest example of a triplet superfluid [7]. It has several phases, with different types of orders, e.g., Balian-Werthamer (B) phase and Anderson-Brinkman-Morel (A) phase. Their topological characters are discussed in the next subsection. Sr_2RuO_4 [8] and some uranium-based compounds, such as UPt_3 [9] and UCoGe [10], also have triplet pairing. As for Sr_2RuO_4, the superconducting proximity effect in ferromagnet is observed in a system composed of a ferromagnet Sr_2RuO_3 and Sr_2RuO_4 [11], and the long-range penetration length supports the triplet-nature of the Cooper pairs.

In noncentrosymmetric superconductors, such as $CePt_3Si$ [12] and $CeRhSi_3$ [13], mixed-parity states are considered to be realized. The direction of $\boldsymbol{d}(\boldsymbol{k})$ vector depends strongly on the anti-symmetric spin-orbit (SO) coupling, which is odd under the spatial inversion. It can be written as

$$H_{\rm SOC} = \alpha \sum_{\boldsymbol{k}\sigma\sigma'} \boldsymbol{g}(\boldsymbol{k}) \cdot c^\dagger_{\boldsymbol{k}\sigma} \boldsymbol{\sigma}_{\sigma\sigma'} c_{\boldsymbol{k}\sigma'}, \tag{1.2.3}$$

with an odd function $\boldsymbol{g}(\boldsymbol{k}) = -\boldsymbol{g}(-\boldsymbol{k})$ and the coupling constant α. For instance, in crystals with C_{4v} symmetry, Rashba SO coupling, given by $\boldsymbol{g}(\boldsymbol{k}) = (k_y a, -k_x a, 0)$, is realized around the Γ point, where a is the lattice constant. It is known that $\boldsymbol{d}(\boldsymbol{k})$ vector in parallel to $\boldsymbol{g}(\boldsymbol{k})$ $[\boldsymbol{d}(\boldsymbol{k}) \parallel \boldsymbol{g}(\boldsymbol{k})]$ around the Fermi surface decreases the Ginzburg-Landau free energy [14]. Furthermore, an anti-symmetric SO coupling gives rise to rich physics such as topological superconductors [15], Edelstein effect [16], and the anomalous Hall effect [17].

Spin-triplet pairing at interface

The triplet correlations may be also generated in a finite region at the interface between a singlet-superconductor and a ferromagnet.

At the interface, scattering processes generate Cooper pairs with $(S, S^z) = (1, 0)$ from that with $(S, S^z) = (0, 0)$, where S is the total spin of a Cooper pair and S^z is the spin component in parallel to the magnetization of the ferromagnet. In terms of the symmetry, it can be explained as follows. The spin rotational symmetry is broken down to $U(1)$ due to the ferromagnet, and hence the total spin S of the Cooper pairs are not conserved during scattering processes, while S^z is conserved. Intuitively, electrons of the Cooper pair obtain the spin-dependent phase through scattering under a finite Zeeman splitting, and then the wave function of the Cooper pairs changes.

Triplet correlations with $S_z \neq 0$ can arise through scattering in the presence of non-collinear moments [18] or the spin-orbit coupling [19, 20] (Fig. 1.1). They break the $U(1)$ spin symmetry, and S_z is not conserved in scattering processes. Experimentally, the conversion to the Cooper pairs with $S_z \neq 0$ has been observed as the long-range proximity effect. There are several experiments using fully-spin polarized metals [21, 22] and multilayers with noncollinear magnetic moments [23, 24].

We also note that depending on the disorder of systems, superconducting correlations show different types frequency dependence: even-frequency and odd-frequency pairings. In this thesis, we focus on the equal time pairing, classified as an even-frequency pairing. The details of this topic are beyond the scope of this thesis.

In Chap. 2, we study spin torques given by a triplet supercurrent. One of the possible setups uses the above spin-triplet pairings induced in the interface so that we can use a singlet superconductor with the high H_{c2} and T_c. Also, in Chap. 4, we propose a way to induce noncollinear textures in the presence of superconducting correlation. It can be used to obtain triplet pairings using the above mechanism.

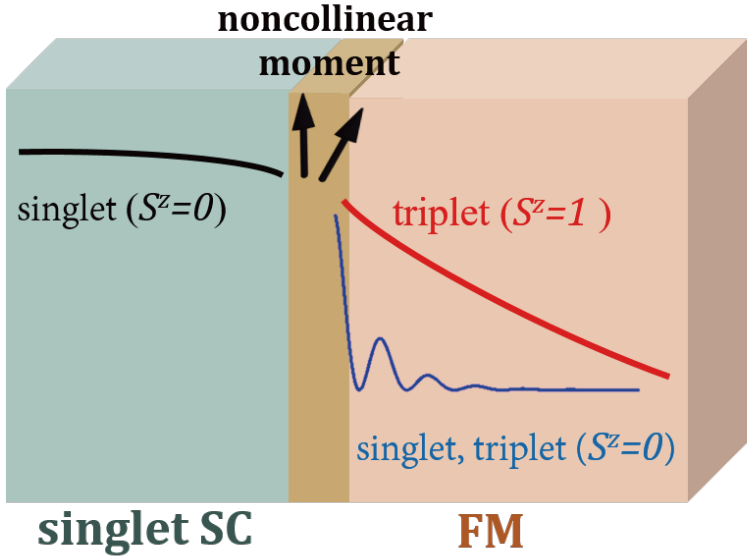

Figure 1.1: Proximity effect of superconductivity in a layered system with a singlet superconductor (SC) and a ferromagnet (FM). A singlet Cooper pair can be converted to a triplet pair with $(S, S^z) = (1, 1)$ in the presence of noncollinear moments.

1.2.3 Topological structure of Bogoliubov quasiparticle

The role of topology in electronic states in solids has been recognized since when the quantized hall conductance is proposed in a two dimensional crystal [25]. The quantized response is the manifestation of the Chern number, the topological invariant defined in the electronic band [26]. In addition to the quantized bulk response, the system hosts the gapless modes localized at the surface or the edge of the system. Later, it was shown that topological classifications are possible for various quantum many-body states with different symmetries. For example, the time reversal symmetry gives a different nontrivial state in two dimensions, the quantum spin Hall insulator [27, 28]. It gives the quantized 'spin' Hall conductance, and the topological invariant takes $\mathbb{Z}_2$ value instead of integer.

Furthermore, we can also classify superconductors by the topological invariants defined in the quasiparticle state [29, 30]. Since the system inherently has the particle-hole symmetry, the topological classifications and properties are different from those in normal systems without the particle-hole symmetry [31, 32]. For example, a chiral p-wave superconductor shows the quantized thermal Hall effect [32] as the manifestation of the topological invariant. Furthermore, it hosts the Majorana fermions as the zero energy state inside a vortex [15, 33]. Majorana fermions show non-Abelian statistics and might be the key to quantum computing. There are many experimental and theoretical efforts on detecting Majorana zero modes.

We also note that topology plays an crucial role not only in fully gapped systems but also in gapless ones. A Weyl semimetal is a gapless system with nontrivial momentum space topology [34, 35, 36]. Two non-degenerate energy bands linearly cross at isolated points in the momentum space (Weyl nodes), and they are the source or sink of the Berry curvature, which is the origin of the anomalous Hall effect. Again, Weyl nodes can be found in Bogoliubov quasiparticle spectrum in superconductors and they are expected to give rise to interesting phenomena.

In this section, we introduce the Bogoliubov quasiparticle to discuss the topological feature of a superconducting state in Chap. 3. Superconducting correlation modifies the quasiparticle spectrum, i.e., it hybridizes the electron and hole bands and open the superconducting gap. The quasiparticle structure can be well captured by the BdG Hamiltonian given by

$$H = \frac{1}{2}\sum_{\boldsymbol{k}} \Psi_{\boldsymbol{k}}^\dagger H(\boldsymbol{k})\Psi_{\boldsymbol{k}} = \frac{1}{2}\sum_{\boldsymbol{k}} \Psi_{\boldsymbol{k}}^\dagger \begin{pmatrix} \hat{H}_N(\boldsymbol{k}) & \hat{\Delta}(\boldsymbol{k}) \\ \hat{\Delta}(\boldsymbol{k})^\dagger & -\hat{H}_N(-\boldsymbol{k})^{\mathrm{T}} \end{pmatrix} \Psi_{\boldsymbol{k}}, \tag{1.2.4}$$

where we define the basis as

$$\Psi_{\boldsymbol{k}} = \begin{pmatrix} c_{\boldsymbol{k}\uparrow} \\ c_{\boldsymbol{k}\downarrow} \\ c_{-\boldsymbol{k}\uparrow}^\dagger \\ c_{-\boldsymbol{k}\downarrow}^\dagger \end{pmatrix}, \tag{1.2.5}$$

and $\hat{H}_N(\boldsymbol{k})$ is the normal part of the Hamiltonian, e.g., $\hat{H}_N(\boldsymbol{k}) = \xi_{\boldsymbol{k}}\mathbb{I}_2$ with the kinetic energy $\xi_{\boldsymbol{k}}$ and $\mathbb{I}_2 = \mathrm{diag}(1, 1)$. The eigenvalues of $H(\boldsymbol{k})$ give the Bogoliubov quasiparticle spectrum.

The BdG Hamiltonian defined in (1.2.4) may give either gapped or gapless band structures. They can realize topological superconductors and Weyl superconductors. Importantly, since the system inherently has the particle-hole symmetry, the topological classifications are different from those in normal systems without the particle-hole symmetry.

In Chap. 3, we discuss the Weyl nodes in the Bogoliubov quasiparticle spectrum. We show how its position and tilting angle depend on the magnetic moment and discuss the physical consequence. Before closing this section, we show some examples of topological superconductors in the following.

Time-reversal-invariant topological superconductor (class DIII) in three dimensions

The spin triplet superfluid ^{3}He-B phase is known to be a three-dimensional (3D) topological superfluid, which is predicted to host gapless helical Majorana fermions on its surface [37]. The superfluid gap is triplet and characterized by $d_\mu(\boldsymbol{k}) = \Delta_B \sum_i R_{\mu i}\hat{k}_i$ with $\hat{k}_i = k_i/|\boldsymbol{k}|$ and a rotational matrix $R_{\mu i}$, e.g., $\boldsymbol{d}(\boldsymbol{k}) = \Delta_B\hat{\boldsymbol{k}}$. The gap amplitude is isotropic in momentum space ($\boldsymbol{d}^*(\boldsymbol{k}) \cdot \boldsymbol{d}(\boldsymbol{k}) = |\Delta_B|^2$).

Time-reversal-breaking topological superconductor in two dimensions (class D)

This category of topological superconductors attracts attention because they host Majorana bound states, which have the non-Abelian statistics and can be applied to topological quantum computing [38].

In one-dimensional (1D) superconductors in class D or class BDI, Majorana zero modes are predicted to appear at the ends of the superconductor [39]. Theoretically proposed setups require the strong spin-orbit coupling with a Zeeman field [40, 41] or helical textures [42, 43, 44, 45, 46]. Many experiments have been conducted with artificially engineered setups, e.g., a semiconducting nanowire [47, 48] or ferromagnetic atomic chains [49] proximitized with a conventional s-wave superconductor.

In two-dimensional (2D) superconductors without the time-reversal symmetry, Majorana zero mode is bound in the vortex core. Also, there is a chiral Majorana edge state. The topological structure can be realized by chiral p-wave ($p + ip$) superconducting pairing. Again, there are many experiments in engineered systems, e.g., the surface of the topological insulator [50] or Rashba-coupled system [51] proximitized with a conventional s-wave superconductor and magnetic field. Theoretically, it is also proposed that a skyrmion texture with the proximity induced singlet superconductivity can realize the topological superconductor in this class [52, 53, 54].

In addition to the engineered systems, the quasi-2D material Sr_2RuO_4 is one of the candidates to realized chiral p-wave superconductivity.

Weyl superconductor

Weyl superconductors have pairs of Weyl points in the BdG spectrum. A Weyl point is a point at which two bands linearly touch, and can be thought of as the sink or source of the Berry curvature in the momentum space [31]. In a superconductor, they are predicted to show the thermal Hall effect and surface Majorana arcs [31, 55].

There are several candidate materials and models that realize Weyl superconductor. ^{3}H-A phase is a Weyl superfluid [31]. The superfluid gap has two points nodes and characterized by $d_\mu(\boldsymbol{k}) = \sum_i d_{\mu i}\hat{k}_i = \Delta_A(\hat{\boldsymbol{d}})_\mu(\hat{\boldsymbol{m}} + i\hat{\boldsymbol{n}})_i$ where $\hat{\boldsymbol{d}}$ is the unit vector that describes the spin state and $\hat{\boldsymbol{m}}, \hat{\boldsymbol{n}}$ ($\hat{\boldsymbol{m}} \perp \hat{\boldsymbol{n}}$) are the unit vectors that describe the orbital state. The point nodes, i.e., Weyl points, appear in the direction of $\hat{\boldsymbol{m}} \times \hat{\boldsymbol{n}}$.

The heavy fermion superconductor URu_2Si_2 [56] is another candidate for the Weyl superconductor. The superconducting gap function is considered to be the singlet $d_{xz} + id_{yz}$ pairing. The gap function is given by $k_z(k_x + ik_y)$ for a small $|\boldsymbol{k}|$, and has point nodes at $k_x = k_y = 0$ and a line-node on the $k_z = 0$ plane.

1.2.4 Supercurrent

The spatial gradient in the phase of the gap functions gives a supercurrent, an equilibrium current. Later, we show that a supercurrent flow interacts with a magnetic moment as a spin torque in Chap. 2 and 3. Furthermore, we demonstrate that a supercurrent induces the instability toward a magnetically ordered state in Chap. 4.

The relation between the spatial gradient in the superconducting phase and a supercurrent can be described as follows. Let us consider a singlet pairing with a spatially dependent phase, given by the following mean field Hamiltonian,

$$H = \sum_{\boldsymbol{k}\sigma} \xi_{\boldsymbol{k}} c^\dagger_{\boldsymbol{k}\sigma} c_{\boldsymbol{k}\sigma} + \frac{1}{2}\sum_i (\Delta e^{2i\boldsymbol{\kappa}\cdot\boldsymbol{r}_i} c^\dagger_{i\uparrow} c^\dagger_{i\downarrow} + \text{H.c.}), \tag{1.2.6}$$

where $c_{i\sigma}$ is the Fourier transform of $c_{\boldsymbol{k}\sigma}$, and $\boldsymbol{\kappa}$ characterizes the spatial gradient of the superconducting phase. For $\xi_{\boldsymbol{k}} = \frac{\hbar^2 k^2}{2m} - \varepsilon_F$, the current density is given by

$$j_\mu \simeq -e\frac{\kappa_\mu}{m}\left(n_e - \frac{4\varepsilon_F}{Td}\frac{1}{L^d}\sum_{\boldsymbol{k}} n_F(E_{\boldsymbol{k}})(1 - n_F(E_{\boldsymbol{k}}))\right), \tag{1.2.7}$$

where $-e < 0$ is the electric charge, and d is the dimension and L is the length of the system, n_e is the electron density, $n_F(x) = (e^x + 1)^{-1}$ is the Fermi-Dirac distribution function, $E_{\boldsymbol{k}} = \sqrt{\xi^2_{\boldsymbol{k}} + |\Delta|^2}$, and T is the temperature with Boltzmann constant $k_B = 1$. $n_s \equiv n_e - \frac{4\varepsilon_F}{Td}\frac{1}{V}\sum_{\boldsymbol{k}} n_F(E_{\boldsymbol{k}})(1 - n_F(E_{\boldsymbol{k}}))$ is called the superfluid density. The second term, the correction to the electron density, vanishes at a low temperature $T \ll |\Delta|$, and hence $n_s \simeq n_e$.

1.3 Spin texture

An ordered state can be characterized by an order parameter. For a superfluid, the oder parameter is a complex scalar, and for an isotropic ferromagnet, it is a vector. An order parameter may have some spatial dependence, e.g., around a defect. Such spatial configuration of order parameters, often called textures, can be classified by using topology [57].

Topological textures are realized in many condensed matter systems [58]. A well-known example is a vortex of a superfluid. It is labeled by an integer winding number. In a ferromagnetic Heisenberg model, the order parameter configuration around a point defect in three dimensions can be nontrivial, e.g., a hedge-hog monopole. In two dimension, there is a topological texture without singularities (defects), which is labeled by an arbitrary integer. It is called a skyrmion in condensed matter physics. Furthermore, in a Heisenberg model with an easy axis anisotropy, a magnetic domain wall is also a topological soliton, which is again labeled by an integer.

The stability of the above textures is ensured by topology; they cannot be removed by continuous deformation. In magnets, a domain wall and a skyrmion are promising information carriers in future magnetic memory such as the race-track memory [59]. Therefore manipulation of spin textures has been studied intensively.

Furthermore, topological textures give interesting physical properties. Due to the topological nature, a magnus force, a force transverse to its velocity, acts on a skyrmion and a vortex, and they show peculiar dynamics [60, 61, 62]. In addition, when electrons couple with a skyrmion, the topological Hall effect occurs, i.e., a skyrmion acts on an electron like a magnetic field [63, 64].

In this section, we give a review on spin textures, a domain wall, a skyrmion, and so-called "multiple-Q" orders. A domain wall and a skyrmion are topological solitons. A multiple-Q order refers to a broader class of magnetic orders, which include a skyrmion crystal (triple-Q order). A multiple-Q order is characterized by multiple wave numbers, unlike a ferromagnetic order or a helical order (single-Q state). We show how such spin textures are realized in magnets. Finally, we also discuss their physical consequences that result from coupling with electrons.

1.3.1 Magnetic domain wall

In ordered magnets, a domain wall appears between two different ground state configurations. Here we study a domain wall in a ferromagnetic Heisenberg model with a uniaxial anisotropy, where a domain wall configuration can be obtained analytically. We consider the Hamiltonian

$$H = -J\sum_{i,j} \boldsymbol{S}_i \cdot \boldsymbol{S}_j - \frac{K}{2}\sum_i S_i^{z2}, \tag{1.3.1}$$

where $J > 0$ and K are the coupling constants for the ferromagnetic interaction and the easy axis anisotropy, and $\boldsymbol{S}_i = (S_i^x, S_i^y, S_i^z)$ is the classical spin at site i. Now we take the continuum limit to study low energy physics in the ferromagnet. The classical Hamiltonian in the continuum limit is

$$\begin{aligned} H &= \frac{S^2}{2}\int \frac{dr^d}{a^d}\left(J\partial_\mu \boldsymbol{n}\cdot\partial_\mu \boldsymbol{n} - Kn^{z2}\right), && (1.3.2)\\ &= \frac{S^2}{2}\int \frac{dr^d}{a^d}\left(J\left((\boldsymbol{\nabla}\theta)^2 + \sin^2\theta(\boldsymbol{\nabla}\phi)^2\right) - K\cos^2\theta\right), && (1.3.3)\end{aligned}$$

where $S\boldsymbol{n}(\boldsymbol{r}) = S(\cos\phi\sin\theta, \sin\phi\sin\theta, \cos\theta)$ is the spin field in the continuous approximation. The ground state configurations are given by $\phi =$ const. and $\theta = n\pi$ with N being an arbitrary integer, and it labels "topological sectors" of vacua. A domain wall exists at the boundary of two different sectors labeled by $N = N_+$ and $N = N_-$, and the topological charge of the domain wall is given by $N_+ - N_-$.

Now we study the static ground state configuration under the boundary condition given by $\theta(x = -\infty) = \pi$ and $\theta(x = +\infty) = 0$. The solution is

$$\cos\theta = \tanh\frac{x - X}{\lambda}, \quad \phi = \phi_0, \tag{1.3.4}$$

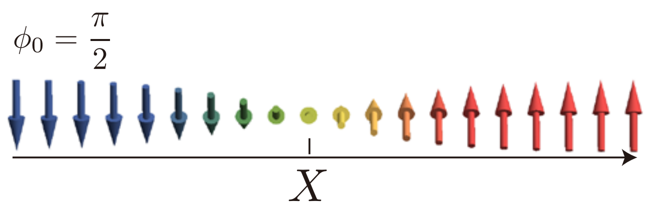

Figure 1.2: A domain wall configuration that centers at $x = X$ with $\phi_0 = \frac{\pi}{2}$, where ϕ_0 is the azimuthal angle of the spin at X.

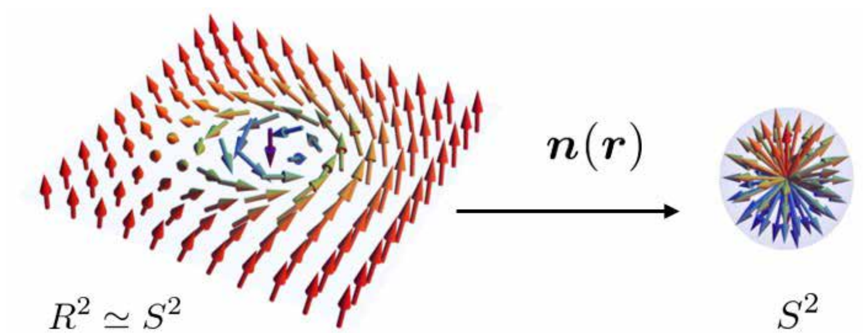

Figure 1.3: A single skyrmion configuration (left), which is defined by the topological number in Eq. (1.3.5).

where $\lambda = \sqrt{\frac{J}{K}}$ and ϕ_0 is an arbitrary angle. With the fixed boundary condition, the domain wall cannot be removed by a smooth deformation. In addition to the topological charge $N_+ - N_- = 1$, ϕ_0 also characterizes a domain wall; a domain wall with $\phi_0 = 0$ is called Neel wall, and one with $\phi_0 = \pm\pi/2$ is called Bloch wall.

1.3.2 Skyrmion

A magnetic skyrmion is a swirling spin texture defined by the topological number. We consider the ferromagnetic Heisenberg model in two dimensions with the boundary condition given by $\boldsymbol{n}(|\boldsymbol{r}| \to \infty) = \boldsymbol{n}_0(\text{const.})$. The spin configuration can be classified by the so-called skyrmion number given by

$$\mathcal{N} = \frac{1}{4\pi} \int d^2x \, \boldsymbol{n} \cdot (\partial_x \boldsymbol{n} \times \partial_y \boldsymbol{n}), \tag{1.3.5}$$

which corresponds to the number of times $\boldsymbol{n}$ wraps around the unit sphere (Fig. 1.3). Again, this number does not change by continuous deformation of $\boldsymbol{n}(\boldsymbol{r})$.

In addition to the topological stability, a skyrmion shows nontrivial dynamics [61, 62]. Furthermore, when electrons couple with a skyrmion texture, the topological Hall effect occurs because of the effective magnetic fields raised by the above topological structure [63, 64].

Let us show the ground state configuration of a skyrmion in the following Hamiltonian

$$H = \frac{JS^2}{2} \int \frac{dr^d}{a^d} \partial_\mu \boldsymbol{n} \cdot \partial_\mu \boldsymbol{n}. \tag{1.3.6}$$

The ground state configuration with $N_{sk} = 1$ under the boundary condition $\boldsymbol{n}(|\boldsymbol{r}| \to \infty) = (0, 0, 1)$ is

$$\boldsymbol{n} = \frac{1}{1 + |u|^2} \left(2\mathrm{Re}(u), 2\mathrm{Im}(u), 1 - |u|^2 \right), \tag{1.3.7}$$

where

$$u = \frac{R}{z - z_1}, \tag{1.3.8}$$

$z = x+iy$, $z_1 = x_1+iy_1$, (x_1, y_1) is the center position of the skyrmion, and R is the parameter characterizing the "radius" of the skyrmion. The energy of this configuration does not depend on the position (x_1, y_1) and R. In addition, there are no interactions between skyrmions in this model. We note that additional terms in the Hamiltonians, such as Dzyaloshinskii-Moriya (DM) interaction and a magnetic field, may give the potential for the radius of a skyrmion and interactions between skyrmions.

Here, we comment on the stability of a skyrmion. Purely topological protection of skyrmions is only valid for the classical and continuous field in the ground state. In other situations, comparison of the energy scales is required to discuss the stability of skyrmions. For example, thermal or quantum fluctuations may cause an abrupt spin flip, which may annihilate skyrmions.

To realize a skyrmion, in most cases, stabilization of spiral spin textures is necessary. In thermodynamically stable states, skyrmions often form a triangular lattice, called a skyrmion crystal (SkX). A simple SkX is described by a superposition of three helices called a triple-Q state, which we describe in the next subsection. In the following, we show several mechanisms that realize skyrmions in magnets. Also, we comment on the size of the skyrmion in each system, because it is an important quantity to discuss the quantum effects in Chap. 5 .

DM interaction

In the metallic chiral magnets MnSi [65], $Fe_{1-x}Co_xSi$ [66, 67], FeGe [68, 69] and $Mn_{1-x}Fe_xGe$ [70] and the insulating chiral magnet Cu_2OSeO_3 [71, 72], skyrmions and SkX are experimentally observed. The above materials are B20 cubic crystals with the same space group $P2_13$, which does not have mirror or inversion symmetry. The chiral crystal structure has the antisymmetric DM interaction, which results in helical states or SkX structures under a magnetic field. In the continuum approximation, the DM interaction is given by

$$H_{\rm DM} = DS^2 \int \frac{dr^2}{a^2} \boldsymbol{n} \cdot (\boldsymbol{\nabla} \times \boldsymbol{n}). \tag{1.3.9}$$

With the Heisenberg term [Eq. 1.3.6], the DM interaction stabilizes a spiral structure with a wave vector $\boldsymbol{Q}$ ($|\boldsymbol{Q}| = 2\pi D/J$). Since DM interaction originates in the relativistic spin-orbit coupling, D tends to be smaller than the symmetric interaction J. Therefore, the size of a skyrmion or the wave length of a helical spin state ($2\pi/Q$) is typically 5-100 nm.

Frustrated spin interaction

There are some frustrated spin models where SkX is stabilized: $J_1 - J_3$ model and $J_1 - J_2$ model on a triangular lattice[73, 74], where the nearest neighbor coupling J_1 is ferromagnetic and the second (third) neighbor coupling J_2 (J_3) is anti-ferromagnetic. The ratio $J_3/|J_1|$ or $J_3/|J_1|$ yields an optimal wave length for a helix, and hence the size of a skyrmion. It can be a few unit lattice length depending on the parameters. Unlike skyrmions in chiral magnets, the energies of a skyrmion with $N_{sk} = \pm 1$ and with different helicity, which characterize how in-plane spins swirl around the core, are degenerated.

As shown in Ref. [74], with the unidirectional anisotropy, a SkX phase appears as a ground state in $J_1 - J_2$ model on a triangular lattice. A single skyrmion or antiskyrmion is stable under a critical field in the fully polarized ferromagnetic state.

Ruderman-Kittel-Kasuya-Yosida interaction

It is theoretically proposed that a SkX is realized in the double exchange model, which describes itinerant electrons that couple with classical localized spins [75]. The model is given by

$$H = \sum_{\boldsymbol{k}\sigma} \xi_{\boldsymbol{k}} c^\dagger_{\boldsymbol{k}\sigma} c_{\boldsymbol{k}\sigma} - J_{\rm sd} S \sum_i \boldsymbol{n}_i \cdot c^\dagger_{i\sigma} \boldsymbol{\sigma}_{\sigma\sigma'} c_{i\sigma'}, \tag{1.3.10}$$

where J is the coupling constant and $S\boldsymbol{n}_i$ ($|\boldsymbol{n}_i| = 1$) is the localized spin at site i. The localized spins interact each other through the coupling with itinerant electrons, and such interactions are called Ruderman-Kittel-Kasuya-Yosida interaction. The spin interaction to the lowest order in J/t, with t being the hopping amplitude, is given by the spin susceptibility of itinerant electrons. As a result, the spin interactions and resulting spin textures depend crucially on the nesting property of the Fermi surface. For example, when the magnitudes of the nesting vectors are large, a smaller skyrmion may be realized.

1.3.3 Multiple-Q order

A multiple-Q order is a magnetic order characterized by multiple wave numbers. For example, it may be described as $\boldsymbol{M}(\boldsymbol{r}) = \frac{1}{L^{d/2}} \sum_i \boldsymbol{M}_{\boldsymbol{Q}_i} e^{i\boldsymbol{Q}_i \cdot \boldsymbol{r}}$, where $\boldsymbol{M}(\boldsymbol{r})$ is the local magnetic moment at $\boldsymbol{r}$ and $\boldsymbol{M}_{\boldsymbol{Q}_i}$ is the Fourier component for $\boldsymbol{Q}_i$. A helical order is described by a single wave vector ($\boldsymbol{Q}_0$), while a triangular SkX is described by using three different wave vectors ($\boldsymbol{Q}_0, \boldsymbol{Q}_1, \boldsymbol{Q}_2$).

There are many types of multiple-Q states, other than a SkX. For instance, in the double exchange model [Eq. (1.3.10)], RKKY interactions stabilize a wide range of multiple-Q states depending on the lattice and Fermi surface structure. In a two-dimensional square lattice system, a noncollinear double-Q order is realized [76, 77]. Furthermore, a three-dimensional pyrochlore system at 1/4 filling realizes a noncoplanar triple-Q order [78].

Hubbard model is also known to realize multiple-Q states [79]. In Chap. 4, we study how the superconducting correlation and the supercurrent flow changes RKKY interaction in the Hubbard model.

1.3.4 Spin gauge field and topological superconductivity

Finally, before closing this section, we comment on the physical consequence of noncollinear and noncoplanar magnetic orders on the electron property. When electrons couples with noncollinear and noncoplanar magnetic orders, they show unusual transport properties, such as the unconventional Hall effect [17, 80]. In fact, coupling with magnetic textures plays similar roles as the anti-symmetric SO couplings. Let us consider the double exchange model [Eq. (1.3.10)] in the continuum limit for simplicity.

$$H = \int dr^d c^\dagger_\alpha(\boldsymbol{r}) \left(\left(\frac{\hat{p}^2}{2m} - \varepsilon_F \right) \delta_{\alpha,\beta} - J_{\mathrm{sd}} S \boldsymbol{n}(\boldsymbol{r}) \cdot \boldsymbol{\sigma}_{\alpha,\beta} \right) c_\beta(\boldsymbol{r}), \tag{1.3.11}$$

where $c_\sigma(\boldsymbol{r})$ is the electron operator at $\boldsymbol{r}$ with spin α and m is the electron mass. $\boldsymbol{n}(\boldsymbol{r})$ is a spin texture that slowly varies in space. To simplify the problem, we rewrite the Hamiltonian with the spin quantization axis in parallel to $\boldsymbol{n}(\boldsymbol{r})$. We introduce $a_\alpha(\boldsymbol{r})$, which is defined by

$$c_{i\alpha} = [U]_{\alpha\beta} a_\beta(\boldsymbol{r}), \tag{1.3.12}$$

where $U = \boldsymbol{m} \cdot \boldsymbol{\sigma}$ is a unitary matrix, and $\boldsymbol{m} = (\sin(\theta/2)\cos\phi, \sin(\theta/2)\sin\phi, \cos(\theta/2))$ with θ and ϕ being the polar and azimuthal angles of $\boldsymbol{n}(\boldsymbol{r})$. This unitary transformation diagonalizes the exchange coupling term as $U^\dagger(\boldsymbol{n} \cdot \boldsymbol{\sigma})U = \sigma^z$. As a result, the Hamiltonian is rewritten as

$$H = \int dr^d a^\dagger_\alpha(\boldsymbol{r}) \left[\left(\left(\frac{\hat{p}^2}{2m} - \varepsilon_F \right) - J_{\mathrm{sd}} S \sigma^z_{\alpha,\alpha} \right) \delta_{\alpha,\beta} + \frac{\hbar}{m} A^a_\mu \sigma^a_{\alpha,\beta} \hat{p}_\mu \right] a_\beta(\boldsymbol{r}), \tag{1.3.13}$$

to the linear order of the spatial derivative of $\boldsymbol{n}(\boldsymbol{r})$ [1], where we define the so-called spin gauge field as

$$A^a_\mu \sigma^a = -iU^\dagger \partial_\mu U, \tag{1.3.14}$$

$$= (\boldsymbol{m} \times \partial_\mu \boldsymbol{m}) \cdot \boldsymbol{\sigma}. \tag{1.3.15}$$

Now the Hamiltonian has terms equivalent to the Zeeman field ($-J_{\mathrm{sd}} S \sigma^z$) and the anti-symmetric SO coupling, which couples the spin and momentum as

$$\boldsymbol{g}_{\mathrm{eff}}(\boldsymbol{k}) \cdot \boldsymbol{\sigma} = \frac{\hbar^2}{m} A^a_\mu k_\mu \sigma^a \tag{1.3.16}$$

with $g^a_{\mathrm{eff}}(\boldsymbol{k}) = \frac{\hbar^2}{m} A^a_\mu k_\mu$ [$\boldsymbol{g}_{\mathrm{eff}}(\boldsymbol{k}) = -\boldsymbol{g}_{\mathrm{eff}}(-\boldsymbol{k})$].

Such an asymmetric coupling lifts the spin-degeneracy of the Fermi surface and realizes spinless p-wave or $p + ip$ -wave topological superconductivity with an s-wave pairing. To realize a 1D p-wave superconductor in this system, $A^x_x = (\boldsymbol{m} \times \partial_x \boldsymbol{m})_x \neq 0$ or $A^y_x = (\boldsymbol{m} \times \partial_x \boldsymbol{m})_y \neq 0$ is required. For example, a helical spin texture satisfies the condition [42, 43, 44, 45, 46], and it has been numerically confirmed [52].

To realize a 2D $p + ip$ superconductor, we need to have a noncollinear spin texture in the momentum space. For comparison, Rashba SO coupling exhibits a XY vortex-like texture in the momentum space. With a Zeeman field in the z direction and an s-wave superconductivity, we can realize spinless $p + ip$ superconductor. In the above case, in order to realize a Rashba-like SO coupling, i.e., spin is noncollinear in the k_x-k_y space (Fig, 1.4), the necessary condition is (A^x_x, A^y_x) and (A^x_y, A^y_y) are not in parallel, i.e.,

$$A^x_x A^y_y - A^y_x A^x_y = \frac{\hat{\boldsymbol{z}}}{4} \left(\boldsymbol{n} \cdot (\partial_x \boldsymbol{n} \times \partial_y \boldsymbol{n}) \right) \neq 0. \tag{1.3.17}$$

Importantly, it is proportional to the skyrmion "density", i.e., the integrand in the topological number that characterizes a skyrmion Eq. (1.3.5). Therefore, coupling to a skyrmion texture acts similarly to the Rashba SO coupling. It is numerically confirmed that a skyrmion crystal in proximity to an s-wave superconductor realizes $p+ip$ pairing, even without anti-symmetric SO couplings [52].

Furthermore, the noncoplanar texture gives rise to an effective magnetic field for a large $J_{\mathrm{sd}} S$. When $J_{\mathrm{sd}} S$ is large enough, we may neglect the off-diagonal terms in the spin space. Assuming $J_{\mathrm{sd}} S \gg \varepsilon_F$, we project the Hamiltonian to the lower spin band as

$$H \simeq \int dr^d a^\dagger_+(\boldsymbol{r}) \left[\frac{\hat{p}^2}{2m} - \varepsilon_F - J_{\mathrm{sd}} S + \frac{\hbar}{m} \boldsymbol{A}_{\mathrm{eff}} \cdot \hat{\boldsymbol{p}} \right] a_+(\boldsymbol{r}), \tag{1.3.18}$$

[1] We note that we drop the spatial dependence of A^a_μ at this point within this approximation.

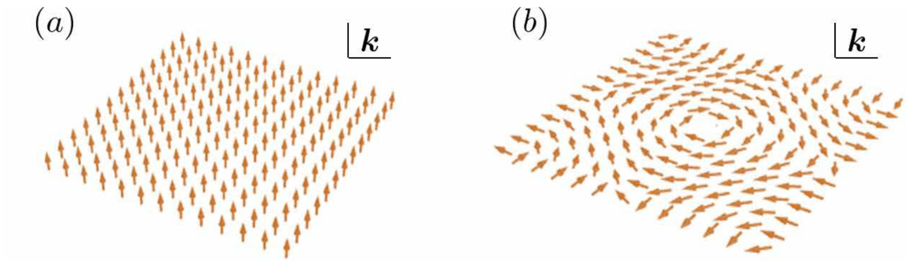

Figure 1.4: Spin state in momentum space. (a) A spin state that does not vary in momentum space. (b) A noncollinear spin state, which can be realized, e.g., with the Rashba SO coupling.

where we define $\boldsymbol{A}_{\text{eff}} = (A^z_x, A^z_y, A^z_z)$. We can see that $\boldsymbol{A}_{\text{eff}}$ acts like a vector potential, whose magnetic field is given by

$$\boldsymbol{\nabla} \times \boldsymbol{A}_{\text{eff}} = \frac{1}{2}\boldsymbol{n} \cdot (\partial_x \boldsymbol{n} \times \partial_y \boldsymbol{n}). \tag{1.3.19}$$

Again, it is proportional to the skyrmion density, and hence a skyrmion gives rise to an effective magnetic field, which manifests in the topological Hall effect [63, 64]. The similar discussions can be made in a lattice model, and the effective Peierls phase arises due to the noncoplanar spin configuration.

1.4 Spin manipulation

Efficient control of the spin orientation is crucial in spintronics. There are many proposals on spin manipulation. In this section, we first show how we can describe dynamics of spin textures in ferromagnets. Then we review different types of spin-torques in a normal system. Later, in Chap. 2 and 3, we show that a supercurrent exerts a spin torque on magnetic moments.

1.4.1 Landau-Lifshitz-Gilbert equation

Dynamics of classical spins are described by the Landau-Lifshitz-Gilbert (LLG) equation [2]. The LLG equation is given by

$$\frac{d\boldsymbol{S}}{dt} = \gamma \boldsymbol{H}_{\text{eff}} \times \boldsymbol{S} - \frac{\alpha}{S}\boldsymbol{S} \times \frac{d\boldsymbol{S}}{dt}, \tag{1.4.1}$$

where $\boldsymbol{H}_{\text{eff}}(\boldsymbol{r}) = \frac{1}{\hbar\gamma}\frac{\delta E}{\delta \boldsymbol{S}(\boldsymbol{r})}$is the effective magnetic field with E being the energy functional and α is the Gilbert damping coefficient.

[2]Here we note that the distinction between local spin moment $\boldsymbol{S}(\boldsymbol{r})$ and magnetization $\boldsymbol{M}(\boldsymbol{r}) = -\frac{\hbar\gamma}{a^d}\boldsymbol{S}(\boldsymbol{r})$,where $\gamma = \frac{g\mu_B}{\hbar} > 0$ is a gyromagnetic ratio.

The Gilbert damping term describes the energy dissipation of the spin as we can see as follows. By taking the outer product of $\boldsymbol{S}$ and Eq. (1.4.1) and multiplying $\frac{d\boldsymbol{S}}{dt}$, we obtain

$$\frac{dE}{dt} = \frac{1}{\hbar}\frac{d\boldsymbol{S}}{dt} \cdot \frac{\partial E}{\partial \boldsymbol{S}} = -\frac{\alpha}{S}\left(\frac{d\boldsymbol{S}}{dt}\right)^2. \tag{1.4.2}$$

The energy dissipation of the spin is proportional to $\left(\frac{d\boldsymbol{S}}{dt}\right)^2$, and it can occur by the coupling with the lattice and the conduction electrons.

1.4.2 Thiele's approach

In most cases, LLG equation cannot be solved exactly. Instead, one can formulate the dynamics of a magnetic texture in terms of collective coordinates. This method is called (generalized) Thiele's approach [81, 82]. In this approach, we choose collective coordinates $\boldsymbol{R}(t) = \{R_0, R_1, R_2, ...\}$, and focus on their time dependence as $\boldsymbol{S}(\boldsymbol{r}, t) = \boldsymbol{S}(\boldsymbol{r}, \{\boldsymbol{R}(t)\})$ assuming that other degrees of freedom are not important for low energy dynamics. Then the LLG equation leads to

$$(\Gamma_{ij} - G_{ij})\,\dot{R}_j = F_i, \tag{1.4.3}$$

where

$$F_i = \int dr^d \frac{\delta \boldsymbol{n}}{\partial R_i} \cdot \frac{\delta E}{\delta \boldsymbol{n}} = \frac{\delta E}{\delta R_i}, \tag{1.4.4}$$

$$\Gamma_{ij} = \hbar S \alpha \int dr^d \frac{\partial \boldsymbol{n}}{\partial R_i} \cdot \frac{\partial \boldsymbol{n}}{\partial R_j}, \tag{1.4.5}$$

$$G_{ij} = \hbar S \int dr^d \boldsymbol{n} \cdot \left(\frac{\partial \boldsymbol{n}}{\partial R_i} \times \frac{\partial \boldsymbol{n}}{\partial R_j}\right), \tag{1.4.6}$$

Here we note the relation: $\Gamma_{ij} = \Gamma_{ji}$ and $G_{ij} = -G_{ji}$. When the collective coordinates only denote the center of mass positions, the magnetic texture behaves like a point particle but without an inertial mass. When some other degrees of freedom, such as internal structures, are considered, inertial masses may arise, or the dynamics cannot even be described by that of a point particle.

A domain wall in Eq. (1.3.4) has the collective coordinates X and ϕ_0, i.e., the center of mass position and the magnetic angle at the center. Because of ϕ_0, a domain wall does not behave like a particle but shows a complex dynamics depending on parameters. As for a skyrmion, the internal excitations have the energy gap, and hence a skyrmion behaves like a particle without inertial mass to the lowest order approximation [3]. As an important feature, a "Magnus force" in the Hall direction acts on a skyrmion because its topological structure renders $G_{xy} \neq 0$.

[3] It has been shown that the low energy internal excitations of the skyrmions do cause the inertial mass[83].

1.4.3 Spin torque

In the LLG equation, $\boldsymbol{T} = \gamma \boldsymbol{H}_{\text{eff}} \times \boldsymbol{S}$ acts as a spin torque, and hence any fields or currents that couple to spins can be a source of a torque. Here we show some examples of spin torques.

Magnetic field

A magnetic field gives rise to a spin precession. With the Gilbert damping, spins gradually align with the magnetic field and the energy decreases. This relaxation process can be used for a domain wall manipulation. Since a magnetic field gives the potential energy for the position of the domain wall. a domain wall motion can be driven by a static magnetic field when there is the Gilbert damping. In the simplest case without pinning potentials, a uniform linear motion of a domain wall is realized. Domain wall motions driven by magnetic field are observed in experiments [84].

Spin transfer torque

Spin-transfer torques (STT), which can control magnetization with an electric current, have attracted attention[85, 86, 87, 88, 89, 90, 91]. It is useful in nanoscale control and often energetically efficient compared to the ampere field (magnetic field induced torque). STT can be applied to magnetic random access memory and the racetrack memory using magnetic domain walls or skyrmions[59]. The origin of STT is the transfer of spin angular momentum via spin-polarized currents.

STT is studied in two situations: magnetic multilayers and a smooth magnetic texture. The former approximates that each layer is characterized by a single magnetic moment, and an applied current transfers spin angular momentum from layer to layer. This has been observed in magnetic tunnel junctions.

Here let us focus on the latter case, STT on a smooth magnetic texture. In a smooth magnetic texture $\boldsymbol{n} = \boldsymbol{S}/S$, spin-polarized currents exert STT on $\boldsymbol{n}$, which is given by [92, 93, 94]

$$\boldsymbol{\tau}_{\text{STT}} = -(\boldsymbol{j}_s \cdot \boldsymbol{\nabla})\boldsymbol{n} + \beta \boldsymbol{n} \times (\boldsymbol{j}_s \cdot \boldsymbol{\nabla})\boldsymbol{n}. \tag{1.4.7}$$

Here $\boldsymbol{j}_s = -(Pa^d/2eS)\boldsymbol{j}$, and β is a dimensionless parameter, where $\boldsymbol{j}[\text{A/m}^{d-1}]$ is a charge current density, P is the spin polarization of current, a is the lattice constant, S is the spin size, and $-e$ is the electron charge. The first term in Eq. (1.4.7) arises when the electron spins follow the texture adiabatically. The second term, often referred to as the non-adiabatic torque, is known to have two origins [95, 96, 93]. It appears from spin-flip impurity scatterings or the spin-orbit coupling. It also occurs when electrons fail to follow magnetic textures because the texture is not smooth enough. As demonstrated in several works [97, 93], the non-adiabatic torque plays a crucial role in magnetization dynamics. For

$\beta \neq 0$, the threshold current density for a steady motion of a domain wall becomes zero in the absence of pinning potentials.

Spin-orbit torque

In noncentrosymmetric systems, SO coupling gives rise to an additional current-induced torque called SO torque [98, 99, 100, 101, 102]. In noncentrosymmetric materials, charge currents induce a spin polarization via the anti-symmetric SO coupling[103, 16, 104, 105], which is known as the Edelstein effect or the inverse spin-galvanic effect. This can be understood from the coupling between the spin and the momentum on the Fermi surface. An electric field displaces the Fermi surface and creates an imbalanced population of electrons between $\boldsymbol{k}$ and $-\boldsymbol{k}$. This imbalance is accompanied by a net spin polarization. For example, with the Rashba SO coupling, the spin polarization induced by a current is proportional to $\hat{\boldsymbol{z}} \times \boldsymbol{j}$ with a current density $\boldsymbol{j}$.

This induced spin polarization acts as a spin-torque. Importantly, while STT requires noncollinear magnetic moments or textures, this SO torque does not. The direction of this effective field depends on the current direction so that a local control of "magnetic" field can be possible with the use of the Edelstein effect. Experimentally, a spin-orbit torque is observed in a ferromagnetic metal [101] and the ferromagnetic semiconductor (Ga, Mn)As [106].

Chapter 2

Spin-transfer torque induced by triplet supercurrent

In this chapter, we study spin transfer torques induced by a spin-triplet supercurrent in a magnet in proximity to a superconductor. By a perturbative approach, we show that spin-triplet correlations realize new types of torque, which are analogous to the adiabatic and non-adiabatic torques. Remarkable advantages compared to conventional spin-transfer torques are highlighted in domain wall manipulation. Oscillatory motions of a domain wall, which could decrease efficiency, can be avoided. Furthermore, the threshold current density can be zero depending on the triplet-correlations. Our results show that a triplet correlation qualitatively changes the spin-transfer process, and efficient manipulation of a magnetic domain wall can be realized.

The organization of this chapter is as follows. In Sec. 2.1, we give the background and the aim of this work. In Sec. 2.2, we present the model we used in our calculation. In Sec. 2.3, we show the derivation and result on the spin transfer torque induced by a triplet supercurrent. In Sec. 2.4, we discuss domain wall dynamics driven by the obtained torque. In Sec. 2.5, we present the summary and discussion of this work. Section 2.6 provides the details of the calculation.

2.1 Introduction to this chapter

Recently more and more people are interested in applying superconductivity for spintronics [107, 108]. Here are important topics in spintronics: (1) the lifetime of spin, (2) spin valves, and (3) spin torques. Their interplay with superconductivity has been studied so far as follows.

(1) The time scale over which the spin density relaxes is a basic and important quantity in spintronics. It reflects the character of excitation particles such as electrons and phonons. The lifetime of spin density is enhanced in a superconducting state relative to a normal (metallic) state [109, 110, 111]. Injecting spin polarized electrons into a superconductor causes both spin and charge imbalances. Interestingly, the imbalances do not relax over the same time scale, but the spin imbalance survives much longer ($\sim$ 10ns) than the charge imbalance, which lives for $\sim$ 1ps [110]. Importantly, the spin lifetime is much longer than one in normal states.

(2) A spin valve is a device which consists of metallic magnetic layers. The electrical resistance in the direction normal to the layers depend on the alignment of the magnetization, and hence we can "write" by changing magnetic alignment and "read" the written information by the electrical resistance. With spin valves using superconductors[112, 113, 114, 115], one can change the resistance drastically. Li *et al.* [115] used a EuS (1.5 nm)/Al (3.5 nm)/EuS (4 nm) structure, where EuS is a ferromagnetic insulator and Al becomes a superconductor at $T_c \sim 1.2$K. Two magnetic layers with different thicknesses have different coercivities, and they can have an (anti)parallel alignment depending on the magnitude of magnetic fields. For the antiparallel alignment, the resistivity drops to zero, while it is finite for the parallel alignment.

(3) As we have introduced in Sec. 1.4, spin torques have been intensively studied in the field of spintronics. They can be useful in magnetic memories. It has been shown that the Josephson current exerts a spin torque on magnetization in ferromagnetic Josephson junctions [116, 117, 118, 119, 120, 121, 122]. For example, Waintal *et al.* [116] studied an F/N/F junction with two s-wave superconducting contacts, where F is a ferromagnetic layer and N is a normal metallic layer. The exchange interaction of spins is affected by the phase difference between the two superconductors.

The interplay of superconductivity and magnetic moments is important especially with spin-triplet Cooper pairs due to the coupling between triplet order parameters and localized moments [1, 2, 3, 4, 5, 6]. Triplet pairs can arise in the interface between a ferromagnet and singlet superconductor when there is noncollinear magnetism [18] or spin-orbit couplings [19, 20]. Experimentally, the proximity effect of triplet pairs has been observed in fully-spin polarized metals[21, 22] and multilayers with noncollinear magnets[23, 24]. The spin-triplet proximity effect to a ferromagnet from Sr_2RuO_4, a candidate of a triplet superconductor, has been also observed[11].

Given the recent experimental advances in the proximity-induced triplet Cooper pairs in magnets, triplet supercurrent-induced STT is a promising way to realize an efficient control of magnetization. Utilization of a supercurrent suppresses Joule heating and the tunablity of STT may be enhanced by pairing degrees of freedom. However, while several works showed that a supercurrent exerts a spin-torque in ferromagnetic Josepshon junctions[116, 117, 118, 119, 120, 121, 122], it still remains unclear how a triplet supercurrent acts on a localized moment, and how STT is changed by triplet-paring correlation. In order to reveal a role of spin-triplet pairings in STT and propose a torque with desired properties, microscopic calculations are required. The aim of this work to microscopically study STT induced by triplet supercurrents, and to reveal the properties of the STT in domain wall manipulation.

2.2 Model

In our work, we consider a thin-film magnet with the proximity effect of p-wave triplet superconductivity modeled by the Hamiltonian :

$$\begin{aligned} H_{\mathrm{el}} =& -t\sum_{\langle i,j\rangle} c^\dagger_{i\alpha}c_{j\alpha} - \mu\sum_i c^\dagger_{i\alpha}c_{i\alpha} - J_{\mathrm{sd}}S\sum_i \boldsymbol{n}(\boldsymbol{r}_i)\cdot\boldsymbol{\sigma}_{\alpha\beta}c^\dagger_{i\alpha}c_{i\beta} \\ &+ \frac{\Delta_0}{2}\sum_{i,j} e^{i\boldsymbol{\kappa}\cdot(\boldsymbol{r}_i+\boldsymbol{r}_j)}\left[(\boldsymbol{d}_{ij}\cdot\boldsymbol{\sigma})i\sigma^y\right]_{\alpha\beta} c^\dagger_{i\alpha}c^\dagger_{j\beta} + \mathrm{H.c.} \end{aligned} \tag{2.2.1}$$

Here $c^\dagger_{i\alpha}(c_{i\alpha})$ is the electron creation (annihilation) operator at site i with spin α on a square lattice, $\langle i,j\rangle$ is taken over the nearest neighbor pairs, t is the hopping amplitude, and μ is the chemical potential. Electrons couple to localized spins given by $S\boldsymbol{n}(\boldsymbol{r}_i) = S(\sin\theta\cos\phi, \sin\theta\cos\phi, \cos\theta)$ with the coupling constant J_{sd}. The spin texture $\boldsymbol{n}(\boldsymbol{r})$ varies smoothly with the length scale ℓ ($\gg \xi_{\mathrm{SC}}$) where ξ_{SC} denotes the superconducting coherence length. The last term in Eq. (2.2.1) is the proximity-induced triplet p-wave pairing, given by $\boldsymbol{d}_{ij} = (d^x_{ij}, d^y_{ij}, d^z_{ij})$, where $\boldsymbol{d}_{ij} = -\boldsymbol{d}_{ji}$, and Δ_0 is the pairing amplitude.

The phase gradient of the paring function describes a supercurrent. We consider a phase given by $\boldsymbol{\kappa}\cdot(\boldsymbol{r}_i+\boldsymbol{r}_j)$, which results in the supercurrent density $\boldsymbol{j} \simeq -2ten_e a^2\boldsymbol{\kappa}$ (for $|\boldsymbol{\kappa}|a \ll 1$ and at low temperature), where n_e is an electron density[1] that participates in the supercurrent. Here, the supercurrent can be supplied from an external dc current source. We also note that we can restore the gauge invariance by redefining $\boldsymbol{\kappa}$ in the current so as to include the vector potential.

As shown in Fig. 2.1, a relevant experimental setup of the above model is a heterostructure composed of a metallic magnet and a triplet superconductor (e.g., Sr_2RuO_4). A triplet

[1] For a high density, n_e should be replaced with an effective electron density modified by lattice effects.

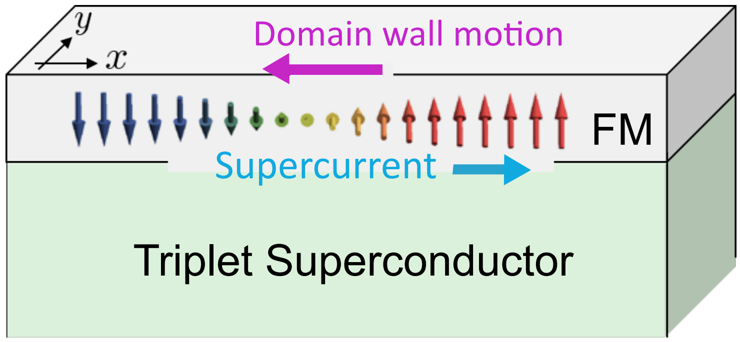

Figure 2.1: Schematic picture of the proposed setup. A ferromagnet (FM) with a domain wall is attached on a superconductor, which produces a spin-triplet proximity effect. We apply a supercurrent in the xy plane and drive the domain wall motion. We note that it is necessary to prepare a situation, in which a supercurrent does not escape from a magnetic texture. Experimentally, S/F/S trilayers might also be a good setup.

superconductor can be replaced by a singlet superconductor (e.g., Nb) with a conical magnetic layer such as Ho [24] or the spin-orbit coupling[19, 20], which produces the triplet proximity effect.

2.3 Spin-transfer torque induced by triplet supercurrent

To derive STT, we calculate the spin density induced by a supercurrent to the linear order of $\boldsymbol{j} \propto \boldsymbol{\kappa}$. In the following calculation, we perturbatively treat the spatial derivative of $\boldsymbol{n}(\boldsymbol{r}_i)$. As we have shown in Sec. 1.3.4, this perturbation can be simplified by rewriting the Hamiltonian with electron operators $a_{i\alpha}$, the spin quantization axis of which is parallel to $\boldsymbol{n}(\boldsymbol{r}_i)$[93]. It is defined by $c_{i\alpha} = (U(\boldsymbol{r}_i))_{\alpha\beta} a_{i\beta}$, where $U(\boldsymbol{r}_i) = \boldsymbol{m}(\boldsymbol{r}_i) \cdot \boldsymbol{\sigma}$ is a unitary matrix, and $\boldsymbol{m}(\boldsymbol{r}_i) = (\sin(\theta/2)\cos\phi, \sin(\theta/2)\sin\phi, \cos(\theta/2))$ with θ and ϕ being the angles of $\boldsymbol{n}(\boldsymbol{r}_i)$. This satisfies $U^\dagger(\boldsymbol{n}\cdot\boldsymbol{\sigma})U = \sigma^z$. The Hamiltonian Eq. (2.2.1) is rewritten as

$$
\begin{aligned}
H_{\mathrm{el}} \simeq & \sum_{\boldsymbol{k}} (\xi_{\boldsymbol{k}} \mathbb{I}_2 - J_{\mathrm{sd}} S \sigma^z)_{\alpha\alpha} a^\dagger_{\boldsymbol{k}\alpha} a_{\boldsymbol{k}\alpha} + \sum_{\boldsymbol{k},\boldsymbol{q}} v^\nu_{\boldsymbol{k}+\boldsymbol{q}/2} A^a_\nu(\boldsymbol{q}) \sigma^a_{\alpha\beta} a^\dagger_{\boldsymbol{k}+\boldsymbol{q}\alpha} a_{\boldsymbol{k}\beta} \\
& + \frac{1}{2} \sum_{\boldsymbol{k}} \Delta^\alpha_{\boldsymbol{k}} a^\dagger_{\boldsymbol{k}+\boldsymbol{\kappa}\alpha} a^\dagger_{-\boldsymbol{k}+\boldsymbol{\kappa}\alpha} + \mathrm{H.c.} \ , \qquad (2.3.1)
\end{aligned}
$$

where $\xi_{\boldsymbol{k}} = -2t(\cos(k_x a) + \cos(k_y a)) - \mu$ is the kinetic energy, $v^\nu_{\boldsymbol{k}} = \partial\xi_{\boldsymbol{k}}/\partial k_\nu$ is the velocity, $\mathbb{I}_2 = \mathrm{diag}(1,1)$, and $a_{\boldsymbol{k}\alpha}$ is the Fourier transform of $a_{i\alpha}$. The second term arises from the hopping in the presence of a noncollinear texture. Here we define the spin gauge field $A^a_{\nu i}\sigma^a = -iU(\boldsymbol{r}_i)\partial_\nu U(\boldsymbol{r}_i)$, where we denote $A^b_\nu(\boldsymbol{q}) = N^{-1}\sum_i A^b_{\nu i} e^{-i\boldsymbol{q}\cdot\boldsymbol{r}_i}$ with $\nu = \{x, y, z\}$

and $b = \{x, y, z\}$. N is the total number of sites. Assuming a large exchange splitting $\sim 2J_{\mathrm{sd}}S \gg |\Delta_0|$, we focus on the equal spin pairing given by

$$\Delta_{\boldsymbol{k}}^{\alpha} = \Delta_0 (U^{\dagger}(\boldsymbol{d}(\boldsymbol{k}) \cdot \boldsymbol{\sigma}) i\sigma^y U^*)_{\alpha\alpha}, \tag{2.3.2}$$

$$= -\Delta_0 \left((\mathcal{R}^{ab} d^b(\boldsymbol{k}) \sigma^a) i\sigma^y \right)_{\alpha\alpha}, \tag{2.3.3}$$

where $\boldsymbol{d}(\boldsymbol{k}) = N^{-1} \sum_{\langle ij \rangle} \boldsymbol{d}_{ij} e^{-i\boldsymbol{k}\cdot(\boldsymbol{r}_i - \boldsymbol{r}_j)}$. We neglect pairings between spin-split bands, which correspond to the components of $\boldsymbol{d}(\boldsymbol{k})$ parallel to $\boldsymbol{n}$. $\mathcal{R}^{ab} = 2m^a m^b - \delta^{ab}$ $(a, b = \{x, y, z\})$ is a SO(3) rotation matrix corresponding to the unitary matrix U. In the last term in Eq. (2.3.1), we neglect the spatial dependence of θ, ϕ, terms of the order of ξ_{SC}/ℓ, assuming that $|\Delta_0(\boldsymbol{k})|/t$ is also a small parameter.

The spin expectation value of electrons $s_i^a = \frac{1}{2}(\sigma^a)_{\alpha\beta} \langle c_{i\alpha}^{\dagger} c_{i\beta} \rangle$ can be described by the operator $a_{i\alpha}$ as

$$s_i^a = \mathcal{R}^{ab}(\boldsymbol{r}_i) \tilde{s}_i^b, \tag{2.3.4}$$

where $\tilde{s}_i^a = \frac{1}{2}(\sigma^a)_{\alpha\beta} \langle a_{i\alpha}^{\dagger} a_{i\beta} \rangle$. Noting this relation, we obtain the spin density induced by a supercurrent as

$$\delta \tilde{s}_{\boldsymbol{q}}^a := \left(\lim_{\boldsymbol{\kappa} \to \boldsymbol{0}} \frac{\tilde{s}_{\boldsymbol{q}}^a - \tilde{s}_{\boldsymbol{q}}^a|_{\boldsymbol{\kappa}=\boldsymbol{0}}}{\kappa_\eta} \right) \frac{j_\eta}{(-2ten_e a^2)}, \tag{2.3.5}$$

$$= \pi_{\nu\eta}^{ab} A_\nu^b(\boldsymbol{q}) \frac{j_\eta}{2en_e}, \tag{2.3.6}$$

where $\delta \tilde{\boldsymbol{s}}_{\boldsymbol{q}} = N^{-1} \sum_i \delta \tilde{\boldsymbol{s}}_i e^{-i\boldsymbol{q}\cdot\boldsymbol{r}_i}$ and

$$\pi_{\nu\eta}^{ab} = \lim_{\boldsymbol{q} \to \boldsymbol{0}} \frac{-T}{4Nta^2} \sum_{n,\boldsymbol{k}} \frac{\partial^2 \xi_{\boldsymbol{k}}}{\partial k_\nu \partial k_\eta} \mathrm{Tr}[S^a \mathcal{G}_{\boldsymbol{k}+\boldsymbol{q}}(i\epsilon_n) S^b \mathcal{G}_{\boldsymbol{k}}(i\epsilon_n)]. \tag{2.3.7}$$

The details are presented in Sec. 2.6.1. Here, $\mathcal{G}_{\boldsymbol{k}}(i\epsilon_n)$ is the Green function in Nambu representation, the basis of which is $(a_{\boldsymbol{k}\uparrow}, a_{\boldsymbol{k}\downarrow}, a_{-\boldsymbol{k}\uparrow}^{\dagger}, a_{-\boldsymbol{k}\downarrow}^{\dagger})^T$, and S^a is a spin matrix in the Nambu representation, which is given by

$$S^a = \begin{pmatrix} \sigma^a & \\ & -(\sigma^a)^T \end{pmatrix}. \tag{2.3.8}$$

Its inverse is defined by $(\mathcal{G}_{\boldsymbol{k}}(i\varepsilon_n))^{-1} = i\epsilon_n \mathbb{I}_4 - H_{\mathrm{BdG}}(\boldsymbol{k})$, where

$$H_{\mathrm{BdG}}(\boldsymbol{k}) = \begin{pmatrix} \xi_{\boldsymbol{k}} \mathbb{I}_2 - M\sigma^z & \Delta(\boldsymbol{k}) \\ \Delta^*(\boldsymbol{k}) & -\xi_{\boldsymbol{k}} \mathbb{I}_2 + M\sigma^z \end{pmatrix}, \tag{2.3.9}$$

$\mathbb{I}_4 = \mathrm{diag}(1, 1, 1, 1)$, $\epsilon_n = \pi T(2n + 1)$ is Matsubara frequency with temperature T, and $\Delta(\boldsymbol{k}) = \mathrm{diag}(\Delta_{\mathrm{k}}^{\uparrow}, \Delta_{\mathrm{k}}^{\downarrow})$.

In Eq. (2.3.7), we have neglected terms which are vanishingly small at low temperatures compared to the critical temperature, in a system with a full gap or point nodes. Also, we have taken the limit $\boldsymbol{q} \to \boldsymbol{0}$ assuming that the momentum transfer from a smooth magnetic texture is small compared to the Fermi momentum [93]. We note that $\boldsymbol{s}_i$ is invariant by a unitary transformation $U \to Ue^{i\varphi\sigma^z}$ with an arbitrary spin rotational angle $\varphi(\boldsymbol{r})$ around $\boldsymbol{n}$, while $\tilde{\boldsymbol{s}}_i$ and $\mathcal{R}^{ab}$ change their forms. In the following, we explicitly use $\frac{\partial^2 \xi_{\boldsymbol{k}}}{\partial k_\nu \partial k_\eta} \propto \delta_{\nu\eta}$ and define $\pi^{ab}_{\nu\eta} = \pi^{ab}_\nu \delta_{\nu\eta}$.

From Eqs. (2.3.4) and (2.3.6), we obtain the local STT, $\boldsymbol{\tau}_{\mathrm{STT}} = 2J_{\mathrm{sd}}\boldsymbol{n} \times \delta\boldsymbol{s}_i$, as

$$\boldsymbol{\tau}_{\mathrm{STT}} = \sum_{\nu=x,y} \frac{-\tilde{P}_\nu a^3}{2eS} j_\nu \left(-\partial_\nu \boldsymbol{n} + \tilde{\beta}_\nu \boldsymbol{n} \times \partial_\nu \boldsymbol{n}\right). \tag{2.3.10}$$

Here $\tilde{P}_\nu$ and $\tilde{\beta}_\nu$ are the analogs of the spin polarization of a current P and β in Eq. (1.4.7), and they are given by

$$\tilde{P}_\nu = \frac{J_{\mathrm{sd}}S}{n_e a^3}\left[\frac{1}{2}\left(\pi^{xx}_\nu + \pi^{yy}_\nu\right) + \frac{1}{|\partial_\nu \boldsymbol{n}|^2}\left(-\pi^{(1)}_\nu \left((\partial_\nu\theta)^2 - \sin^2\theta(\partial_\nu\phi)^2\right) + 2\pi^{(2)}_\nu \sin\theta\partial_\nu\theta\partial_\nu\phi\right)\right], \tag{2.3.11}$$

$$\tilde{\beta}_\nu = -\frac{J_{\mathrm{sd}}S}{n_e a^3}\frac{1}{\tilde{P}_\nu}\frac{1}{|\partial_\nu \boldsymbol{n}|^2}\left(\pi^{(2)}_\nu \left((\partial_\nu\theta)^2 + \sin^2\theta(\partial_\nu\phi)^2\right) + 2\pi^{(1)}_\nu \sin\theta\partial_\nu\theta\partial_\nu\phi\right), \tag{2.3.12}$$

where

$$\pi^{(1)}_\nu = \cos(2\phi)\frac{1}{2}\left(\pi^{xx}_\nu - \pi^{yy}_\nu\right) + \sin(2\phi)\pi^{xy}_\nu, \tag{2.3.13}$$

$$\pi^{(2)}_\nu = \sin(2\phi)\frac{1}{2}\left(\pi^{xx}_\nu - \pi^{yy}_\nu\right) - \cos(2\phi)\pi^{xy}_\nu. \tag{2.3.14}$$

These are the central results of this chapter, which are applicable to any smooth magnetic textures. Notably, in the low density limit and at low temperature, $\tilde{P}_\nu$ and $\tilde{\beta}_\nu$ are given by the spin susceptibility perpendicular to $\boldsymbol{n}$ since π^{ab}_ν is equivalent to the bare spin susceptibility of the $a_{\boldsymbol{k}\alpha}$ field. To make $\tilde{\beta}_\nu$ finite, anisotropy such as $\pi^{xx}_\nu \neq \pi^{yy}_\nu$ or $\pi^{xy}_\nu \neq 0$ is necessary. As is known in the spin susceptibility [7], such anisotropy naturally arises with a triplet pairing. They depend on the relative phase between $\Delta^{\uparrow}_{\boldsymbol{k}}$ and $\Delta^{\downarrow}_{\boldsymbol{k}}$ as $\frac{1}{2}\left(\pi^{xx}_\nu - \pi^{yy}_\nu\right) = \lim_{\boldsymbol{q}\to\boldsymbol{0}} N^{-1}\sum_{\boldsymbol{k}} \mathrm{Re}(\Delta^{*\uparrow}_{\boldsymbol{k}}\Delta^{\downarrow}_{\boldsymbol{k}}) f_\nu(\boldsymbol{k},\boldsymbol{q})$ and $\pi^{xy}_\nu = \lim_{\boldsymbol{q}\to\boldsymbol{0}} N^{-1}\sum_{\boldsymbol{k}} \mathrm{Im}(\Delta^{*\uparrow}_{\boldsymbol{k}}\Delta^{\downarrow}_{\boldsymbol{k}}) f_\nu(\boldsymbol{k},\boldsymbol{q})$, where $f_\nu(\boldsymbol{k},\boldsymbol{q})$ is presented in Sec. 2.6.1. Therefore, a triplet pairing can make $\tilde{\beta}_\nu$ finite and cause the non-adiabatic torque without extrinsic scattering processes. Furthermore, $\tilde{P}_\nu$ and $\tilde{\beta}_\nu$ depend on the spatial position through the coupling between the d vector and $\boldsymbol{n}$. This is important for a domain wall dynamics as we see in the next section.

2.4 Domain wall dynamics

Now, we demonstrate domain wall dynamics induced by the obtained STT. We consider the Hamiltonian $H_{\rm tot} = H_{\rm el} + H_{\rm spin}$, where $H_{\rm el}$ is given in Eq. (2.3.1) and

$$H_{\rm spin} = \frac{S^2}{2}\sum_i \left(-J(\partial_\nu \boldsymbol{n}(\boldsymbol{r}_i,t))^2 - Kn_z(\boldsymbol{r}_i,t)^2 + K_\perp n_y(\boldsymbol{r}_i,t)^2\right). \tag{2.4.1}$$

Here, J is the ferromagnetic exchange coupling, and $K, K_\perp$ are the onsite anisotropies that satisfy $K_\perp \ll K \ll Ja^{-2}$. We consider a domain wall configuration given by $\boldsymbol{n}(\boldsymbol{r},t) = (\cos\phi_0(t)\sin\theta(x,t), \sin\phi_0(t)\sin\theta(x,t), \cos\theta(x,t))$, where $\cos\theta(x,t) = \tanh\left(\frac{x-X(t)}{\lambda}\right)$, $\lambda = \sqrt{J/K}$, and $X(t)$ is the domain wall center. A schematic figure of a domain wall for $\phi_0 = \pi$ is shown in Fig. 2.1. With this configuration, the STT in Eq. (2.3.10) is characterized by $\tilde{P}_x = \frac{J_{\rm sd}S}{n_e a^3}\left[\frac{1}{2}\left(\pi_x^{xx} + \pi_x^{yy}\right) - \pi_x^{(1)}\right]$ and $\tilde{\beta}_x = -\frac{J_{\rm sd}S}{n_e a^3}\frac{\pi_x^{(2)}}{\tilde{P}_x}$. Including the effects of damping, we obtain the equations of motion of $\phi(t)$ and $X(t)$ as

$$\partial_t X = \frac{v_c}{(1+\alpha^2)}\left(\tau(\phi_0)j_x + \alpha F(\phi_0)j_x + \sin 2\phi_0\right), \tag{2.4.2}$$

$$\partial_t \phi_0 = \frac{-1}{(1+\alpha^2)t_0}\left(\alpha\tau(\phi_0)j_x - F(\phi_0)j_x + \alpha\sin 2\phi_0\right), \tag{2.4.3}$$

where α is the Gilbert damping constant, $v_c = K_\perp \lambda S/2$, and $t_0 = \lambda/v_c$. $\tau(\phi_0)$ and $F(\phi_0)$ denote the coupling to the current via STT. They read

$$\tau(\phi_0) = -\frac{a}{2v_c}\sum_i \frac{\tilde{P}_x a^3}{2eS}\partial_x n^z, \tag{2.4.4}$$

$$F(\phi_0) = \frac{a}{2v_c}\sum_i \frac{\tilde{P}_x a^3}{2eS}\tilde{\beta}_x \partial_x n^z. \tag{2.4.5}$$

In the above equations of motions, we have assumed that the electron spin density induced by $\dot{\boldsymbol{n}}$ does not change the dynamics qualitatively when the spin size S is large. Also, we did not consider pinning potentials for simplicity. The explicit form of $F(\phi_0)$ as the function of $\boldsymbol{d}(\boldsymbol{k})$ is presented in Sec. 2.6.2 .

In the following, we consider triplet pairing given by $\boldsymbol{d}(\boldsymbol{k}) = (-\sin k_y a, \sin k_x a, \delta \sin k_x a)$. Such a pairing can be stabilized by the spin-orbit coupling $\boldsymbol{g}(\boldsymbol{k})\cdot\boldsymbol{\sigma}$ ($\boldsymbol{g}(\boldsymbol{k}) = -\boldsymbol{g}(-\boldsymbol{k})$) in a system without inversion symmetry; $\boldsymbol{d}(\boldsymbol{k}) \parallel \boldsymbol{g}(\boldsymbol{k})$ is energetically favored[14]. The Rashba type spin-orbit coupling can stabilize $\boldsymbol{d}(\boldsymbol{k}) = (-\sin(k_y a), \sin(k_x a), 0)$, and in our case, it can originate from the boundary between the superconductor and ferromagnet. Furthermore, we add $d^z(\boldsymbol{k}) = \delta\sin(k_x a)$, which can be attributed to the additional spin-orbit coupling due to the broken mirror symmetry about the xz plane.

In numerical calculations, we set $\mu/t = -1.8, \Delta_0/t = 5\times10^{-2}, J_{\rm sd}S/t = 1$, and $T/t = 5\times10^{-3}$. Using the above $\boldsymbol{d}(\boldsymbol{k})$, we first show $\tilde{P}_x$ and $\tilde{\beta}_x$ in the domain wall configuration for

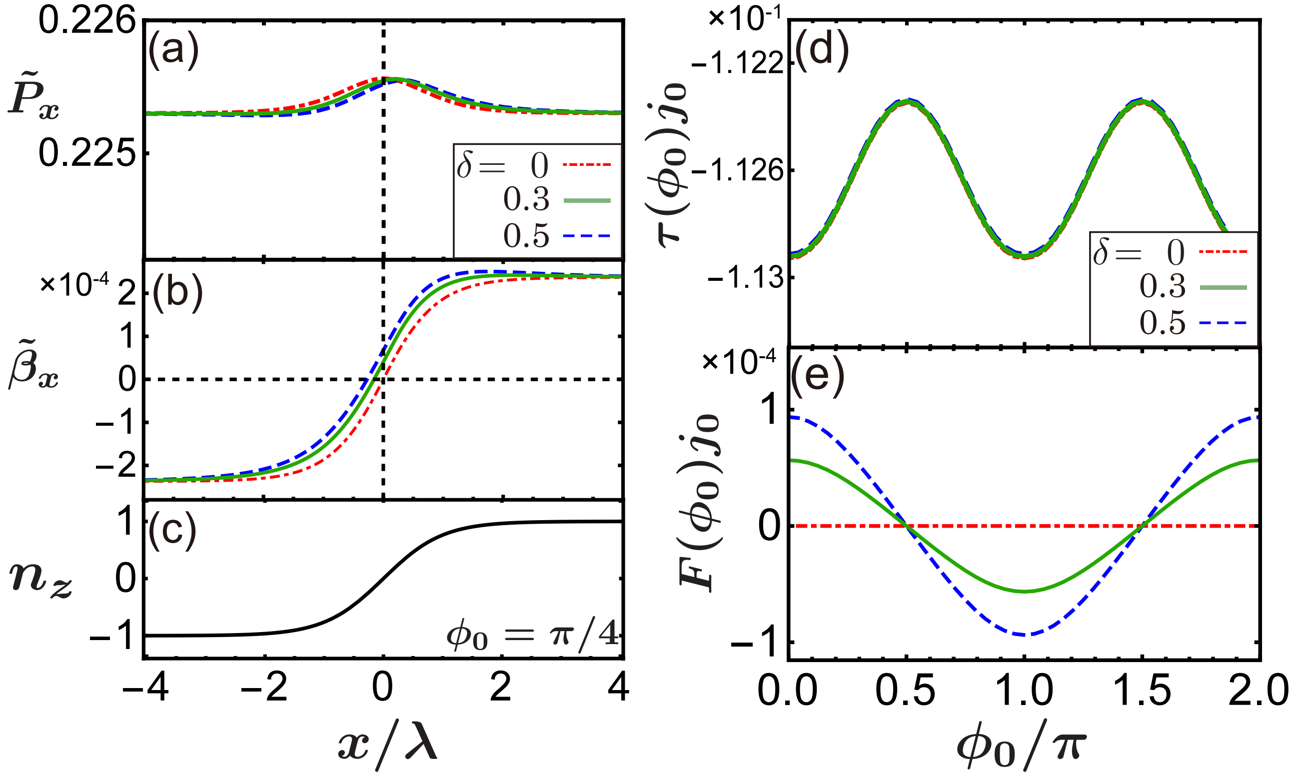

Figure 2.2: (a) $\tilde{P}_x$ and (b) $\tilde{\beta}_x$ in a domain wall configuration with $\phi_0 = \pi/4$ as functions of the position x for different δ, where d vector is $\boldsymbol{d}(\boldsymbol{k}) = (-\sin k_y a, \sin k_x a, \delta \sin k_x a)$. (c) The profile of the domain wall. (d) $\tau(\phi_0)$ and (e) $F(\phi_0)$ as functions of ϕ_0 for different δ, where we define $j_0 = Sev_c a^{-3}$.

$\phi_0 = \pi/4$ (Fig. 2.2 (a)-(c)). Effective spin polarization $\tilde{P}_x$ is almost constant in space. On the other hand, $\tilde{\beta}_x$ highly depends on the spatial position. Importantly, $\tilde{P}_x$ ($\tilde{\beta}_x$) is symmetric (antisymmetric) under $x \to -x$ for $\delta = 0$, while $\tilde{P}_x$ and $\tilde{\beta}_x$ are slightly shifted for $\delta \neq 0$. Because of such symmetries, $F(\phi_0)$ (Eq. (2.4.5)) vanishes for $\delta = 0$, where we note $\partial_x n^z$ is an even function of x. On the other hand, for $\delta \neq 0$ such symmetries of $\tilde{P}_x$ and $\tilde{\beta}_x$ are broken, and hence we obtain finite $F(\phi_0)$. Similar arguments apply to other ϕ_0 values. In the following, we will show the resulting domain wall dynamics.

We next solve the equation of motion. For $\delta = 0$, $\tau(\phi_0)$ is well fitted by $\tau(\phi_0) \simeq \tau_0 + \tau_1 \cos 2\phi_0$, and $F(\phi_0) = 0$ as shown in Fig. 2.2 (d), (e). Note that such ϕ_0 dependence of $\tau(\phi_0)$ arises from the triplet pairing. With this $\tau(\phi_0)$, we have solved Eqs. (2.4.2) and (2.4.3). Fig. 2.3 (a) shows the averaged velocity after sufficiently long time, and there is a threshold current density. It is given by $j_c = \frac{1}{\sqrt{\tau_0^2 - \tau_1^2}}$, which is obtained from Eqs. (2.4.2) and (2.4.3) with $\tau(\phi_0) = \tau_0 + \tau_1 \cos 2\phi_0$ and $F(\phi_0) = 0$. As shown in Fig. 2.3 (c), $\dot{X}$ is zero after sufficiently long time for $j_x < j_c$ because of the intrinsic pinning due to the anisotropy

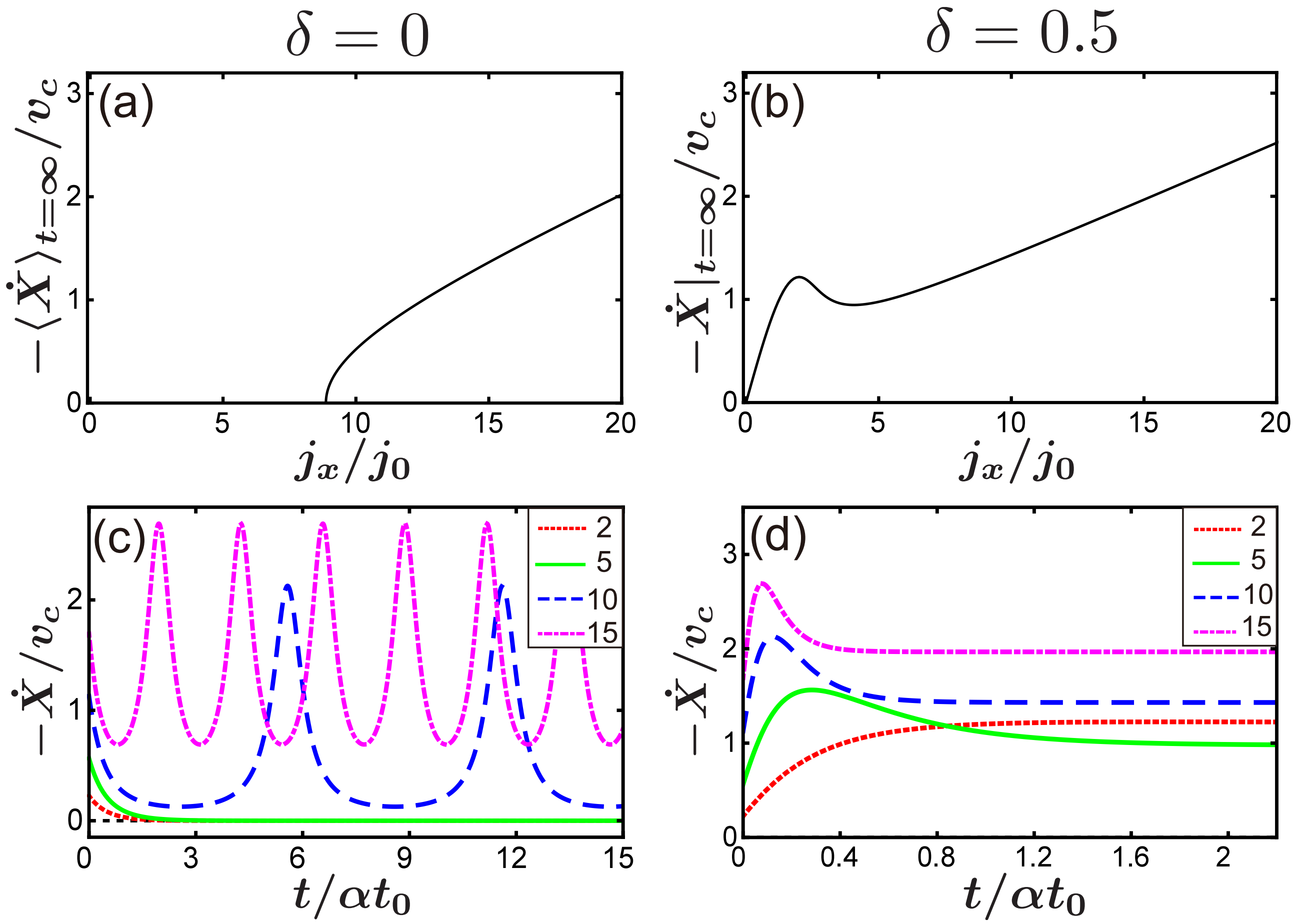

Figure 2.3: Velocity of a domain wall center for $\delta = 0$ in (a) and (c), and for $\delta = 0.5$ in (b) and (d). (a) shows the velocity averaged over the oscillation period after sufficiently long time, and (b) shows the velocity after sufficiently long time. In (c) and (d), the time evolution of the velocity for different j_x/j_0 (indicated by different colors) is presented. We have set $\alpha = 10^{-4}$, and the initial conditions are $\phi_0(t = 0) = \pi$ and $\dot{X}(t = 0)$.

$K_\perp$. With a larger current density ($j_x > j_c$), the domain wall center oscillates with a finite drift velocity. The above behavior is similar to a domain wall motion in normal ferromagnetic metals without the non-adiabatic torque.

We now consider the case with $\delta \neq 0$. As shown in Fig. 2.2 (d) and (e), $\tau(\phi_0)$ and $F(\phi_0)$ are well fitted by

$$\tau(\phi_0) \simeq \tau_0 + \tau_1 \cos 2\phi_0, \tag{2.4.6}$$

$$F(\phi_0) \simeq F_0 \cos \phi_0. \tag{2.4.7}$$

Importantly, we have finite $F(\phi_0)$ when $\delta \neq 0$. As shown in Sec. 2.6.2, finite $d^x(\boldsymbol{k})d^z(\boldsymbol{k})$ and $d^y(\boldsymbol{k})d^z(\boldsymbol{k})$ are necessary to have finite $F(\phi_0)$.

This $F(\phi_0)$ changes the domain wall motion drastically. As shown in Fig. 2.3(b), there is no threshold current density for driving the steady motion, which is similar to a situation in normal metals with the non-adiabatic torque. An important difference from conventional STT is that a domain wall shows no oscillatory motions ($\ddot{X} = \dot{\phi} = 0$) even for a large current density depending on α. According to Eqs. (2.4.3), oscillation occurs for $j > j_{\max} = \max_{\phi_0} \{\alpha \sin 2\phi_0/(\alpha\tau(\phi_0) - F(\phi_0))\}$. With the numerically obtained parameters in Eqs. (2.4.6) and (2.4.7), $j_{\max}$ is infinite when α is small enough ($\alpha \lesssim 10^{-3} \sim |\Delta_0|^2/t^2$) because $\alpha\tau(\phi_0) - F(\phi_0)$ can be zero. In contrast, for conventional STT, $j_{\max}$ is always finite since $\tau(\phi_0)$ and $F(\phi_0)$ do not depend on ϕ_0, and oscillatory motion always appears for a current density larger than $j_{\max}$. The absence of oscillatory motion is important for an efficient manipulation of a domain wall. Let us estimate the required supercurrent density. For example, in a ferromagnetic nanowire $Ni_{81}Fe_{19}$, an experimental value is $S^2K_\perp\lambda a^{-3} \sim 0.05$ J/m^2[123], and hence $v_c \simeq 3 \times 10^2$m/s and $j_0 \sim 4 \times 10^{13}$A/m^2. The required current density to achieve $\dot{X} \simeq 0.4$ μm/s is $j_x \simeq 10^5$A/m^2, which is lower than the critical current density in typical ferromagnetic Josephson junctions[124].

2.5 Summary and discussion

To summarize, we have microscopically derived STT induced by triplet supercurrents. We showed that spin-triplet pairings give novel types of STT, which can be used for an efficient control of a domain wall. The results can be applied to different d vectors and magnetic textures such as a skyrmion, and we expect the possibilities for more interesting aspects of triplet supercurrent-induced STT.

There are several comments and discussions. In normal metals, a voltage drop occurs due to the domain wall motion[125, 126, 127, 128] in addition to the resistance of a sample. For a superconducting system, while a supercurrent (dc current) is not accompanied by the voltage drop, the motion of a domain wall would also cause time evolution of the phase, and it might result in a finite voltage drop. In this work, we have assumed such fluctuation is small compared to the overall phase gradient.

In this work, we did not consider the Abrikosov vortices in a superconductor, which might be induced by the stray field of the ferromagnet. These vortices can cause voltage drop due to their dynamics and a non-uniform current pattern. To suppress the vortices, we can use junctions with a ferromagnet with a small stray field, e.g., Sr_2RuO_4/permalloy junction with magnetization oriented in-plane. We can also use a singlet superconductor with a high critical field [18] such as niobium, and hence Nb/Ho/permalloy junction is another possible setup.

When the superconducting pairing is proximity-induced, in general, singlet pairing is expected to be mixed. However, the decay length of the singlet proximity effect is much shorter than that of the equal spin triplet pairing for a large exchange coupling. Furthermore, the contribution from singlet pairing to STT is much smaller than that from triplet pairing in the adiabatic regime, which is justified in a smooth magnetic texture.

2.6 Details

In this section, we present the derivation and more detailed discussion on this chapter.

2.6.1 Derivation of spin torque

We show the derivation of Eq. (2.3.6). The model is described by the following action.

$$S = -\frac{1}{2} \sum_{n,\boldsymbol{k},\boldsymbol{q}} \tilde{\Psi}^{\dagger}_{\boldsymbol{k}+\boldsymbol{q}}(i\epsilon_n)(\mathcal{G}^{-1}_{\mathrm{tot}})_{\boldsymbol{k}+\boldsymbol{q},\boldsymbol{k}}(i\epsilon_n)\tilde{\Psi}_{\boldsymbol{k}}(i\epsilon_n), \tag{2.6.1}$$

where

$$\tilde{\Psi}_{\boldsymbol{k}}(i\epsilon_n) = \begin{pmatrix} a_{\boldsymbol{k}+\boldsymbol{\kappa}\uparrow}(i\epsilon_n) \\ a_{\boldsymbol{k}+\boldsymbol{\kappa}\downarrow}(i\epsilon_n) \\ a^{\dagger}_{-\boldsymbol{k}+\boldsymbol{\kappa}\uparrow}(-i\epsilon_n) \\ a^{\dagger}_{-\boldsymbol{k}+\boldsymbol{\kappa}\downarrow}(-i\epsilon_n) \end{pmatrix}, \tag{2.6.2}$$

$$(\mathcal{G}^{-1}_{\mathrm{tot}})_{\boldsymbol{k}+\boldsymbol{q},\boldsymbol{k}}(i\epsilon_n) \simeq \mathcal{G}^{-1}_{\boldsymbol{k}}\delta_{\boldsymbol{q},\boldsymbol{0}} + U^{(1)}_{\boldsymbol{k}+\boldsymbol{q},\boldsymbol{k}} + U^{(2)}_{\boldsymbol{k}+\boldsymbol{q},\boldsymbol{k}}. \tag{2.6.3}$$

Here we define

$$U^{(1)}_{\boldsymbol{k}+\boldsymbol{q},\boldsymbol{k}} = -v^{\nu}_{\boldsymbol{k}}\kappa_{\nu}\delta_{\boldsymbol{q},\boldsymbol{0}}\mathbb{I}_4 - v^{\mu}_{\boldsymbol{k}+\boldsymbol{q}/2}A^a_{\mu}(\boldsymbol{q})\begin{pmatrix} \sigma_a & 0 \\ 0 & \sigma^T_a \end{pmatrix}, \tag{2.6.4}$$

$$U^{(2)}_{\boldsymbol{k}+\boldsymbol{q},\boldsymbol{k}} = -\frac{\partial \xi_{\boldsymbol{k}+\boldsymbol{q}/2}}{\partial k_{\mu}\partial k_{\nu}}\kappa_{\nu}A^a_{\mu}(\boldsymbol{q})S^a, \tag{2.6.5}$$

and $\mathcal{G}^{-1}_{\boldsymbol{k}}$ is defined using Eq. (2.3.9). To restore the gauge invariance, we need to include the vector potential $\boldsymbol{A}$ and redefine $\tilde{\boldsymbol{\kappa}} = \boldsymbol{\kappa} + \frac{e}{c}\boldsymbol{A}$. Assuming the supercurrent, $\boldsymbol{j} \propto \tilde{\boldsymbol{\kappa}}$, is homogeneous, we can apply the perturbation with respect to $\tilde{\boldsymbol{\kappa}}$ in the same way.

The spin density under a superconducting current is given by

$$\tilde{s}^a_{\boldsymbol{q}} = \frac{T}{2N}\frac{1}{2}\sum_{\boldsymbol{k},n} \mathrm{tr}[S^a \mathcal{G}_{\mathrm{tot},\boldsymbol{k}+\boldsymbol{q},\boldsymbol{k}}(i\varepsilon_n)]. \tag{2.6.6}$$

We calculate it to the linear order of κ_ν and $A^a_\mu(\boldsymbol{q})$, and obtain $\delta\tilde{s}^a_{\boldsymbol{q}} = \pi^{ab}_{\mu\nu}A^b_\mu(\boldsymbol{q})\frac{j_\nu}{2en_e}$. Here

$$\pi^{ab}_{\mu\nu} = \lim_{\boldsymbol{q}\to\boldsymbol{0}} \frac{-T}{4Nta^2}\sum_{n,\boldsymbol{k}} \frac{\partial^2 \xi_{\boldsymbol{k}}}{\partial k_\mu \partial k_\nu} \mathrm{Tr}[S^a \mathcal{G}_{\boldsymbol{k}+\boldsymbol{q}}(i\epsilon_n) S^b \mathcal{G}_{\boldsymbol{k}}(i\epsilon_n)] + \delta^{ab} L^a_{\mu\nu}, \tag{2.6.7}$$

where

$$L^x_{\mu\nu} = L^y_{\mu\nu} = \frac{1}{2J_{\mathrm{sd}}Sta^2}\frac{1}{N}\sum_{\boldsymbol{k}} v^\mu_{\boldsymbol{k}} v^\nu_{\boldsymbol{k}} \left(\left.\frac{\partial n_F(\varepsilon)}{\partial \varepsilon}\right|_{\varepsilon=E^\uparrow_{\boldsymbol{k}}} - \left.\frac{\partial n_F(\varepsilon)}{\partial \varepsilon}\right|_{\varepsilon=E^\downarrow_{\boldsymbol{k}}} \right), \tag{2.6.8}$$

$$L^z_{\mu\nu} = \frac{-1}{2ta^2}\frac{1}{N}\sum_{\boldsymbol{k}} v^\mu_{\boldsymbol{k}} v^\nu_{\boldsymbol{k}} \sum_{\sigma=\uparrow,\downarrow} \frac{\xi^\sigma_{\boldsymbol{k}}}{E^\sigma_{\boldsymbol{k}}} \left.\frac{\partial n_F(\varepsilon)}{\partial \varepsilon}\right|_{\varepsilon=E^\sigma_{\boldsymbol{k}}} (2n_F(E^\sigma_{\boldsymbol{k}}) - 1), \tag{2.6.9}$$

with $E^\uparrow_{\boldsymbol{k}} = \sqrt{(\xi_{\boldsymbol{k}} - J_{\mathrm{sd}}S)^2 + |\Delta^\uparrow_{\boldsymbol{k}}|^2}$, $E^\downarrow_{\boldsymbol{k}} = \sqrt{(\xi_{\boldsymbol{k}} + J_{\mathrm{sd}}S)^2 + |\Delta^\downarrow_{\boldsymbol{k}}|^2}$, and $n_F(\varepsilon) = (e^{\varepsilon/T}+1)^{-1}$. $L^a_{\mu\nu}$ are the contributions from the Fermi surface; they are proportional to the derivative of $n_F(\varepsilon)$ and vanishingly small at low temperatures in systems with a full gap or point nodes. In Eq. (2.3.10), we neglect $L^a_{\mu\nu}$ considering a low temperature compared to the superconducting critical temperature. We note that for $\Delta(\boldsymbol{k}) = 0$, two terms in Eq. (2.6.7) cancel each other and $\pi^{ab}_{\mu\nu} = 0$.

According to Eq. (2.3.12), finite $\frac{1}{2}(\pi^{xx}_\mu - \pi^{yy}_\mu)$ or π^{xy}_μ are necessary for $\tilde{\beta}_\mu \neq 0$, and they depend on the relative phase between $\Delta^\uparrow_{\boldsymbol{k}}$ and $\Delta^\downarrow_{\boldsymbol{k}}$ as

$$\frac{1}{2}(\pi^{xx}_\mu - \pi^{yy}_\mu) = \lim_{\boldsymbol{q}\to 0}\frac{T}{Nta^2}\sum_{\boldsymbol{k},n}\frac{\partial^2 \xi_{\boldsymbol{k}+\boldsymbol{q}/2}}{\partial^2 k_\mu}\left(\frac{\mathrm{Re}(\Delta^\downarrow_{\boldsymbol{k}+\boldsymbol{q}}\Delta^{\uparrow *}_{\boldsymbol{k}})}{(\epsilon_n^2 + E^{\downarrow 2}_{\boldsymbol{k}+\boldsymbol{q}})(\epsilon_n^2 + E^{\uparrow 2}_{\boldsymbol{k}})}\right), \tag{2.6.10}$$

$$= \lim_{\boldsymbol{q}\to 0}\frac{1}{N}\sum_{\boldsymbol{k}} \mathrm{Re}(\Delta^\downarrow_{\boldsymbol{k}}\Delta^{\uparrow *}_{\boldsymbol{k}}) f_\mu(\boldsymbol{k},\boldsymbol{q}), \tag{2.6.11}$$

$$\pi^{xy}_\mu = \lim_{\boldsymbol{q}\to 0}\frac{T}{Nta^2}\sum_{\boldsymbol{k},n}\frac{\partial^2 \xi_{\boldsymbol{k}+\boldsymbol{q}/2}}{\partial^2 k_\mu}\left(\frac{\mathrm{Im}(\Delta^\downarrow_{\boldsymbol{k}+\boldsymbol{q}}\Delta^{\uparrow *}_{\boldsymbol{k}})}{(\epsilon_n^2 + E^{\downarrow 2}_{\boldsymbol{k}+\boldsymbol{q}})(\epsilon_n^2 + E^{\uparrow 2}_{\boldsymbol{k}})}\right). \tag{2.6.12}$$

$$= \lim_{\boldsymbol{q}\to 0}\frac{1}{N}\sum_{\boldsymbol{k}} \mathrm{Im}(\Delta^\downarrow_{\boldsymbol{k}}\Delta^{\uparrow *}_{\boldsymbol{k}}) f_\mu(\boldsymbol{k},\boldsymbol{q}), \tag{2.6.13}$$

where

$$f_\mu(\boldsymbol{k},\boldsymbol{q}) = \frac{T}{ta^2}\sum_n \frac{\partial^2 \xi_{\boldsymbol{k}+\boldsymbol{q}/2}}{\partial^2 k_\mu}\frac{1}{(\epsilon_n^2 + E^{\downarrow 2}_{\boldsymbol{k}+\boldsymbol{q}})(\epsilon_n^2 + E^{\uparrow 2}_{\boldsymbol{k}})}. \tag{2.6.14}$$

2.6.2 Finite β term in domain wall manipulation

The explicit form of $F(\phi_0)$ in a domain wall configuration when $d^\mu(\boldsymbol{k}) \in \mathbb{R}$. We have

$$F(\phi_0) = \frac{|\Delta_0|^2 a^4}{2ev_c S} \sum_i \partial_x n^z \lim_{\boldsymbol{q}\to\boldsymbol{0}} \frac{1}{N} \sum_{\boldsymbol{k}} f_x(\boldsymbol{k},\boldsymbol{q}) \left[d^y(\boldsymbol{k}) d^z(\boldsymbol{k}) \sin\phi_0 - d^x(\boldsymbol{k}) d^z(\boldsymbol{k}) \cos\phi_0\right] \sin\theta$$
$$+ \frac{|\Delta_0|^2 a^4}{2ev_c S} \sum_i \partial_x n^z \lim_{\boldsymbol{q}\to\boldsymbol{0}} \frac{1}{N} \sum_{\boldsymbol{k}} f_x(\boldsymbol{k},\boldsymbol{q}) \left[-\frac{1}{2}\left(d^x(\boldsymbol{k})^2 - d^y(\boldsymbol{k})^2\right) \sin(2\phi_0) + d^x(\boldsymbol{k}) d^y(\boldsymbol{k}) \cos(2\phi_0)\right] \cos\theta, \tag{2.6.15}$$

where we have used Eq. (2.3.3).

In the following, we show that $F(\phi_0) = 0$ for $\boldsymbol{d}(\boldsymbol{k}) = (-\sin(k_y a), \sin(k_x a), 0)$. The first line in Eq. (2.6.15) is zero since $d^z(\boldsymbol{k}) = 0$. We note that in a domain wall configuration, $\theta(x) = \pi - \theta(-x)$ is satisfied. Since $f_x(\boldsymbol{k},\boldsymbol{q})$, which depends on $\boldsymbol{n}$ through $|\Delta_{\boldsymbol{k}}^\uparrow| = |\Delta_{\boldsymbol{k}}^\downarrow| = |\Delta_0|^2 |\boldsymbol{d}(\boldsymbol{k}) \times \boldsymbol{n}|$ in $E_{\boldsymbol{k}}^\sigma$, and $\partial_x n^z$ are invariant under the spatial reflection ($\theta \to \pi - \theta$), the second line in Eq. (2.6.15) vanishes after the spatial summation $\sum_i$.

For $F(\phi_0) \neq 0$, finite $d^x(\boldsymbol{k}) d^z(\boldsymbol{k})$ or $d^y(\boldsymbol{k}) d^z(\boldsymbol{k})$ is necessary. In this case, the first line in Eq. (2.6.15) is nonzero, and $|\boldsymbol{d}(\boldsymbol{k}) \times \boldsymbol{n}|$ changes its value under $\theta \to \pi - \theta$ so that the second term is also nonzero in general. As we show in the previous sections, $\boldsymbol{d}(\boldsymbol{k}) = (-\sin(k_y a). \sin(k_x a), \delta \sin(k_x a))$ is one way to satisfy this condition.

Chapter 3

Chiral magnet in proximity to singlet superconductor

In this chapter, we consider a cubic chiral magnet in proximity to a singlet superconductor. The cubic chiral magnets MnSi and $\mathrm{Fe}_x\mathrm{Co}_{1-x}\mathrm{Si}$ are known to show a skyrmion crystal phase owing to the lack of inversion symmetry of the crystal. We show that, in the presence of the superconducting proximity effect, a singlet supercurrent exerts a spin-torque on a skyrmion and can drive the motions. Furthermore, we also show that Weyl quasiparticles exist in the BdG spectrum, and the Weyl points can be controlled by the magnetization. We show that the tilt of the Weyl cones can be tuned by the strength of the spin-orbit coupling, and propose a possible realization of type-II Weyl points.

This chapter is organized as follows. In Sec. 3.1, we give the background and present the aim of this study. In Sec. 3.2, we show our results on the spin-orbit torque induced by a supercurrent. We first introduce the model which describes a cubic chiral magnet with proximity-induced superconductivity. Then, using a linear response theory, we calculate spin polarization induced by a supercurrent, which acts as a local spin torque. In Sec. 3.3, we show that the torque can drive motions of skyrmions. In Sec. 3.4, we study the band structure of Bogoliubov quasiparticles, and demonstrate how type-I (conventional) and type-II Weyl points appear. We also discuss the effect of inhomogeneity in spin textures. In Sec. 3.5, we give the summary and discussions. Section 3.6 provides the details of the calculations in this chapter.

3.1 Introduction to this chapter

As we have already introduced in Sec. 1.2.3, topological structures in electronic states exhibit interesting features. Topological insulators have surface Dirac cones and show the magnetoelectric polarizability[129, 130]. In metallic systems, Weyl points in a band structure are predicted to produce a variety of phenomena such as Fermi-arc surface states, chiral anomaly, and unusual anomalous Hall effects [31, 34, 35, 131, 132, 36, 133, 134, 135, 136, 137, 138, 139]. Two non-degenerate energy bands linearly cross at isolated points in the momentum space (Weyl nodes), and they are the source or sink of the Berry curvature, which is the origin of the anomalous Hall effect. Weyl nodes are achieved in a material by breaking either time reversal or inversion symmetry.

Recently, it has been shown that Weyl semimetals can be classified into two categories: type-I and type-II Weyl semimetals. A type-I Weyl semimetal is a conventional Weyl semimetal. The number of candidate materials is still increasing. For materials that break inversion symmetry, the TaAs family compounds that include TaP, NbAs, and NbP are reported to have Weyl points [140, 141, 142]. For materials with broken time reversal symmetry, the antiferromagnetic Heusler compounds GdPtBi [143] and the noncollinear antiferromagnet Mn_3Sn [144] are also reported to have Weyl points. In a type-II Weyl semimetal, the dispersion is strongly tilted so that it has a finite density of states at each Weyl point. Type-II Weyl semimetals have been proposed to exist in layered transition metal dichalcogenides such as WTe_2 [145, 146, 147] and $MoTe_2$ [148, 149], and LaAlGe [150], Type-II Weyl semimetals are predicted to have peculiar properties[151, 152, 153, 154, 155, 156, 157]; chiral anomaly depending on the relative direction of the field and tilt[154], and a non-analytic behavior in the anomalous Hall effect[155], etc.

Topological structures in Bogoliubov quasiparticle states also show unusual features as we have introduced in Sec. 1.2.3 [29, 30]. Realization of Weyl superconductors are proposed in several materials. ^{3}He-A phase is the oldest example of Weyl superfluid. In an artificially engineered setup, it has been proposed that multilayers of magnetically doped topological insulators and s-wave superconductors realize a Weyl superconducting state [55]. In materials, URu_2Si_2 [56] and B-phase of UPt_3 [158] are also proposed as Weyl superconductors.

For topological structures in a *spin texture*, of particular recent interest is a magnetic skyrmion[159, 65, 67, 66, 69, 160], which is defined by an integer topological number. Skyrmions are experimentally observed in cubic chiral magnets such as cubic B20 compounds MnSi and $Fe_{0.5}Co_{0.5}Si$. Their topological structure gives rise to Magnus force that acts on a skyrmion like a Lorentz force[161]. When electrons coupled to skyrmions, the so-called emergent electromagnetic field acts on electrons [126, 160]. Skyrmions have received attentions also as a promising candidate of a future information career (c.f. Sec. 1.3.2). Magnus force prevents a skyrmion from being pinned by impurities or lattice defects, and the threshold current density to drive its motion is quite low compared to that of a domainwall [162, 163, 164, 165, 166, 167].

Such current-induced magnetization dynamics has been studied intensively in the field of spintronics. A spin transfer torque[85, 168, 86, 169] is one type of current-induced spin torques, which requires noncolinear spin textures. SO coupling realizes another type of current-induced torque, so called SO torque[98, 99, 100, 101, 102], which can also drive domain walls[170] or skyrmions via applied currents[171, 172].

In this chapter, we consider a cubic chiral magnet (e.g. MnSi and $Fe_{0.5}Co_{0.5}Si$) in proximity to an s-wave superconductor. We show that this system shows rich physics in terms of topological states and spintronics. We point out two interesting properties in this system: spin torque induced by a singlet supercurrent and Weyl Bogoliubov quasiparticles. The summary of the results are the following.

- A singlet supercurrent can also exert a spin-torque with the aid of the SO coupling in chiral magnets. From the symmetry point of view, it can be written as $H_{so} = \alpha_{so}\boldsymbol{k}\cdot\boldsymbol{\sigma}$ around Γ point with $\boldsymbol{\sigma}$ being the pauli matrices acting on the spin space. This SO coupling plays a crucial role in chiral magnets, since it leads to Dzyaloshinskii-Moriya interaction, which is the origin of the noncollinear magnetic orders such as helical spin orders and skyrmion crystal phases. With the SO coupling, we calculate a spin polarization and a resulting spin-torque, which are induced by supercurrents.

- We point out that the Bogoliubov quasiparticle band has a pair of Weyl points. Their positions in the Brillouin zone are determined by the direction of magnetization. Consequently, inhomogeneous spin textures realize an effective magnetic field acting on Bogoliubov quasiparticles. Furthermore, the tilt of the Weyl cones can also be tuned by the strength of the SO coupling. We propose a realization of type-II Weyl points in the quasiparticle spectrum and show the phase diagram, which includes a phase transition between conventional (type-I) Weyl points and type-II Weyl points. We expect intriguing transport properties of quasipaticles to be realized in our system.

3.2 Spin-orbit torque induced by supercurrent

3.2.1 Model

We consider a heterostructure composed of an s-wave superconductor and a cubic chiral magnet (Fig. 3.1), which is modeled by the following BdG Hamiltonian using the basis given by Eq. 1.2.5.

$$H(\boldsymbol{k}) = \begin{pmatrix} \hat{H}_N(\boldsymbol{k}) & \Delta(i\sigma_y) \\ \Delta^*(i\sigma_y)^\dagger & -\hat{H}_N(-\boldsymbol{k})^{\mathrm{T}} \end{pmatrix}, \tag{3.2.1}$$

with the normal part of the Hamiltonian

$$\hat{H}_N(\boldsymbol{k}) = (\varepsilon_{\boldsymbol{k}} - \mu)\,\mathbf{1} - JM\boldsymbol{n}\cdot\boldsymbol{\sigma} + \alpha_{so}\boldsymbol{g}(\boldsymbol{k})\cdot\boldsymbol{\sigma}, \tag{3.2.2}$$

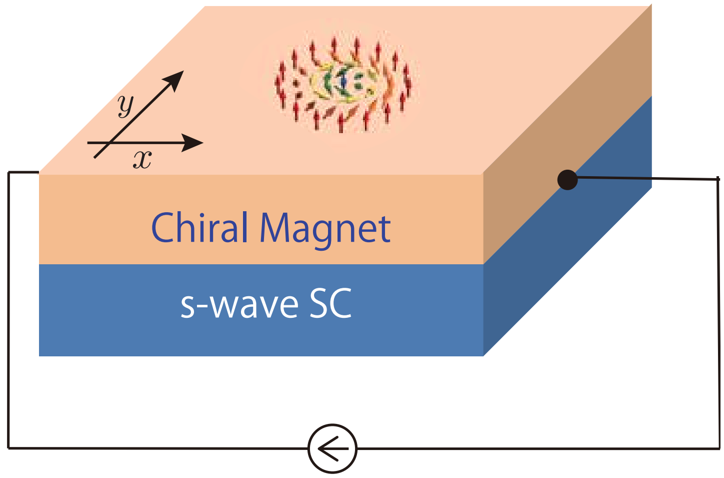

Figure 3.1: Heterostructure composed of a chiral magnet and an s-wave superconductor.

where $\varepsilon_{\boldsymbol{k}} = -t\sum_{\ell=\{x,y,z\}}\cos(k_\ell a)$ is a hopping energy with the lattice constant a and the hopping amplitude t. The chemical potential is denoted by μ, the exchange coupling coefficient is J, and the localized magnetic moment is denoted by $M\boldsymbol{n}$ with the unit vector $\boldsymbol{n} = (\cos\phi\sin\theta, \sin\phi\sin\theta, \cos\theta)$. We assume the characteristic length of spatial variation to be much longer than the coherence length of superconductivity and the Fermi wave length, so that $\boldsymbol{n}(\boldsymbol{r})$ can be regarded as being locally homogeneous. The effect of the inhomogeneity will be discussed in Sec. 3.4.2.

The SO coupling in a cubic lattice model can be written as

$$\boldsymbol{g}(\boldsymbol{k}) = (\sin(k_x a), \sin(k_y a), \sin(k_z a)), \tag{3.2.3}$$

which reflects the symmetry of cubic chiral magnets whose point group symmetry is T. The proximity induced superconductivity is given by Δ, where we take s-wave singlet pairings. The SO coupling supports the proximity of the superconductivity because it causes the tilt of the spin orientation in momentum space.

3.2.2 Calculation of spin-torque

Using the BdG Hamiltonian [Eq. (3.2.1)], one can calculate the spin polarization density of the system as

$$s_\mu = \frac{1}{2}\frac{1}{V}\sum_{\boldsymbol{k},n} n_F(\varepsilon_{n\boldsymbol{k}})\langle n\boldsymbol{k}|\hat{S}_\mu|n\boldsymbol{k}\rangle, \tag{3.2.4}$$

where $|n\boldsymbol{k}\rangle$ and $\varepsilon_{n\boldsymbol{k}}$ are the eigenstates and eigenenergy of the BdG Hamiltonian with the band indices $n = \{0,1,2,3\}$. $n_F(\varepsilon_{n\boldsymbol{k}})$ is the Fermi distribution function, and V is the volume.

The spin operator is given by

$$\hat{S}_\mu = \frac{\hbar}{2}\begin{pmatrix}\sigma_\mu & 0\\ 0 & -\sigma_\mu^T\end{pmatrix}. \tag{3.2.5}$$

Now we consider a state with a finite supercurrent density $\boldsymbol{j} = -\frac{e}{m}n_s\hbar\boldsymbol{\kappa}$ where m is an electron mass, n_s is the superfluid density, $\boldsymbol{q}$ is the shift of the Fermi surface, and $-e$ is the electron charge. With a perturbation theory, the leading correction to the polarization is obtained as

$$\delta s_\mu = K_{\mu\nu} j_\nu, \tag{3.2.6}$$

where

$$K_{\mu\nu} = -\frac{m}{2e\hbar n_s}\lim_{\boldsymbol{q}'\to 0}\frac{1}{V}\sum_{\boldsymbol{k}}\sum_{n,m}\frac{n_F(\varepsilon_{n\boldsymbol{k}}) - n_F(\varepsilon_{m\boldsymbol{k}+\boldsymbol{q}'})}{\varepsilon_{m\boldsymbol{k}+\boldsymbol{q}'} - \varepsilon_{n\boldsymbol{k}}}\langle n\boldsymbol{k}|\hat{S}_\mu|m\boldsymbol{k}\rangle\langle m\boldsymbol{k}|\hat{V}_\nu|n\boldsymbol{k}\rangle, \tag{3.2.7}$$

and the velocity operator $\hat{V}_\mu$ is defined by

$$\hat{V}_\mu = \begin{pmatrix}\left.\frac{\partial \hat{H}_N}{\partial k_\mu}\right|_{\boldsymbol{k}} & 0\\ 0 & -\left(\left.\frac{\partial \hat{H}_N}{\partial k_\mu}\right|_{-\boldsymbol{k}}\right)^{\mathrm{T}}\end{pmatrix}. \tag{3.2.8}$$

As shown in Sec. 3.6.1, Eq. (3.2.7) is obtained by calculating the spin polarization using states with the finite center of mass momentum $\boldsymbol{\kappa}$ and expanding it in powers of $\boldsymbol{\kappa}$ [173, 174].

3.2.3 Limiting cases

In chiral magnets, due to the large exchange splitting, $\alpha_{so} \ll JM$ is expected, but we first consider two limiting cases to provide an intuitive picture. In the limit of $JM/\alpha_{so} \to 0$, the anisotropy due to the spin polarization $\boldsymbol{n}$ can be neglected. In this case, a symmetry argument straightforwardly leads to the relative orientation between $\delta\boldsymbol{s}$ and $\boldsymbol{j}$. The point group symmetry T leads to $K_{\mu\nu} = K\delta_{\mu\nu}$ [1], and we obtain

$$\delta\boldsymbol{s} = K\boldsymbol{j}, \tag{3.2.9}$$

i.e., the spin polarization is induced in parallel to the supercurrent. This relation is in contrast with the case of Rashba SO coupling (e.g., C_{4v}) that gives $\delta\boldsymbol{s} \propto \hat{\boldsymbol{z}} \times \boldsymbol{j}$.

In the limit of $\alpha_{so} \ll JM$, $K_{\mu\nu}$ depends on the direction of $\boldsymbol{n}$. In particular, assuming $\{JM, |\mu|\} \gg \{t, \alpha_{so}, \Delta\}$, we perform a perturbative approach. We first apply a unitary transformation, $U(\boldsymbol{k})$, on the BdG Hamiltonian (Eq. (3.2.1)), which acts on both spin space

[1] C_2 rotational symmetry in point group T prohibits the off-diagonal components in $K_{\mu\nu}$, and C_3 rotational symmetry makes the diagonal components the same.

and particle-hole space. (The detail is in Sec. 3.6 .) It diagonalizes the Hamiltonian up to the required order of a small parameter ϵ defined by $\{t, \alpha_{so}, \Delta\} \sim \epsilon JM$, and we expand the Hamiltonian to the second order of ϵ as

$$U^\dagger(\boldsymbol{k})H(\boldsymbol{k})U(\boldsymbol{k}) = H_0'(\boldsymbol{k}) + H_1'(\boldsymbol{k}), \tag{3.2.10}$$

where the diagonal matrix $H_0'(\boldsymbol{k})$ reads

$$H_0'(\boldsymbol{k}) = \mathrm{diag}(E_{0\boldsymbol{k}}, E_{1\boldsymbol{k}}, E_{2\boldsymbol{k}}, E_{3\boldsymbol{k}}) \tag{3.2.11}$$

with

$$E_{0\boldsymbol{k}} = \varepsilon_{\boldsymbol{k}} - \mu - (JM - \alpha_{so}\boldsymbol{g}(\boldsymbol{k}) \cdot \boldsymbol{n}), \tag{3.2.12}$$
$$E_{1\boldsymbol{k}} = \varepsilon_{\boldsymbol{k}} - \mu + (JM - \alpha_{so}\boldsymbol{g}(\boldsymbol{k}) \cdot \boldsymbol{n}), \tag{3.2.13}$$
$$E_{2\boldsymbol{k}} = -(\varepsilon_{\boldsymbol{k}} - \mu) + (JM + \alpha_{so}\boldsymbol{g}(\boldsymbol{k}) \cdot \boldsymbol{n}), \tag{3.2.14}$$
$$E_{3\boldsymbol{k}} = -(\varepsilon_{\boldsymbol{k}} - \mu) - (JM + \alpha_{so}\boldsymbol{g}(\boldsymbol{k}) \cdot \boldsymbol{n}), \tag{3.2.15}$$

and, every matrix element in $H_1'(\boldsymbol{k})$ is of the order of ϵ^2. For now we consider $\mu \sim -JM$, and project the Hilbert space to a space spanned by two eigenstates of $H_0'(\boldsymbol{k})$ with eigenenergies $E_{0\boldsymbol{k}}$ and $E_{2\boldsymbol{k}}$, noting that $E_{3\boldsymbol{k}} \ll \{E_{0\boldsymbol{k}} \sim E_{2\boldsymbol{k}} \sim 0\} \ll E_{1\boldsymbol{k}}$. After the projection, we obtain an effective BdG Hamiltonian $H_0'(\boldsymbol{k}) + H_1'(\boldsymbol{k}) \mapsto H_{\mathrm{eff}}(\boldsymbol{k})$, which is a 2×2 matrix.

We then use the effective Hamiltonian $H_{\mathrm{eff}}(\boldsymbol{k})$ to calculate $K_{\mu\nu}$ [Eq. (3.2.7)]. The detailed structure of the quasiparticle states is discussed in Sec. 3.4. We define the eigenstates of $H_{\mathrm{eff}}(\boldsymbol{k})$ as $||\pm, \boldsymbol{k}\rangle$, whose eigenenergies are $\varepsilon_{\pm,\boldsymbol{k}}$. The spin and velocity operators in the projected space are defined as $U^\dagger(\boldsymbol{k})\hat{S}_\mu U(\boldsymbol{k}) \mapsto \hat{S}_\mu^{\mathrm{eff}}$ and $U^\dagger(\boldsymbol{k})\hat{V}_\mu U(\boldsymbol{k}) \mapsto \hat{V}_\mu^{\mathrm{eff}}$. (The detail is in Sec. 3.6.)

For the calculation of a response against a supercurrent, the interband terms ($n \neq m$ in Eq. (3.2.7)) are important. The directional dependence of $K_{\mu\nu}$ is obtained from the matrix element:

$$\mathcal{S}_{\mu\nu} \equiv \langle -, \boldsymbol{k}||\hat{S}_\mu^{\mathrm{eff}}||+, \boldsymbol{k}\rangle\langle +, \boldsymbol{k}||\hat{V}_\nu^{\mathrm{eff}}||-, \boldsymbol{k}\rangle, \tag{3.2.16}$$
$$= \frac{a^2\hbar(JM + |\mu|)^2}{8(JM)^2\mu^2}\frac{\alpha_{so}^3|\Delta|^2k_\perp^2}{|\varepsilon_{+,\boldsymbol{k}} - \varepsilon_{-,\boldsymbol{k}}|^2}n_\mu n_\nu, \tag{3.2.17}$$
$$= \langle +, \boldsymbol{k}||S_\mu^{\mathrm{eff}}||-, \boldsymbol{k}\rangle\langle -, \boldsymbol{k}||V_\nu^{\mathrm{eff}}||+, \boldsymbol{k}\rangle, \tag{3.2.18}$$

to the lowest order of ϵ, where we consider momentum region that satisfies $|\boldsymbol{k}|a \ll 1$ and define $k_\perp^2 = k^2 - (\boldsymbol{k} \cdot \boldsymbol{n})^2$. Integration over the momentum space as

$$K_{\mu\nu} = -\frac{m}{e\hbar n_s}\int \frac{d^3\boldsymbol{k}}{(2\pi)^3}\frac{n_F(\varepsilon_{-,\boldsymbol{k}}) - n_F(\varepsilon_{+,\boldsymbol{k}})}{\varepsilon_{+,\boldsymbol{k}} - \varepsilon_{-,\boldsymbol{k}}}\mathcal{S}_{\mu\nu}, \tag{3.2.19}$$

leads to the relation $K_{\mu\nu} = K' n_\mu n_\nu$, i.e. the induced spin polarization is given by

$$\delta \boldsymbol{s} = K' \boldsymbol{n}(\boldsymbol{n} \cdot \boldsymbol{j}), \tag{3.2.20}$$

up to the lowest order in ϵ. The spin polarization is induced in parallel to $\boldsymbol{n}$, and it is not induced when the applied supercurrent is in perpendicular to $\boldsymbol{n}$. As we will see later, this term does not produce a spin torque since the spin torque is given by $\boldsymbol{n} \times \delta\boldsymbol{s}$. In the higher order of ϵ, other terms such as the form of Eq. (3.2.9) is expected to appear and leads to the spin torque, which is important for dynamics of skyrmions discussed below.

3.2.4 Numerical results

Next, we investigate the dependence of $K_{\mu\nu}$ on parameters and the direction of $\boldsymbol{n}$ for intermediate values of α_{so}/JM which interpolate two limiting cases considered in the previous subsection. For this purpose, we numerically calculate $K_{\mu\nu}$ with the BdG Hamiltonian in Eq. (3.2.1) and compare the results to the analytical asympotic results obtained in the last subsection. The main results in this subsection is as follows: (i) $K_{\mu\nu}$ depends on the direction of $\boldsymbol{n}$, and its dependence is well fitted by $K_{\mu\nu} = K^{(0)}\delta_{\mu\nu} + K^{(1)} n_\mu n_\nu$, which interpolates the asymptotic behaviors in the two limiting cases (Eq. (3.2.9) and Eq. (3.2.20)). (ii) The numerical results for $\alpha_{so}/JM \ll 1$ confirm the asymptotic form given in Eq. (3.2.20). (iii) $K_{\mu\mu}$ monotonically increase with increasing α_{so}, and $K_{\mu\mu}$ with μ in the direction parallel to $\boldsymbol{n}$ dominates over that with μ in the direction perpendicular to $\boldsymbol{n}$ for small α_{SO}/JM, in accordance with Eq. (3.2.20).

Fig. 3.2 and Fig. 3.3 show numerical results of the spin-polarization density per unit supercurrent density with the parameters, $t = 1.0$, $JM = 2.0$, $\Delta = 0.2$, $\mu = -4.8$. The lattice constant is $a = 10^{-1}$ nm and the London penetration depth $\lambda = 50$ nm. In Fig. 3.2, we show the dependence on α_{so} of K_{xx} and K_{zz} in the case with $\boldsymbol{n} = (0, 0, 1)$. K_{xx} and K_{zz} monotonically increase with increasing α_{so}, and the difference between them arises from the directional anisotropy due to $\boldsymbol{n}$, which is consistent with the asymptotic from Eq. (3.2.20) with $\boldsymbol{n} = (0, 0, 1)$; the magnitude of K_{xx} is suppressed compared to K_{zz} in the limit of $\alpha_{so}/JM \ll 1$. However, it is noted that, in contrast to Eq. (3.2.20) which implies zero K_{xx} for $\boldsymbol{n} = (0, 0, 1)$, K_{xx} is finite in Fig. 3.2 even for small values of α_{SO} because of the higher order terms neglected in Eq. (3.2.20) and also the continuum approximation.

In Fig. 3.3, we show the dependence of K_{xx} and K_{zx} on the direction of $\boldsymbol{n}$ rotating in xz plane. $\boldsymbol{n}$ is parametrized as $\boldsymbol{n} = (\sin\theta, 0, \cos\theta)$ with $0 \leq \theta \leq \pi$. The magnitude of K_{xx} and K_{zx} varies depending on θ, and their dependence is well fitted by $K_{\mu\nu} = K^{(0)}\delta_{\mu\nu} + K^{(1)} n_\mu n_\nu$, i.e. $K_{xx} = K^{(0)} + K^{(1)} \sin^2\theta$ and $K_{zx} = K^{(1)} \sin\theta\cos\theta$. Thus, the θ-dependence of $K_{\mu\nu}$ is qualitatively given by the sum of Eq. (3.2.9) and Eq. (3.2.20). In this calculation, we set $\alpha_{so} = 0.2$, and we note that the behaviors of the θ-dependence are not qualitatively changed by varying the value of α_{so}. Other components such as K_{xy} are calculated as well, and we

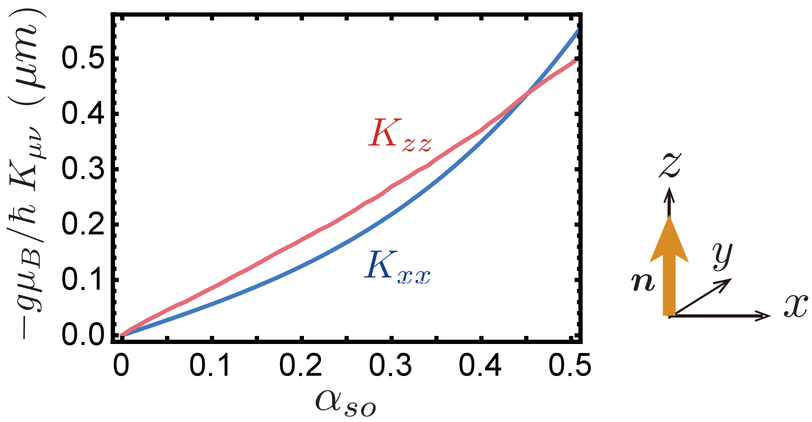

Figure 3.2: Dependence of K_{xx} and K_{zz} on the parameter α_{so} for $t = 1.0,\ JM = 2.0,\ \Delta = 0.2,\ \mu = -4.8$, when the direction of the localized spin is $\boldsymbol{n} = (0, 0, 1)$. Both K_{xx} and K_{zz} increase monotonically as α_{so} increases. In the limit of $\alpha_{so}/JM \ll 1$, the magnitude of K_{xx} is suppressed compared to K_{zz}, which is in agreement with the asymptotic form given by Eq. (3.2.20).

conclude that, in general, the dependence of $K_{\mu\nu}$ on $\boldsymbol{n}$ is qualitatively given by the sum of the two limiting cases, Eq. (3.2.9) and Eq. (3.2.20), for intermediate values of α_{so}/JM.

3.3 Skyrmion manipulation

Using the obtained results, we discuss skyrmion dynamics induced by supercurrents. We consider a heterostucture system with a supercurrent flow. Here we neglect the effect of normal currents, which would be suppressed in the presence of superconductivity. Our analysis is based on the Landau-Lifshtz-Gilbert equation for the localized spin $\boldsymbol{n}$,

$$\frac{d\boldsymbol{n}}{dt} = -\gamma \boldsymbol{n} \times \boldsymbol{H} - \alpha_G \boldsymbol{n} \times \frac{d\boldsymbol{n}}{dt} + \boldsymbol{T}, \tag{3.3.1}$$

where γ is the gyromagnetic ratio, $\boldsymbol{H}$ is the effective magnetic field given by the derivative of the free energy with respect to the magnetization, α_G is the Gilbert damping constant, and $\boldsymbol{T}$ is a supercurrent induced spin torque. We focus on a spin-orbit torque that originates from the spin polarization discussed in the last section. The spin polarization is given by the form $\delta \boldsymbol{s} = K^{(0)}\boldsymbol{j} + K^{(1)}\boldsymbol{n}(\boldsymbol{n} \cdot \boldsymbol{j})$, and it results in the following spin torque:

$$\boldsymbol{T} = \frac{JM}{\hbar^2} \boldsymbol{n} \times \delta \boldsymbol{s}, \tag{3.3.2}$$

$$= \frac{JMK^{(0)}}{\hbar^2} \boldsymbol{n} \times \boldsymbol{j}, \tag{3.3.3}$$

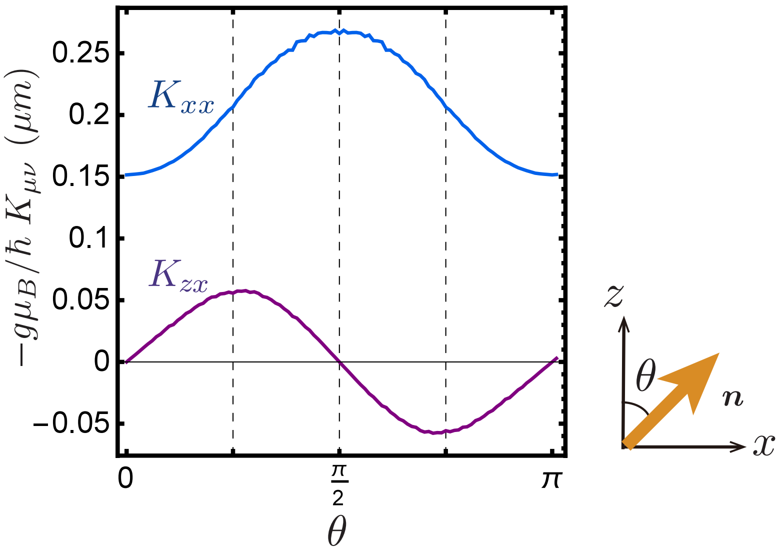

Figure 3.3: Dependence of K_{xx} and K_{zx} on the directional angle θ that parametrizes the localized spin as $\boldsymbol{n} = (\sin\theta, 0, \cos\theta)$. The parameters are set as $t = 1.0$, $JM = 2.0$, $\Delta = 0.2$, $\mu = -4.8$, and $\alpha_{so} = 0.2$. The diagonal component K_{xx} has an offset value that is independent of θ, and it is well fitted by $K_{xx} = 0.118n_x^2 + 0.150$. The off-diagonal component, K_{xy}, is fitted by $K_{xy} = 0.112n_xn_y$.

i.e., only $K^{(0)}\boldsymbol{j}$ acts as a spin torque, and the anisotropy due to $\boldsymbol{n}$ does not affect the spin torque even for large JM with the above form.

Dynamics of skyrmions is well described with the equation of motion of collective coordinates of a texture [82, 62, 175, 172]. Neglecting the deformation of skyrmions, we take the center of mass coordinate $\boldsymbol{R}(t)$ as the collective coordinate. The spin texture is given by $\boldsymbol{n}(\boldsymbol{r}, t) = \boldsymbol{n}^{sk}(\boldsymbol{r} - \boldsymbol{R}(t))$, where $\boldsymbol{n}^{sk}(\boldsymbol{r})$ is the spin configuration with a skyrmion at the origin. $\boldsymbol{n}_{sk}(\boldsymbol{r})$ has a finite topological number as

$$\frac{1}{4\pi}\int d^2\boldsymbol{r}\boldsymbol{n}^{sk} \cdot \left(\frac{\partial \boldsymbol{n}^{sk}}{\partial x} \times \frac{\partial \boldsymbol{n}^{sk}}{\partial y}\right) = -1. \tag{3.3.4}$$

For simplicity, we consider a specific skyrmion configuration given by

$$n_x^{sk}(\boldsymbol{r}) = -\sin\Theta(r)\frac{y}{r}, \tag{3.3.5}$$

$$n_y^{sk}(\boldsymbol{r}) = \sin\Theta(r)\frac{x}{r}. \tag{3.3.6}$$

$$n_z^{sk}(\boldsymbol{r}) = \cos\Theta(r), \tag{3.3.7}$$

where $\Theta(r)$ only depends on $r = \sqrt{x^2 + y^2}$, and it satisfied $\Theta(0) = \pi$ and $\Theta(\infty) = 0$. With this configuration and the torque (Eq. (3.3.3)), we calculate the time dependence of $\boldsymbol{R}(t)$

from the LLG equation (Eq. (3.3.1)), and obtain

$$\dot{R}_x = -\Lambda_0 j_x - \alpha_G \Lambda_1 j_y, \tag{3.3.8}$$
$$\dot{R}_y = -\Lambda_0 j_y + \alpha_G \Lambda_1 j_x, \tag{3.3.9}$$

where

$$\Lambda_0 = \frac{JMK^{(0)}}{\hbar^2}\frac{L_0}{4\pi}, \tag{3.3.10}$$
$$\Lambda_1 = \frac{JMK^{(0)}}{\hbar^2}\frac{\Gamma_0 L_0}{16\pi^2}. \tag{3.3.11}$$

L_0 and Γ_0 depends on the function $\Theta(r)$; $L_0 = \int d^2\boldsymbol{r}\partial_x \boldsymbol{n}_y = -\int d^2\boldsymbol{r}\partial_y \boldsymbol{n}_x$ is of the order of the radius of a skyrmion, and $\Gamma_0 = \int d^2\boldsymbol{r}\partial_x\boldsymbol{n}\cdot\partial_x\boldsymbol{n} = \int d^2\boldsymbol{r}\partial_y\boldsymbol{n}\cdot\partial_y\boldsymbol{n}$.

The supercurrent-induced torque can give rise to the drift motion of skyrmions, and the finite Gilbert damping coefficient α_G gives the transverse motion against the supercurrent, which is a well known effect for skyrmion dynamics[164]. Eqs. (3.3.8) and (3.3.9) are compatible with the results obtained from phenomenological arguments in the presence of SO coupling[172].

3.4 Weyl Bogoliubov quasiparticles

In the heterostructure of interest, Bogoliubov quasiparticles have nontrivial band topology; a pair of Weyl points exists. We first study the effective Hamiltonian which describes low-energy quasiparticles, and then numerically demonstrate the existence of type-I and type-II Weyl points. In the end of this section, we discuss the effect of the spatial inhomogeneity in spin textures and show that an effective magnetic field acts on the quasiparticles.

3.4.1 Type-I and Type-II Weyl fermions

The strucutre of Bogoliubov quasiparticles in the presence of spin texutres such as skyrmions is rather complicated. Before tackling this problem, we first consider the case of a homegenous exchange field. This analysis is valid provided that the spatial variation of the spin texture is sufficiently weak compared to the Fermi wave-length and the superconducting coherence length, and thus the spin configuration is locally approximated by a homogeneous structure.

For a homogeneous spin configuration, the effective Hamitonian is derived in Sec. 3.6.1. In the limit of $\{JM, |\mu|\} \gg \{t, \alpha_{so}, \Delta\}$ with $\mu \sim -JM$, the Hamiltonian for low-energy quasiparticles is given by

$$H_{\text{eff}}(\boldsymbol{k}) = \alpha_{so}\boldsymbol{k}\cdot\boldsymbol{n}\mathbf{1} + \begin{pmatrix} \xi_{\text{eff}}(\boldsymbol{k}) & \Delta_{\text{eff}}\boldsymbol{\gamma}\cdot\boldsymbol{k} \\ \Delta_{\text{eff}}\boldsymbol{\gamma}^*\cdot\boldsymbol{k} & -\xi_{\text{eff}}(\boldsymbol{k}) \end{pmatrix} \tag{3.4.1}$$

where

$$\Delta_{\text{eff}} = \frac{|\Delta|\alpha_{so}(JM + |\mu|)}{2JM|\mu|}, \tag{3.4.2}$$

$$\xi_{\text{eff}}(\boldsymbol{k}) = \varepsilon_{\boldsymbol{k}} - JM - \mu - \frac{|\Delta|^2}{2\mu} + \frac{\alpha_{so}^2}{2JM} k_\perp^2. \tag{3.4.3}$$

Here we consider the momentum $|\boldsymbol{k}|a \ll 1$ (a=1), and define $k_\perp^2 = k^2 - (\boldsymbol{k} \cdot \boldsymbol{n})^2$. A complex vector $\boldsymbol{\gamma} = (\gamma_x, \gamma_y, \gamma_z)$ satisfies $|Re\boldsymbol{\gamma}| = |Im\boldsymbol{\gamma}| = 1$ and $Re\boldsymbol{\gamma} \times Im\boldsymbol{\gamma} = -\boldsymbol{n}$. (See Sec. 3.6 for detail) The two bands cross at $\boldsymbol{k} = \pm k_0\boldsymbol{n}$ if there exists k_0 that satisfies $\xi_{\text{eff}}(k_0\boldsymbol{n}) = 0$, and the crossing points are shifted from the zero energy by $\pm\alpha_{so}k_0$. These crossing points are protected by the spin rotation symmetry along $\boldsymbol{n}$, i.e., two crossing bands of interest have different eigenvalues of $\hat{\boldsymbol{S}} \cdot \boldsymbol{n}$, which commutes with $H(k_0\boldsymbol{n})$.

Without loss of generality, we can define x, y and z axis of momentum along $Re\boldsymbol{\gamma}, Im\boldsymbol{\gamma}$, and $\boldsymbol{n}$ so that the crossing points locates at $k_0\hat{\boldsymbol{z}}$. The effective Hamiltonian around the crossing points reads

$$H_{\text{eff}}(\pm k_0\hat{\boldsymbol{z}} + \boldsymbol{q}) = \alpha_{so}(\pm k_0 + q_z)\mathbf{1} + \begin{pmatrix} \pm t k_0 q_z & \Delta_{\text{eff}}(q_x + iq_y) \\ \Delta_{\text{eff}}(q_x - iq_y) & \mp t k_0 q_z \end{pmatrix}. \tag{3.4.4}$$

Each cone is tilted by $\alpha_{so}q_z$, and numerical calculations of the Berry curvature with the original BdG Hamiltonian (Eq. (3.2.1)) show that they are a pair of Weyl points, which are a source and a sink of the Berry curvature. The numerical result of the phase diagram is summarized in Fig. 3.4. When the chemical potential is larger than the critical value, a pair of Weyl points with the opposite topological charge exists. In Fig. 3.5 (a) and (b), a band structure for the parameter $\mu = -4.8$, and $\alpha_{so} = 0.6$ is shown, which has conventional (type-I) Weyl cones. The dispersions are weakly tilted in k_z direction.

Interestingly, changing α_{so} or μ leads to a transition between type-I and type-II Weyl cones. Type-II Weyl cones are characterized by the finite density of states at the crossing energy due to the tilt of the cones. The energy spectrum is shown in Fig. 3.5 (c) and (d) for $\mu = -4.8$ and $\alpha_{so} = 0.6$. This tilt may induce distinct properties in transport or the Landau levels under an effective magnetic field discussed in the next section.

We have obtained the surface Majorana arc exists for both type-I and type-II Weyl points by numerical calculations with an open boundary. Since the positions of the Weyl points is at $\pm k_0\boldsymbol{n}$, the surface in which the Majorana arc appear can be changed by the direction of the magnetization.

In the $k_z = 0,\ \pm\pi$ plane, our system can be mapped to a well-known model. By rotating the momentum by $90°$ along k_z axis, the Hamiltonian (Eq. (3.2.1)) is equivalent to a model to realize a spinless $p + ip$ superconductor with the Rashba SO coupling[51, 176]. These two-dimensional planes can have nonzero Chern number depending on the parameters, and the difference of the Chern number ensures the existence of Weyl points.

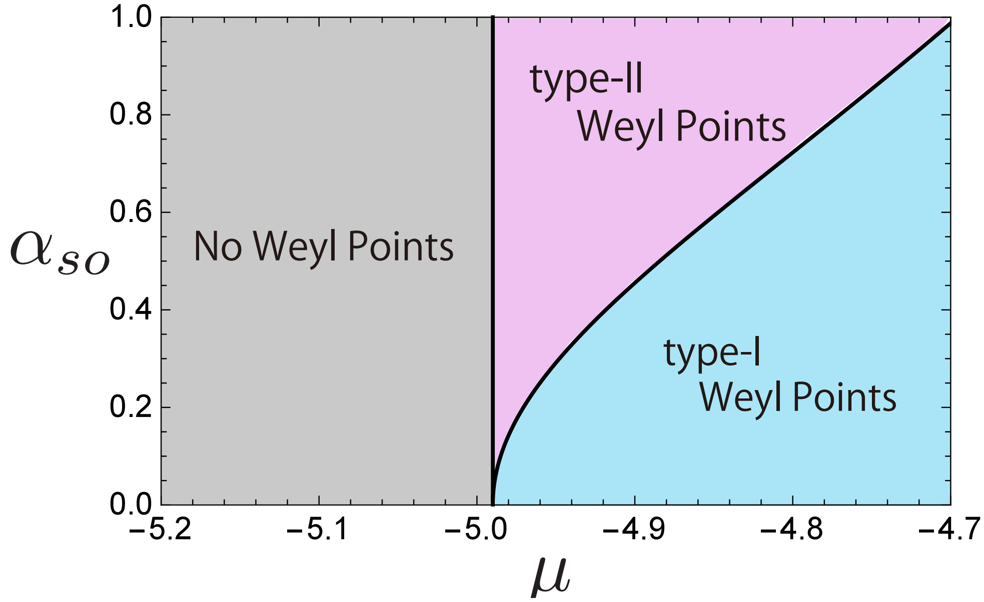

Figure 3.4: Phase diagram of Weyl points as a function of chemical potential μ and the SO coupling coefficient α_{so} with the parameter $t = 1.0,\ JM = 2.0,\ \Delta = 0.2$. In phases denoted by type-I (type-II) Weyl points, a pair of type-I (type-II) Weyl points exist.

3.4.2 Inhomogeneous spin texture

So far, we have studied a locally homogeneous system assuming that the spin texture varies weakly enough in space. Now we include the effect of inhomogeneity to the lowest order and show the emergence of an effective magnetic field. We consider quasiparticle states around some arbitary point $\boldsymbol{r}_0$ in real space, and define $\boldsymbol{n}_0 = \boldsymbol{n}(\boldsymbol{r}_0)$ and $\boldsymbol{\gamma}_0 = \boldsymbol{\gamma}(\boldsymbol{r}_0)$. We then rewrite as $\boldsymbol{n}(\boldsymbol{r}) = \boldsymbol{n}_0 + \delta\boldsymbol{n}(\boldsymbol{r})$ and $\gamma(\boldsymbol{r}) = \gamma_0 + \delta\gamma(\boldsymbol{r})$. Around one of the Weyl point given by $\boldsymbol{k} = k_0\boldsymbol{n}_0$, we define the Bogoliubov quasiparticle operator as $\psi(\boldsymbol{r}) = e^{ik_0\boldsymbol{n}_0\cdot\boldsymbol{r}}\tilde{\psi}_+(\boldsymbol{r})$. Up to the lowest order of spatial variation, the Hamiltonian for slowly varying field is given by

$$H^+_{\text{eff}}(\boldsymbol{r}) = \alpha_{so}(k_0 + \boldsymbol{n}_0\cdot\hat{\boldsymbol{p}})\mathbf{1} + \begin{pmatrix} tk_0\boldsymbol{n}_0\cdot\hat{\boldsymbol{p}} & \Delta_{\text{eff}}\boldsymbol{\gamma}_0\cdot(\hat{\boldsymbol{p}} - k_0\boldsymbol{n}(\boldsymbol{r})) \\ \Delta_{\text{eff}}\boldsymbol{\gamma}_0^*\cdot(\hat{\boldsymbol{p}} - k_0\boldsymbol{n}(\boldsymbol{r})) & -tk_0\boldsymbol{n}_0\cdot\hat{\boldsymbol{p}} \end{pmatrix}, \tag{3.4.5}$$

$$= \alpha_{so}(k_0 + \boldsymbol{n}_0\cdot(\hat{\boldsymbol{p}} - k_0\delta\boldsymbol{n}(\boldsymbol{r}))\mathbf{1} + \begin{pmatrix} tk_0\boldsymbol{n}_0\cdot(\hat{\boldsymbol{p}} - k_0\delta\boldsymbol{n}(\boldsymbol{r})) & \Delta_{\text{eff}}\boldsymbol{\gamma}_0\cdot(\hat{\boldsymbol{p}} - k_0\delta\boldsymbol{n}(\boldsymbol{r})) \\ \Delta_{\text{eff}}\boldsymbol{\gamma}_0^*\cdot(\hat{\boldsymbol{p}} - k_0\delta\boldsymbol{n}(\boldsymbol{r})) & -tk_0\boldsymbol{n}_0\cdot(\hat{\boldsymbol{p}} - k_0\delta\boldsymbol{n}(\boldsymbol{r})) \end{pmatrix}, \tag{3.4.6}$$

where we have used the relation $\boldsymbol{n}(\boldsymbol{r})\cdot\boldsymbol{\gamma}(\boldsymbol{r}) = 0$ and $\boldsymbol{n}_0\cdot\delta\boldsymbol{n}(\boldsymbol{r}) = 0$. Minimal coupling $\hat{\boldsymbol{p}} - k_0\delta\boldsymbol{n}(\boldsymbol{r})$ exhibits that the effect of the spatial variation of spins can be described by the effective magnetic field given by $\boldsymbol{B}_{\text{eff}}(\boldsymbol{r}) = k_0\boldsymbol{\nabla}\times\boldsymbol{n}(\boldsymbol{r})$. Around the other Weyl point at $-k_0\boldsymbol{n}_0$, the sign is the opposite: $\boldsymbol{B}_{\text{eff}}(\boldsymbol{r}) = -k_0\boldsymbol{\nabla}\times\boldsymbol{n}(\boldsymbol{r})$.

This result shows that Bogoliubov quasiparticles around each Weyl cone may form the Landau levels when $\boldsymbol{\nabla} \times \boldsymbol{n}(\boldsymbol{r}) \neq \boldsymbol{0}$, and the chiral zero modes are expected to appear for each cone, which is studied in the A phase of ^{3}He [177, 178, 179]. The velocities of the chiral zero modes have the same direction for two cones to preserve the particle hole symmetry, and they are along the direction of $\boldsymbol{\nabla} \times \boldsymbol{n}(\boldsymbol{r})$.

A skyrmion texture gives $\boldsymbol{\nabla} \times \boldsymbol{n}(\boldsymbol{r}) \neq \boldsymbol{0}$, and a skyrmion flow is expected to cause an effective electric field given by $\mp k_0 \partial_t \boldsymbol{n}$, which acts on quasiparticles in each cone. As has been discussed in ^{3}He [178, 179], the quasiparticle excitation in the chiral zero mode is expected to cause a force acting on the skyrmion, which is in perpendicular to the velocity of the skyrmion [2], i.e., the anomaly of Weyl fermions can affect the skyrmion dynamics.

Tuning the tilt may change the property of the chiral zero modes, as is studied in Weyl semimetal[154]. We leave the detailed study of skyrmion dynamics associated with Weyl fermions in chiral magnet for future work.

[2]This is distinguished from the Magnus force, which does not require the excitation of quasiparticles.

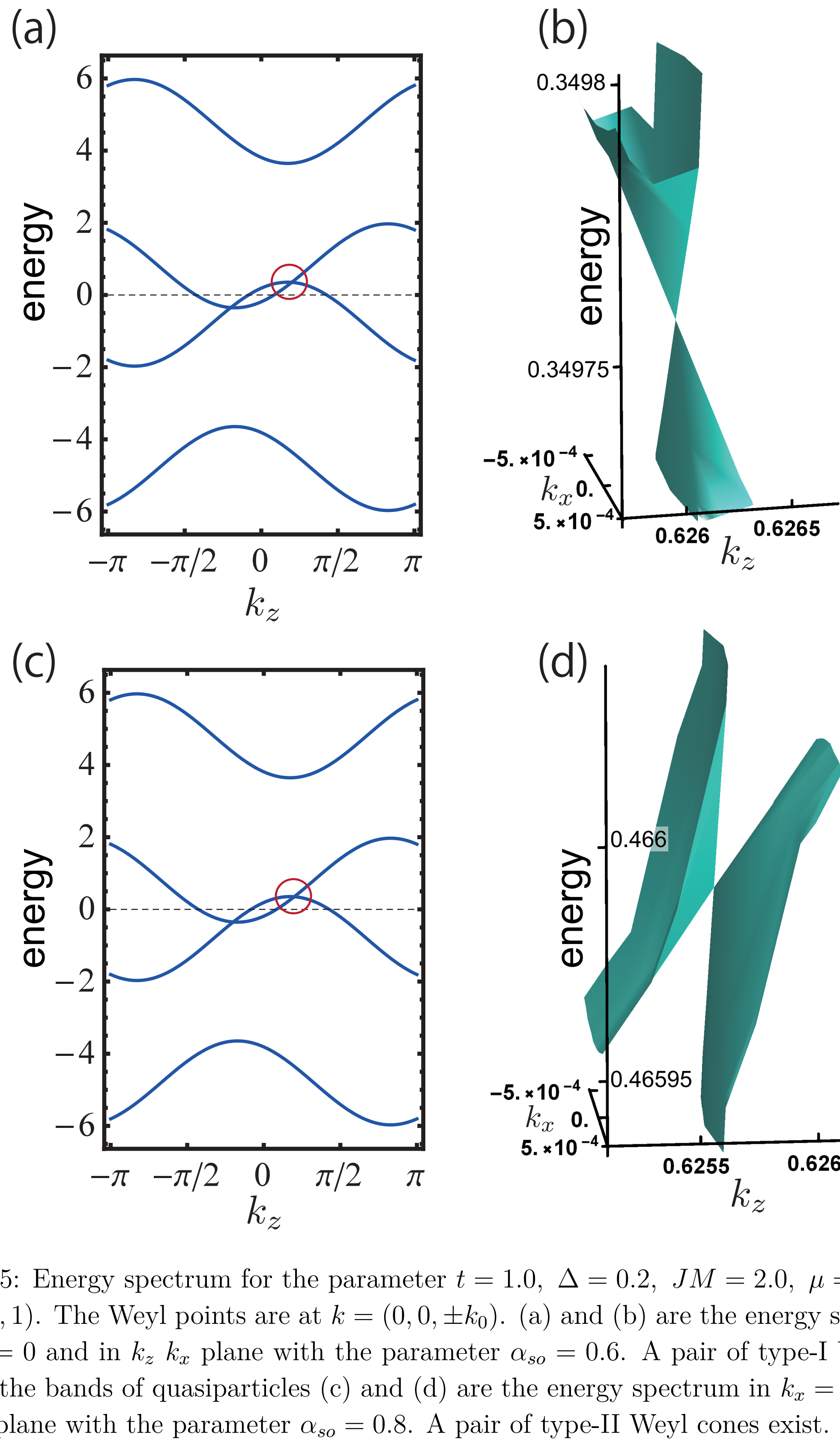

Figure 3.5: Energy spectrum for the parameter $t = 1.0,\ \Delta = 0.2,\ JM = 2.0,\ \mu = -4.8$ and $\boldsymbol{n} = (0, 0, 1)$. The Weyl points are at $k = (0, 0, \pm k_0)$. (a) and (b) are the energy spectrum in $k_x = k_y = 0$ and in k_z k_x plane with the parameter $\alpha_{so} = 0.6$. A pair of type-I Weyl cones exists in the bands of quasiparticles (c) and (d) are the energy spectrum in $k_x = k_y = 0$ and in k_z k_x plane with the parameter $\alpha_{so} = 0.8$. A pair of type-II Weyl cones exist.

3.5 Summary and discussion

In this chapter, we have studied a spin-torque induced by a supercurrent in a heterostructure composed of a cubic chiral magnet and an s-wave superconductor. With the numerical and analytical calculation, we have derived the spin polarization induced by a supercurrent, which depends on the direction of the localized spin. The equation for the time evolution of skyrmion has been obtained.

We have also pointed out the existence of a pair of Weyl points in the quasiparticle bands. The positions of the Weyl points are determined by the magnetization, and the resulting effective electromagnetic field may give rise to novel phenomena in spintronics. The tilt of the cones can also be changed by the strength of the SO coupling, and type-II Weyl points can be realized. We believe that nontrivial band topology of Bogoliubov quasiparticles provides a new perspective in superconducting spintronics.

We leave the discussion on the stability of the proximity induced superconducting gap for future work. The quantitative estimation requires self-consistent calculations of the superconducting gap. At this point, we expect that there should be a finite region where the superconducting gap is proximity-induced in the chiral magnet when the interface between the superconductor and the chiral magnet is sufficiently smooth.

3.6 Details

In this section, we present the derivation and more detailed discussion on this chapter.

3.6.1 Derivation of Eq. (3.2.7)

A supercurrent gives the finite phase gradient of superconducting order parameter as

$$\frac{1}{2}\sum_i (\Delta e^{2i\boldsymbol{\kappa}\cdot\boldsymbol{r}_i} c^\dagger_{i\uparrow} c^\dagger_{i\downarrow} + \text{H.c.}). \tag{3.6.1}$$

To simplify the calculation, we introduce fermion operators $\tilde{c}_{i\sigma} = c_{i\sigma} e^{-i\boldsymbol{\kappa}\cdot\boldsymbol{r}_i}$ and $\tilde{c}^\dagger_{i\sigma} = c^\dagger_{i\sigma} e^{i\boldsymbol{\kappa}\cdot\boldsymbol{r}_i}$. With these operators, the Hamiltonian can be rewritten as

$$H = \frac{1}{2}\sum_{\boldsymbol{k}} \tilde{\Psi}^\dagger_{\boldsymbol{k}} \tilde{H}(\boldsymbol{k}) \tilde{\Psi}_{\boldsymbol{k}}, \tag{3.6.2}$$

$$\tilde{H}(\boldsymbol{k}) = \begin{pmatrix} H_N(\boldsymbol{k}+\boldsymbol{\kappa}) & \Delta(i\sigma_y) \\ \Delta^*(i\sigma_y)^\dagger & -H_N(-\boldsymbol{k}+\boldsymbol{\kappa})^{\mathrm{T}} \end{pmatrix}, \tag{3.6.3}$$

$$= H(\boldsymbol{k}) + \hat{V}_\nu \kappa_\nu + O(\kappa^2), \tag{3.6.4}$$

where we define $\tilde{\Psi}_{\boldsymbol{k}} = (\tilde{c}_{\boldsymbol{k},\uparrow}, \tilde{c}_{\boldsymbol{k},\downarrow}, \tilde{c}^{\dagger}_{-\boldsymbol{k},\uparrow}, \tilde{c}^{\dagger}_{-\boldsymbol{k},\downarrow},)^{\mathrm{T}} = (c_{\boldsymbol{k}+\boldsymbol{\kappa},\uparrow}, c_{\boldsymbol{k}+\boldsymbol{\kappa},\downarrow}, c^{\dagger}_{-\boldsymbol{k}+\boldsymbol{\kappa},\uparrow}, c^{\dagger}_{-\boldsymbol{k}+\boldsymbol{\kappa},\downarrow})^{\mathrm{T}}$. The spin-polarization density can be represented with $\tilde{c}_{\boldsymbol{k}}$ as

$$s_\mu = \frac{\hbar}{2V}\sum_{\boldsymbol{k}} \langle c^{\dagger}_{\boldsymbol{k}} \sigma_\mu c_{\boldsymbol{k}} \rangle, \tag{3.6.5}$$

$$= \frac{\hbar}{2V}\sum_{\boldsymbol{k}} \langle \tilde{c}^{\dagger}_{\boldsymbol{k}} \sigma_\mu \tilde{c}_{\boldsymbol{k}} \rangle. \tag{3.6.6}$$

A perturbation theory with $\tilde{H}(\boldsymbol{k})$ leads to Eq. (3.2.7).

3.6.2 Derivation of $H_{\text{eff}}(\boldsymbol{k})$

We show the derivation of the effective Hamiltonian when $\{JM, |\mu|\} \gg \{t, \alpha_{so}, \Delta\}$. We start from the BdG Hamiltonian in Eq. (3.2.1). Then we apply a unitary transformation $U^{\dagger}(\boldsymbol{k})H(\boldsymbol{k})U(\boldsymbol{k})$. The unitary matrix is given by

$$U(\boldsymbol{k}) = \begin{pmatrix} U_0 & 0 \\ 0 & U_0^* \end{pmatrix} e^{iQ(\boldsymbol{k})}, \tag{3.6.7}$$

where U_0 rotates the spin axis as $U_0^{\dagger}\boldsymbol{n}\cdot\boldsymbol{\sigma}U_0 = \sigma_z$.

$Q(\boldsymbol{k})$ is Hermite matrix given by

$$Q(\boldsymbol{k}) = \begin{pmatrix} 0 & -\frac{i\alpha_{so}}{2M}\omega & 0 & -\frac{i\Delta}{2\mu} \\ \frac{i\alpha_{so}}{2M}\omega^* & 0 & \frac{i\Delta}{2\mu} & 0 \\ 0 & -\frac{i\Delta^*}{2\mu} & 0 & \frac{i\alpha_{so}}{2M}\omega^* \\ \frac{i\Delta^*}{2\mu} & 0 & \frac{-i\alpha_{so}}{2M}\omega & 0 \end{pmatrix} \tag{3.6.8}$$

with

$$\omega = \sum_{\ell=x,y,z} \sin(k_\ell a)\left(U_0^{\dagger}\sigma_\ell U_0\right)_{12}. \tag{3.6.9}$$

Then we expand the Hamiltonian in the series of ϵ where we define the small parameter by $\{t, \alpha_{so}, \Delta\} \sim \epsilon JM$, as $U^{\dagger}(\boldsymbol{k})H(\boldsymbol{k})U(\boldsymbol{k}) = H_0'(\boldsymbol{k}) + H_1'(\boldsymbol{k}) + \mathcal{O}(\epsilon^3)$, where $H_0'(\boldsymbol{k})$ is given by Eq. (3.2.11) and

$$H_1'(\boldsymbol{k}) = \begin{pmatrix} -\frac{|\Delta|^2}{2\mu} - \frac{\alpha_{so}^2}{2JM}|\omega|^2 & \frac{\alpha_{so}^2}{JM}\beta\omega & u_0\Delta\omega & \frac{\Delta}{\mu}(\varepsilon_{\boldsymbol{k}} + \alpha_{so}\beta) \\ \frac{\alpha_{so}^2}{JM}\beta\omega^* & -\frac{|\Delta|^2}{2\mu} + \frac{\alpha_{so}^2}{2JM}|\omega|^2 & -\frac{\Delta}{\mu}(\varepsilon_{\boldsymbol{k}} - \alpha_{so}\beta) & u_1\Delta\omega^* \\ u_0\Delta^*\omega^* & -\frac{\Delta^*}{\mu}(\varepsilon_{\boldsymbol{k}} - \alpha_{so}\beta) & \frac{|\Delta|^2}{2\mu} + \frac{\alpha_{so}^2}{2JM}|\omega|^2 & -\frac{\alpha_{so}^2}{JM}\beta\omega^* \\ \frac{\Delta^*}{\mu}(\varepsilon_{\boldsymbol{k}} + \alpha_{so}\beta) & u_1\Delta^*\omega & -\frac{\alpha_{so}^2}{JM}\beta\omega & \frac{|\Delta|^2}{2\mu} - \frac{\alpha_{so}^2}{2JM}|\omega|^2 \end{pmatrix}, \tag{3.6.10}$$

with $\beta = \sum_{\ell=x,y,z}\sin(k_\ell a)n_\ell$, $u_0 = -\frac{\alpha_{so}(JM-\mu)}{2JM\mu}$, and $u_1 = \frac{\alpha_{so}(JM+\mu)}{2JM\mu}$. When $\mu \sim -JM$, the eigenstates of $H_0'(\boldsymbol{k})$ are energetically separated as $E_{3\boldsymbol{k}} \ll \{E_{0\boldsymbol{k}} \sim E_{2\boldsymbol{k}} \sim 0\} \ll E_{1\boldsymbol{k}}$. We project the Hilbert space to a space around zero energy, i.e. a space spanned by eigenstates with eigenenergy $E_{0\boldsymbol{k}}$ and $E_{2\boldsymbol{k}}$.

The effective Hamiltonian $H_{\text{eff}}(\boldsymbol{k})$ is given by

$$H_{\text{eff}}(\boldsymbol{k}) = \begin{pmatrix} (H_0'(\boldsymbol{k}))_{11} + (H_1'(\boldsymbol{k}))_{11} & (H_0'(\boldsymbol{k}))_{13} + (H_1'(\boldsymbol{k}))_{13} \\ (H_0'(\boldsymbol{k}))_{31} + (H_1'(\boldsymbol{k}))_{31} & (H_0'(\boldsymbol{k}))_{33} + (H_1'(\boldsymbol{k}))_{33} \end{pmatrix}, \tag{3.6.11}$$

$$= \begin{pmatrix} E_{0\boldsymbol{k}} - \frac{|\Delta|^2}{2\mu} - \frac{\alpha_{so}^2}{2JM}|\omega|^2 & -\frac{\alpha_{so}|\Delta|(JM-\mu)}{2JM\mu}e^{i\varphi}\omega \\ -\frac{\alpha_{so}|\Delta|(JM-\mu)}{2JM\mu}e^{-i\varphi}\omega^* & E_{2\boldsymbol{k}} + \frac{|\Delta|^2}{2\mu} + \frac{\alpha_{so}^2}{2JM}|\omega|^2 \end{pmatrix}, \tag{3.6.12}$$

where we define $\Delta = |\Delta|e^{i\varphi}$ and $(H_n'(\boldsymbol{k}))_{ij}$ is the (i,j) component of $H_n'(\boldsymbol{k})$. We introduce a complex vector $\boldsymbol{\gamma} = (\gamma_x, \gamma_y, \gamma_z)$ as

$$\boldsymbol{\gamma} = e^{i\varphi}\left(U_0^\dagger \boldsymbol{\sigma} U_0\right)_{12}, \tag{3.6.13}$$

where $\left(U_0^\dagger \boldsymbol{\sigma} U_0\right)_{12}$ is the $(1,2)$ component in the 2×2 matrix $U_0^\dagger \boldsymbol{\sigma} U_0$. One can show the following relations

$$|Re\boldsymbol{\gamma}| = |Im\boldsymbol{\gamma}| = 1, \tag{3.6.14}$$

$$Re\boldsymbol{\gamma}\cdot Im\boldsymbol{\gamma} = 0, \tag{3.6.15}$$

$$Re\boldsymbol{\gamma}\times Im\boldsymbol{\gamma} = -\boldsymbol{n}, \tag{3.6.16}$$

$$\epsilon_{\mu\nu\lambda}\partial_\mu(\boldsymbol{\gamma}^*\cdot\partial_\nu\boldsymbol{\gamma}) = -2i\epsilon_{\mu\nu\lambda}\boldsymbol{n}\cdot(\partial_\mu\boldsymbol{n}\times\partial_\nu\boldsymbol{n}). \tag{3.6.17}$$

The last equation shows that the rotation of the superfluid velocity is given by the skyrmion density. Around the Γ point ($|\boldsymbol{k}|a \ll 1$), we obtain the effective Hamiltonian in Eq. (3.4.1), noting that $e^{i\varphi}\omega = \boldsymbol{\gamma}\cdot\boldsymbol{k}a$ and $|\omega|^2 = a^2k^2 - a^2(\boldsymbol{k}\cdot\boldsymbol{n})^2$.

3.6.3 Derivation of Eq. (3.2.16)

In this section, we calculate the matrix element $\mathcal{S}_{\mu\nu}$ (Eq. (3.2.16)) with the effective Hamiltonian in the continuum limit ($|\boldsymbol{k}|a \ll 1$). The effective Hamiltonian (Eq. (3.4.1)) is

$$H_{\text{eff}}(\boldsymbol{k}) = f_0\mathbf{1} + \boldsymbol{f}\cdot\boldsymbol{\tau}, \tag{3.6.18}$$

with $\boldsymbol{\tau} = (\tau_x, \tau_y, \tau_z)$ are pauli matrices, and

$$f_0 = \alpha_{so}\boldsymbol{k}\cdot\boldsymbol{n}, \tag{3.6.19}$$

$$\boldsymbol{f} = (f_1, f_2, f_3), \tag{3.6.20}$$

$$f_1 = \Delta_{\text{eff}}\text{Re}\boldsymbol{\gamma}\cdot\boldsymbol{k}, \tag{3.6.21}$$

$$f_2 = -\Delta_{\text{eff}}\text{Im}\boldsymbol{\gamma}\cdot\boldsymbol{k}, \tag{3.6.22}$$

$$f_3 = \xi_{\text{eff}}(\boldsymbol{k}). \tag{3.6.23}$$

We define $\boldsymbol{f}/|\boldsymbol{f}| = (\sin\theta_0\cos\phi_0, \sin\theta_0\sin\phi_0, \cos\theta_0)$, and then the eigenstates of Eq. (3.4.1) are given by

$$||+,\boldsymbol{k}\rangle = \begin{pmatrix} \cos\frac{\theta_0}{2}e^{-i\phi_0} \\ \sin\frac{\theta_0}{2} \end{pmatrix}, \tag{3.6.24}$$

$$||-,\boldsymbol{k}\rangle = \begin{pmatrix} \sin\frac{\theta_0}{2}e^{-i\phi_0} \\ -\cos\frac{\theta_0}{2} \end{pmatrix}. \tag{3.6.25}$$

The corresponding eigenstates are $\varepsilon_{\pm,\boldsymbol{k}} = f_0 \pm |\boldsymbol{f}|$, which depend on k^2 and $\boldsymbol{k}\cdot\boldsymbol{n}$. The spin and velocity operators in the projected space are

$$\hat{S}^{\text{eff}}_\mu \sim \frac{\hbar}{2}\left(n_\mu\tau_z - \frac{\alpha_{so}}{M}\text{Re}(\gamma^*_\mu\boldsymbol{\gamma}\cdot\boldsymbol{k})\mathbf{1}\right), \tag{3.6.26}$$

$$\hat{V}^{\text{eff}}_\mu \sim -tk_\mu\mathbf{1} + \alpha_{so}n_\mu\tau_z, \tag{3.6.27}$$

where we have expanded in the series of ϵ. Thus we obtain

$$\begin{aligned} \mathcal{S}_{\mu\nu} &= \langle -,\boldsymbol{k}||\hat{S}^{\text{eff}}_\mu||+,\boldsymbol{k}\rangle\langle +,\boldsymbol{k}||\hat{V}^{\text{eff}}_\nu||-,\boldsymbol{k}\rangle, && (3.6.28)\\ &= \langle -,\boldsymbol{k}||\tau_z||+,\boldsymbol{k}\rangle\langle +,\boldsymbol{k}||\tau_z||-,\boldsymbol{k}\rangle\frac{\hbar}{2}\alpha_{so}n_\mu n_\nu, && (3.6.29)\\ &= \sin^2\theta_0\frac{\hbar}{2}\alpha_{so}n_\mu n_\nu, && (3.6.30)\\ &= \frac{\Delta^2_{\text{eff}}k^2_\perp}{\xi_{\text{eff}}(\boldsymbol{k})^2 + \Delta^2_{\text{eff}}k^2_\perp}\frac{\hbar}{2}\alpha_{so}n_\mu n_\nu, && (3.6.31) \end{aligned}$$

where $k^2_\perp = k^2 - (\boldsymbol{k}\cdot\boldsymbol{n})^2$. One can also show that $\langle +,\boldsymbol{k}||S^{\text{eff}}_\mu||-,\boldsymbol{k}\rangle\langle -,\boldsymbol{k}||V^{\text{eff}}_\nu||+,\boldsymbol{k}\rangle = \mathcal{S}_{\mu\nu}$.

Chapter 4

Generating noncollinear magnetism by supercurrent

When superconductivity couples with noncollinear spin textures, rich physics arises; for instance, singlet Cooper pairs can be converted to triplet pairs, and topological superconductors can be realized. For their application, generating and controlling noncollinear magnetism are crucial issues. In this chapter, we consider a metallic layer on top of a singlet superconductor with a supercurrent flow. We demonstrate that a supercurrent induces noncollinear magnetic orders, such as helical (single-Q) and vortexlike (double-Q) orders in a controlled manner. Furthermore, these states can be switched by the direction of the supercurrent. Our results open up the possibilities to use superconducting correlations as a “harness” for spin textures.

The organization of this chapter is as follows. In Sec. 4.1, we first show the background and the aim of this chapter. In Sec. 4.2, we present the model, a two-dimensional correlated metal deposited on a singlet superconductor with a supercurrent flow. In Sec. 4.3, we calculate the spin susceptibility in the correlated metal, and show that the magnetic instability is enhanced by the proximity effect of supercurrents. In Sec. 4.4, we show that the instability actually leads to magnetic ordering by presenting the magnetic phase diagrams. In Sec. 4.5, we provide the summary and discussion of this work. Finally, Sec. 4.6 provides the details of the calculation.

4.1 Introduction to this chapter

The proximity effect of superconductivity, inducing Cooper pairs in non-superconducting materials, has renewed interest for application ranging from spintronics devices to topological quantum computation. As we have already discussed in Chap. 2, in spintronics, spin-triplet Cooper pairs are promising spin carriers for efficient spintronics devices with suppressed Joule heating [107, 108]. The interplay between triplet pairs and magnetic moments show rich physics such as a novel type of domain wall dynamics [1, 180, 122, 181]. Furthermore, an artificially engineered system with proximity-induced superconductivity is one of the most promising platforms for realizing topological superconductors [182, 176, 47, 48, 49]. They can host Majorana fermions, whose non-Abelian statistics might be used for topological quantum computing [38].

In these application of superconductivity, noncollinear magnetic orders play essential roles. Here we present two examples: (1) spin conversion of Cooper pairs and (2) engineering topological superconductivity.

(1) Triplet Cooper pairs can be generated from a singlet superconductor via the coupling to noncollinear magnetic moments: noncollinearity of magnetic moments breaks the spin rotational symmetry of electrons and can convert singlet Cooper pairs to triplet pairs [18]. This "spin-conversion" of Cooper pairs is experimentally observed [23, 24]. Robinson *et al.* [24] studied junctions Nb/Ho/Co/Ho/Nb, where Nb becomes an s-wave superconductor ($T_c \sim 9.2$K), Ho is a conical magnet, and Co is a ferromagnet. They observed the characteristic voltage of the junction for different Co thicknesses. Notably, the characteristic voltage decays much slower as the function of the Co thickness in the junction with Ho compared to the one without Ho. This shows that the long-range proximity effect inside the ferromagnet is realized, and it is attributed to the spin-triplet pairing induced by noncollinear moments in Ho.

(2) One can engineer topological superconductor by using noncollinear magnetic moments. 1D spinless p-wave superconductivity can be realized using a helical spin texture on an s-wave superconducting substrate [42, 43, 44, 45, 46]. Klinovaja *et al.* [44] have shown that a helical order realized by RKKY interaction realizes a topological superconductor and it does not need to tune the chemical potential. Furthermore, two-dimensional $p + ip$-wave superconductivity can be realized using a magnetic skyrmion texture [52, 53, 54]. Nakosai *et al.* [52] numerically calculate the quasiparticle spectrum in a system with a SkX and an s-wave paring potential and found the chiral edge modes. These schemes do not require the strong relativistic spin-orbit coupling, and hence expand the range of candidate materials.

Given the interplay between noncollinear spin textures and superconductivity, controlling noncollinear magnetism is crucial to externally control the resulting physics. For example, we could turn on or optimize singlet-triplet conversion, and it might also be possible to manipulate Majorana zero modes by magnetic states. In normal states, several ways are known to induce or switch magnetic orders, e.g., applying an electric field [183, 184] or optical pulses [185, 186]. However, in the presence of superconductivity, little is known about the tunability of magnetic orders [1]. Therefore, the aim of this chapter is to propose a way to generate and control noncollinear magnetic order by utilizing a supercurrent, in a correlated metal in proximity to a singlet superconductor.

4.2 Model

We consider a two-dimensional model of a correlated metal deposited on a bulk singlet superconductor with a supercurrent flow. A possible experimental setup is shown in Fig. 4.1. This can be described by the Hamiltonian $H = H_0 + H_U$, where we define

$$H_0 = \sum_{\boldsymbol{k}\sigma} \xi_{\boldsymbol{k}} c^\dagger_{\boldsymbol{k}\sigma} c_{\boldsymbol{k}\sigma} + \sum_{ij} (\Delta_{ij} e^{i\boldsymbol{\kappa}\cdot(\boldsymbol{r}_i+\boldsymbol{r}_j)} c^\dagger_{i\uparrow} c^\dagger_{j\downarrow} + \text{H.c.}), \tag{4.2.1}$$

$$H_U = U \sum_i n_{i\uparrow} n_{i\downarrow}. \tag{4.2.2}$$

Here $c^\dagger_{i\sigma}(c_{i\sigma})$ is a creation (annihilation) operator of itinerant electrons at site $\boldsymbol{r}_i = (x_i, y_i)$ and spin σ, $c^\dagger_{\boldsymbol{k}\sigma}(c_{\boldsymbol{k}\sigma})$ is the Fourier transform of $c^\dagger_{i\sigma}(c_{i\sigma})$, and $\xi_{\boldsymbol{k}}$ is the energy dispersion measured from the chemical potential. The itinerant electrons have the repulsive Hubbard interaction with the strength $U > 0$, and $n_{i\sigma} = c^\dagger_{i\sigma} c_{i\sigma}$ is the electron density operator of spin σ. The proximity effect to the superconductor is taken into account by Δ_{ij} and $\boldsymbol{\kappa}$; Δ_{ij} describes a singlet pairing potential between sites i and j, and $\boldsymbol{\kappa}$, a spatial gradient of the superconducting phase, originates from a supercurrent flow. The supercurrent is assumed to be a unidirectional flow, and the supercurrent density $\mathbf{j}^{\text{sc}}$ is proportional to $\boldsymbol{\kappa}$ for $\xi|\boldsymbol{\kappa}| \ll 1$, where ξ is the coherence length of the bulk superconductor. In the following, we study this model within the mean-field approximation as $H \approx H_0 + H_U^{\text{MF}}$, where

$$H_U^{\text{MF}} = -\frac{4U}{3} \sum_i \mathbf{m}_i \cdot \mathbf{s}_i + \frac{2U}{3} \sum_i |\mathbf{m}_i|^2. \tag{4.2.3}$$

Here $\mathbf{s}_i = \frac{1}{2} \sum_{\sigma_1,\sigma_2} c^\dagger_{i\sigma_1} \boldsymbol{\sigma}_{\sigma_1\sigma_2} c_{i\sigma_2}$ is the spin density operator at site i with the Pauli matrices $\boldsymbol{\sigma} = (\sigma^x, \sigma^y, \sigma^z)$, and $\mathbf{m}_i = \langle \mathbf{s}_i \rangle$ is the mean field of the spin density.

[1] In superconductors coexisting with magnetic moments, it is proposed that a supercurrent changes the direction of the spin texture [187, 188].

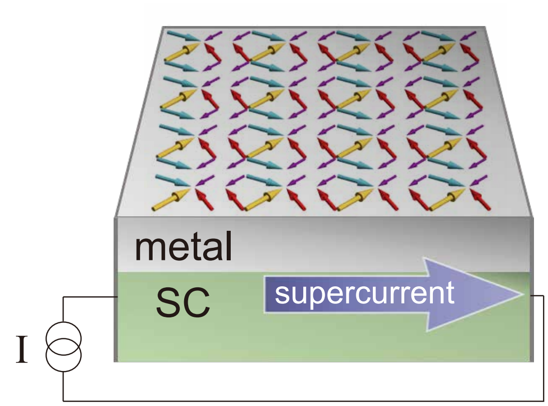

Figure 4.1: The proposed setup for an experimental realization. A metallic layer is deposited on a bulk singlet superconductor (SC), where a supercurrent is supplied from a current battery.

4.3 Magnetic instability

Let us first demonstrate that a supercurrent $\mathbf{j}^{\mathrm{sc}} \propto \boldsymbol{\kappa}$ enhances an instability toward a non-collinear magnetic order. From now on, we will focus on an s-wave pairing ($\Delta_{ij} = \frac{1}{2}\Delta\delta_{ij}$) for simplicity, while we will discuss other symmetries later. We calculate the energy functional of $\mathbf{m}_i$, which is obtained by integrating out the electron operators:

$$E[\{\mathbf{m}_{\boldsymbol{q}}\}] = \frac{2U}{3}\sum_{\boldsymbol{q}}\left(1 - \frac{2U}{3}\chi(\boldsymbol{q})\right)|\mathbf{m}_{\boldsymbol{q}}|^2, \tag{4.3.1}$$

where $\mathbf{m}_{\boldsymbol{q}}$ is the Fourier transform of $\mathbf{m}_i$, and we have taken the lowest order of $\mathbf{m}_{\boldsymbol{q}}$. $\chi(\boldsymbol{q}) > 0$ is the bare spin susceptibility under a supercurrent, where we note that the spin-rotational symmetry exists in the absence of the spin-orbit coupling (the effect of the spin-orbit coupling will be discussed later). The largest peak of $\chi(\boldsymbol{q})$ indicates an instability toward a magnetic order given by the corresponding mode $\mathbf{m}_{\mathbf{q}}$.

Here we show how a supercurrent changes the profile of $\chi(\boldsymbol{q})$ considering the low density limit in two dimensions at low temperature ($k_B T \ll |\Delta|$, where k_B is the Boltzmann constant and T is temperature). We define $\xi_{\boldsymbol{k}} = \frac{k^2}{2m} - \varepsilon_F$, where m is the electron mass, $\varepsilon_F \geq 0$ is the Fermi energy and we set the reduced Planck constant $\hbar = 1$. In a normal state ($\Delta = 0$), $\chi(\boldsymbol{q})$ is constant and largest for $|\boldsymbol{q}| \leq 2k_F$ with $k_F = \sqrt{2m\varepsilon_F}$, i.e., all modes of $\mathbf{m}_{\mathbf{q}}$ with $|\boldsymbol{q}| < 2k_F$ energetically degenerate in Eq. (4.3.1). With an s-wave singlet correlation without a supercurrent ($\Delta \neq 0$, $\boldsymbol{\kappa} = \mathbf{0}$), $\chi(\boldsymbol{q})$ is suppressed around $\boldsymbol{q} = \mathbf{0}$ because of the spin gap associated with the superconductivity [Fig. 4.2(a)]. This is called the Anderson-Suhl mechanism [189]. Now, $\chi(\boldsymbol{q})$ is further deformed from the ring structure by applying a supercurrent given by $\mathbf{j}^{\mathrm{sc}} = -e\frac{n_{\mathrm{sf}}}{m}\boldsymbol{\kappa}$ with the electron charge $-e$ and the superfluid density n_{sf}. A supercurrent introduces peak structures around $\boldsymbol{q}^* \sim \pm 2k_F\hat{\boldsymbol{\kappa}}$ [Fig. 4.2(b)], with $\hat{\boldsymbol{\kappa}} = \boldsymbol{\kappa}/|\boldsymbol{\kappa}|$.

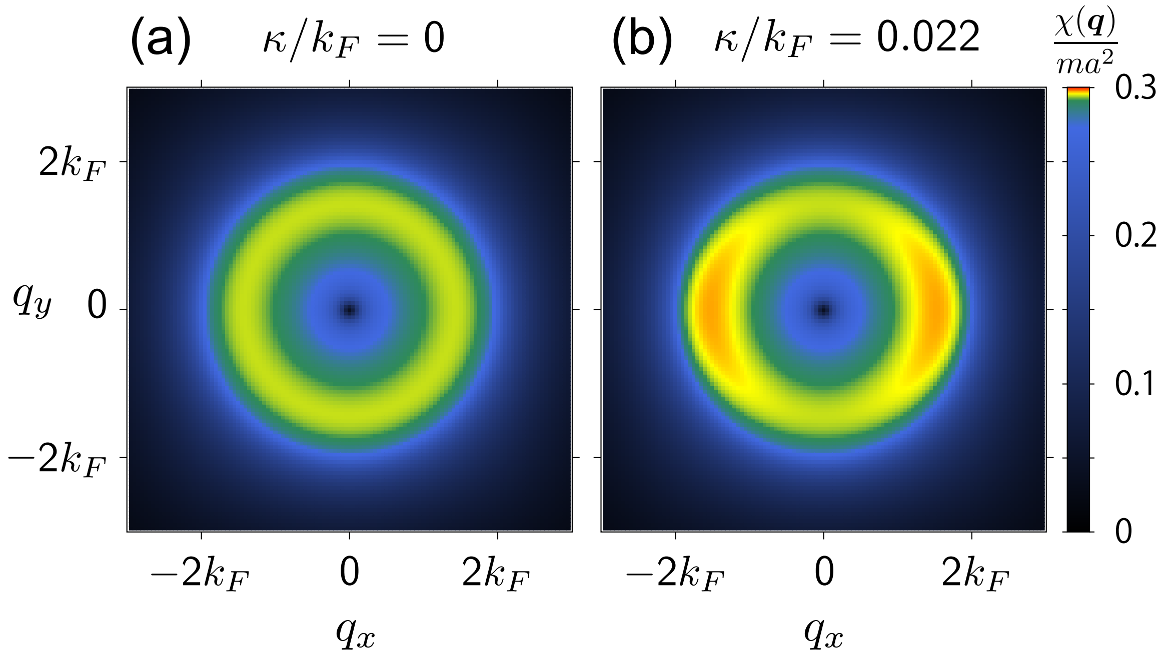

Figure 4.2: Bare spin susceptibility $\chi(\boldsymbol{q})$ in the low density limit for $|\Delta|/\varepsilon_F = 0.05$ and $k_BT/|\Delta| = 1/40 \ll 1$ (a) without a supercurrent ($\boldsymbol{\kappa} = \boldsymbol{0}$) and (b) with a supercurrent $\boldsymbol{\kappa}/k_F = (0.022, 0)$.

Such an increase induced by a supercurrent can be analytically obtained for a small current density. For $k_BT \ll |\Delta|$, we can expand $\chi(\boldsymbol{q})$ to the second order of $\boldsymbol{\kappa}$ as

$$\chi(\boldsymbol{q}) - \chi_{\boldsymbol{\kappa}=\boldsymbol{0}}(\boldsymbol{q}) = \frac{a_0^2|\boldsymbol{\kappa}|^2}{\varepsilon_F} f\left(\frac{q}{k_F}, \frac{|\Delta|}{\varepsilon_F}\right) + \frac{a_0^2\left(\boldsymbol{\kappa}\cdot\hat{\boldsymbol{q}}\right)^2}{\varepsilon_F} g\left(\frac{q}{k_F}, \frac{|\Delta|}{\varepsilon_F}\right), \tag{4.3.2}$$

where $\chi_{\boldsymbol{\kappa}=\boldsymbol{0}}(\boldsymbol{q})$ is the bare spin susceptibility at $\boldsymbol{\kappa} = \boldsymbol{0}$, a_0 stands for the inverse of the momentum cutoff , $f(x, y)$ and $g(x, y)$ are the dimensionless functions, and we define $q = |\boldsymbol{q}|$ and $\hat{\boldsymbol{q}} = \boldsymbol{q}/q$. The directional dependence arises from the second term in the right-hand side, and $g\left(\frac{q}{k_F}, \frac{|\Delta|}{\varepsilon_F}\right)$ is proved to be positive and has a peak around $q \sim 2k_F$. We also note that, for $|\Delta|/\varepsilon_F \ll 1$, we obtain $|g(q/k_F, |\Delta|/\varepsilon_F)| \gg |f(q/k_F, |\Delta|/\varepsilon_F)|$ [2]. As a result, $\chi(\boldsymbol{q})$ increases around $\boldsymbol{q}^* \sim \pm 2k_F\hat{\boldsymbol{\kappa}}$ by a supercurrent, and the magnetic instability with the particular wave number $\boldsymbol{q}^*$ is selected out of the degenerate ring. Although the effect is small in the low density limit, below we will show that it can be enhanced in generic cases.

[2]See Sec. 4.6 for the details of $f(x, y)$ and $g(x, y)$.

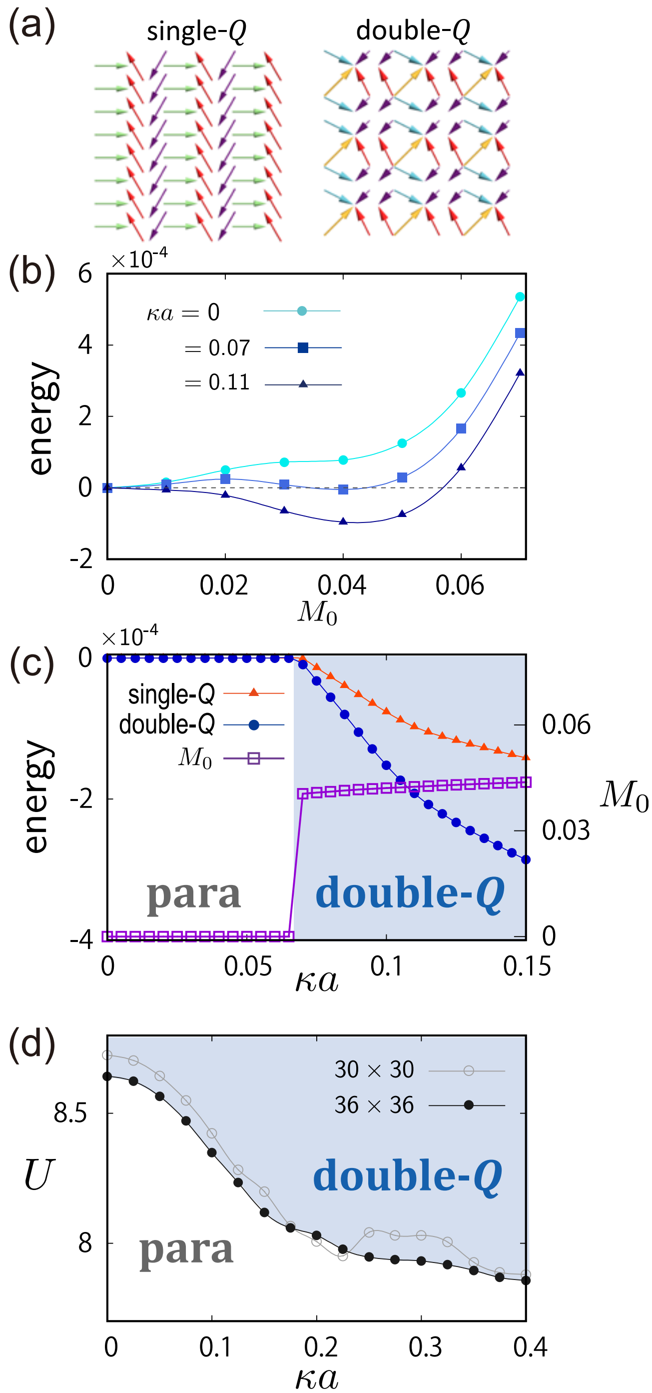

Figure 4.3: Magnetic ordering induced by a supercurrent given by $\boldsymbol{\kappa} = \frac{\kappa}{\sqrt{2}}(1,1)$. (a) Schematic pictures of a single-Q state (left) and a double-Q state (right). (b) Energy of the double-Q state as a function of M_0 for different κ at $U = 8.58$. The energies are measured from those with $M_0 = 0$. (c) Energies of the single-Q and double-Q states and the magnetization of the double-Q state as functions of κ at $U = 8.58$. (d) κa-U phase diagram for the ground state. Phase boundaries obtained in different system sizes are plotted.

4.4 Magnetic phase diagram

On a lattice with a higher density of electrons, the bare spin susceptibility $\chi(\boldsymbol{q})$ is no longer isotropic: it generally has peak structures even without a supercurrent, reflecting the lattice structure and the energy dispersion. Therefore, magnetic instabilities arise from the interplay of the anisotropy of $\chi(\boldsymbol{q})$ and the current direction.

In the following, we investigate magnetic ground-state phase diagrams for a lattice model numerically. We consider a square-lattice model with the energy dispersion $\xi_{\boldsymbol{k}} = -2t(\cos(k_x a) + \cos(k_y a)) - \mu$, where t denotes the hopping amplitude between the nearest-neighbor sites, a is the lattice constant, and μ is the chemical potential. In the calculations, we set $t = 0.5$, $\mu = -1.48$, and $\Delta = 0.05$. With these parameters, $\chi_{\boldsymbol{\kappa}=\boldsymbol{0}}(\boldsymbol{q})$ has four equivalent peaks at $\boldsymbol{q} = (q_x, q_y) = (\pm Q^*, 0),\ (0, \pm Q^*)$ with $Q^* \simeq 2\pi/3a$.

To elucidate the ground-state phase diagram in the presence of the supercurrent, we perform variational calculations. Referring to the previous studies [76, 77, 190], we assume two variational ansatz for magnetic configurations: helical (single-Q) and vortexlike (double-Q) states, which are described by

$$\mathbf{m}_i^{1Q} = M_0 \begin{pmatrix} \cos(Qx_i) \\ \sin(Qx_i) \\ 0 \end{pmatrix}, \quad \mathbf{m}_i^{2Q} = M_0 \begin{pmatrix} \cos(Qx_i) \\ \cos(Qy_i) \\ 0 \end{pmatrix}, \tag{4.4.1}$$

respectively [Fig. 4.3(a)]. Here M_0 is the amplitude of the magnetization and Q is the wave number of modulation, and they are the variational parameters [3]. The single-Q state is characterized by a single mode, $\mathbf{m}_{\boldsymbol{q}=(Q,0)}$, while the double-$Q$ state consist of two modes: $\mathbf{m}_{\boldsymbol{q}=(Q,0)}$ and $\mathbf{m}_{\boldsymbol{q}=(0,Q)}$ [4].

We numerically diagonalize the mean-field Hamiltonian $H_0 + H_U^{\mathrm{MF}}$ by substituting Eq. (4.4.1) for finite-size systems with the open boundary conditions, and obtain the ground state energy. The results for 30×30 sites are shown in Figs. 3 and 4, while Fig. 3(d) also shows the result for 36×36 sites.

First, we consider a supercurrent given by $\boldsymbol{\kappa} = (\kappa_x, \kappa_y) = \frac{\kappa}{\sqrt{2}}(1, 1)$. In this case, the four peaks in $\chi(\boldsymbol{q})$ at $\boldsymbol{q} = (\pm Q^*, 0)$ and $(0, \pm Q^*)$ are equally enhanced. In Fig. 4.3(b), we show the M_0 dependence of the energies of the double-Q state for several values of κa, where the energies are measured from that with $M_0 = 0$. We note that the energy for the single-Q state is always higher than that for the double-Q state. For small κ, the system is in the paramagnetic state ($M_0 = 0$). With κ increased, the first-order phase transition to the double-Q ordered state occurs, and the magnetization M_0 shows a jump at the transition. Figure 4.3(c) shows the κ dependences of the system energies for the single-Q and double-Q

[3] We consider Q at and close to the peak of $\chi(\boldsymbol{q})$.

[4] We note that the stability of the double-Q state might be underestimated with the above simple ansatz, as a noncoplanar component is neglected [190]

ordered states and the magnetic moment in the double-Q state. For κ larger than the critical value, the double-Q ordered state has the lower energy than the paramagnetic state as well as the single-Q state. Therefore, the supercurrent induces a magnetic order transition from the paramagnetic state to the double-Q state. The critical κ is summarized in the ground-state phase diagram in Fig. 4.3(d). The result shows that a larger supercurrent induces the magnetic instability at a smaller interaction strength U. We note that, for large $\kappa a > 0.15$, the jump of M_0 becomes small (not shown), suggesting that the phase transition can possibly be continuous in the large κ region. The features found here are confirmed at different system sizes, and the phase boundary becomes smoother for the larger system [Fig. 4.3(d)].

Furthermore, the stable magnetic state can be switched by changing the supercurrent direction, as the peaks of $\chi(\boldsymbol{q})$ can be modulated independently depending on the current direction. For example, once a current is applied along the x direction, the instability of $\mathbf{m}_{\boldsymbol{q}=(Q,0)}$ is enhanced compared to $\mathbf{m}_{\boldsymbol{q}=(0,Q)}$. To demonstrate how the stable magnetic state changes, let us rotate the current direction from $(1,1)$ to $(1,0)$ by defining $\boldsymbol{\kappa} = \kappa(\cos(45^\circ - \delta\theta), \sin(45^\circ - \delta\theta))$ [the inset of Fig. 4.4(a)]. Figure 4.4(a) shows the energies for the single-Q and double-Q states as functions of the current angle $\delta\theta$. While increasing $\delta\theta$, the double-Q order switches to a single-Q order, which remains stable up to $\delta\theta = 45^\circ$, i.e., for the current along the x direction. The resulting phase diagram while changing U is summarized in Fig. 4.4(b).

Realistic values of κ/k_F depend on the property of the bulk superconductor and the correlated metal, where k_F is the Fermi momentum in the correlated metal. At a low temperature, the upper limit is ideally given by $\kappa/k_F < (\xi k_F)^{-1}$ with ξ being the coherence length of the bulk superconductor [191]. To reach a larger κ/k_F, it is desired to use a superconductor with a higher upper critical field $\propto \xi^{-2}$ and a correlated metal with a lower carrier density. For example, the coherence length of the canonical s-wave superconductor MgB_2 is $a/\xi \sim 10^{-1}$ [192], and hence, κ/k_F may be of the order of $10^{-1} \sim 1$ depending on $k_F a$. The parameter used in Fig. 4.3(d) is within this range. We note that the above upper limit can be lower due to the orbital depairing, which could be suppressed by the geometry of the superconductor to some extent [191].

Other gap symmetries

We have discussed an s-wave pairing, which has a nodeless isotropic gap in the momentum space. Node structures in the superconducting gap render the bare spin susceptibility anisotropic as a lattice does, and the magnetic instability is enhanced particularly for $\boldsymbol{q}$ in the directions of the nodes. For example, a $d_{x^2-y^2}$-wave gap has nodes in the $(\pm\pi, \pm\pi)$ direction, and the magnetic modes $\mathbf{m}_{\boldsymbol{q}\sim(\pm Q,\pm Q)}$ have the dominant instability in the absence of supercurrent. Thus, the stable magnetic state is further flexibly controlled by the pairing symmetry in addition to the current direction, lattice geometry, and energy dispersion.

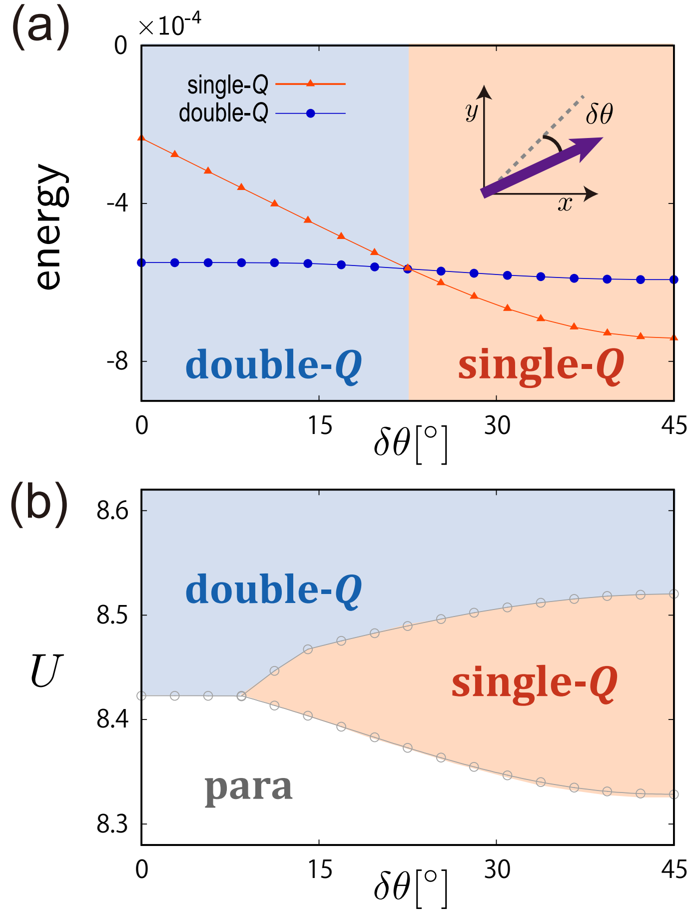

Figure 4.4: Switching of magnetic orders by the supercurrent direction. (a) Energies of the single-Q and double-Q states as functions of the angle $\delta\theta$ at $U = 8.49$. (b) $\delta\theta$-U phase diagram for the ground state.

Rashba spin-orbit coupling

At the interface between a metal and a superconductor, the Rashba spin-orbit coupling may be important due to the broken mirror symmetry along the z axis, the out-of-plane direction. It can be written as

$$H_{so} = \alpha \sum_{\boldsymbol{k}} \mathbf{g}(\boldsymbol{k}) \cdot (c^{\dagger}_{\boldsymbol{k}\sigma_1} \boldsymbol{\sigma}_{\sigma_1\sigma_2} c_{\boldsymbol{k}\sigma_2}), \tag{4.4.2}$$

where α is the magnitude of the Rashba spin-orbit coupling and $\mathbf{g}(\boldsymbol{k}) = (k_y a_0, -k_x a_0, 0)$ in the continuum limit. The spin-orbit coupling breaks the spin rotational symmetry, and Eq. (4.3.1) is replaced by $E[\{\mathbf{m}_{\boldsymbol{q}}\}] = \frac{2U}{3} \sum_{\boldsymbol{q}} \left(1 - \frac{2U}{3}\chi^{\mu\nu}(\boldsymbol{q})\right) m^{\mu}_{-\boldsymbol{q}} m^{\nu}_{\boldsymbol{q}}$. Thus, the magnetic instability is dictated by the peak wave number in the anisotropic susceptibility tensor $\chi^{\mu\nu}(\boldsymbol{q})$.

More importantly, with a supercurrent, superconducting analog of the Edelstein effect arises [174]. A spin polarization is induced by the supercurrent flow owing to the absence of the mirror symmetry. The first-order correction of κ leads to the additional term in the energy functional as

$$\delta E[\{\mathbf{m}_{\boldsymbol{q}}\}] = \mathcal{K} \sum_i (\hat{\mathbf{z}} \times \boldsymbol{\kappa}) \cdot \mathbf{m}_i, \tag{4.4.3}$$

where $\mathcal{K}$ is the odd function of α, and $\hat{\mathbf{z}}$ is the unit vector in the z direction. This term acts like an in-plane magnetic field, e.g., a supercurrent in the x direction gives an effective magnetic field in the y direction. This results in the modulation of the noncollinear spin textures.

Hence, the Rashba spin-orbit coupling locks the spin-spiral plane by the spin anisotropy, and moreover, modulates the spin texture by combining with a supercurrent. Even in this case, we believe that our mechanism to control stable magnetic orders remains robust, as $\chi^{\mu\nu}(\boldsymbol{q})$ is modified by a supercurrent. It would be interesting to explore the resulting magnetic phase diagrams, and we leave further discussion for future work.

4.5 Summary and discussion

To summarize, we have proposed a way to induce and switch noncollinear spin textures by a supercurrent in the presence of the superconducting proximity effect. Our results can be useful to realize and control physics raised by the interplay between superconductivity and noncollinear magnetism, e.g., singlet-triplet conversion of Cooper pairs and engineering topological superconductivity.

The mechanism behind is general, as we have shown in the continuum model. Using different lattice geometries as well as different pairing symmetries, we can control a broad range of magnetic states. For example, we might be able to create and annihilate Skyrmions by a supercurrent in a triangular lattice, noting that Skyrmion crystals can be realized in the Kondo lattice model [75].

Due to the first-order nature of the transition in an s-wave case, it would be interesting to explore what happens with a supercurrent being switched off. It is important, especially for the application, to clarify whether the magnetic order persists as a metastable state, and how the phase of pairing and magnetic order relax.

The mechanism studied in this chapter can also be applied to the Kondo lattice systems, where conduction electrons couple to localized moments. It suggests that not only a heterostructure composed of a heavy-fermion compound and a superconductor but also a heavy-fermion superconductor can lead to further rich control of magnetism, owing to complex magnetic interactions inherent in the heavy-fermion systems.

4.6 Details

4.6.1 Spin susceptibility

The bare spin susceptibility $\chi(\boldsymbol{q})$ in Eq. (2.3.12) can be calculated by

$$\chi(\boldsymbol{q}) = -\frac{T}{2N}\sum_{n,\boldsymbol{k}} \mathrm{tr}[\mathcal{G}_{\boldsymbol{k}+\boldsymbol{q}}(\varepsilon_n)\mathcal{G}_{\boldsymbol{k}}(\varepsilon_n)], \tag{4.6.1}$$

where the Green function $\mathcal{G}_{\boldsymbol{k}}(\varepsilon_n)$ is 4×4 matrix given by

$$\mathcal{G}_{\boldsymbol{k}}(\varepsilon_n) = \begin{pmatrix} (i\varepsilon_n - \xi_{\boldsymbol{k}+\boldsymbol{\kappa}})\,\mathbb{I}_2 & -\Delta(i\sigma^y) \\ -\Delta^*(i\sigma^y)^\dagger & (i\varepsilon_n + \xi_{-\boldsymbol{k}+\boldsymbol{\kappa}})\,\mathbb{I}_2 \end{pmatrix}^{-1}, \tag{4.6.2}$$

$\mathbb{I}_2 = \mathrm{diag}(1,1)$, $\varepsilon_n = T(2n+1)\pi$ is the Matsubara frequency, and we take $k_B = 1$ in the following.

A supercurrent changes the profile of $\chi(\boldsymbol{q})$ as discussed in the previous sections. Figure 4.5(a) shows the profile of $\chi(\boldsymbol{q} \parallel \boldsymbol{\kappa})$ for $\boldsymbol{\kappa} = \kappa\hat{\boldsymbol{x}}$, and the increase is the largest at $q_x \sim 2k_F$ in the continuum model. For a small current density, the change induced by a supercurrent can be described by the dimensionless functions $f(x,y)$ and $g(x,y)$ [Eq. (4.5)]. $f(x,y)$ and $g(x,y)$ are given by

$$f(x,y) = \frac{1}{2\pi^2}\int_0^{\frac{2\pi}{k_F a_0}}\int_0^{2\pi} \tilde{k}d\tilde{k}d\theta \frac{\sqrt{\tilde{\xi}_1^2+y^2}\left(y^2(-2\tilde{\xi}_1+\tilde{\xi}_2)-\tilde{\xi}_1^2\tilde{\xi}_2\right)+\sqrt{\tilde{\xi}_2^2+y^2}(\tilde{\xi}_1^3+y^2\tilde{\xi}_2)}{\sqrt{(\tilde{\xi}_1^2+y^2)^3(\tilde{\xi}_2^2+y^2)}(\sqrt{(\tilde{\xi}_1^2+y^2)}+\sqrt{(\tilde{\xi}_2^2+y^2)})^2}, \tag{4.6.3}$$

$$g(x,y) = \frac{x^2}{\pi^2}\int_0^{\frac{2\pi}{k_F a_0}}\int_0^{2\pi} \tilde{k}d\tilde{k}d\theta \frac{\sqrt{(\tilde{\xi}_1^2+y^2)(\tilde{\xi}_2^2+y^2)}-\tilde{\xi}_1\tilde{\xi}_2-y^2}{\sqrt{(\tilde{\xi}_1^2+y^2)(\tilde{\xi}_2^2+y^2)}(\sqrt{(\tilde{\xi}_1^2+y^2)}+\sqrt{(\tilde{\xi}_2^2+y^2)})^3}, \tag{4.6.4}$$

where we define $\tilde{\xi}_1 = \tilde{k}^2 - 1$ and $\tilde{\xi}_2 = \tilde{k}^2 + 2\tilde{k}x\cos\theta + x^2 - 1$. We can prove that $g\,(x,y)$ is always positive noting the relation $\sqrt{(\tilde{\xi}_1^2+y^2)(\tilde{\xi}_2^2+y^2)} > |\tilde{\xi}_1\tilde{\xi}_2 + y^2|$.

Figure 4.5(b) shows the numerical values of the above functions. $g\left(\frac{q}{k_F}, \frac{|\Delta|}{\varepsilon_F}\right)$, which gives the anisotropic change in $\chi(\boldsymbol{q})$, has a peak at $q \sim 2k_F$. We also note that, around the peak, $g\left(\frac{q}{k_F}, \frac{|\Delta|}{\varepsilon_F}\right)$ is much larger than $f\left(\frac{q}{k_F}, \frac{|\Delta|}{\varepsilon_F}\right)$, which gives the isotropic change.

4.6.2 Energy functional with the Rashba SO coupling

In this section, we show the derivation of Eq. (4.4.3). The the energy functional of $\mathbf{m}_i$ in the presence of the Rashba spin-orbit coupling is given by

$$E[\{\mathbf{m}_{\boldsymbol{q}}\}] = \frac{2U}{3}\left(\sum_i m_i^\mu\right)\frac{T}{N}\sum_{n,\boldsymbol{k}}\mathrm{tr}[S^\mu\mathcal{G}_{\boldsymbol{k}}^{\mathrm{so}}(\varepsilon_n)] + \frac{2U}{3}\sum_{\boldsymbol{q}} m_{-\boldsymbol{q}}^\mu m_{\boldsymbol{q}}^\nu\left(\delta_{\mu\nu} - \frac{2U}{3}\chi^{\mu\nu}(\boldsymbol{q})\right), \tag{4.6.5}$$

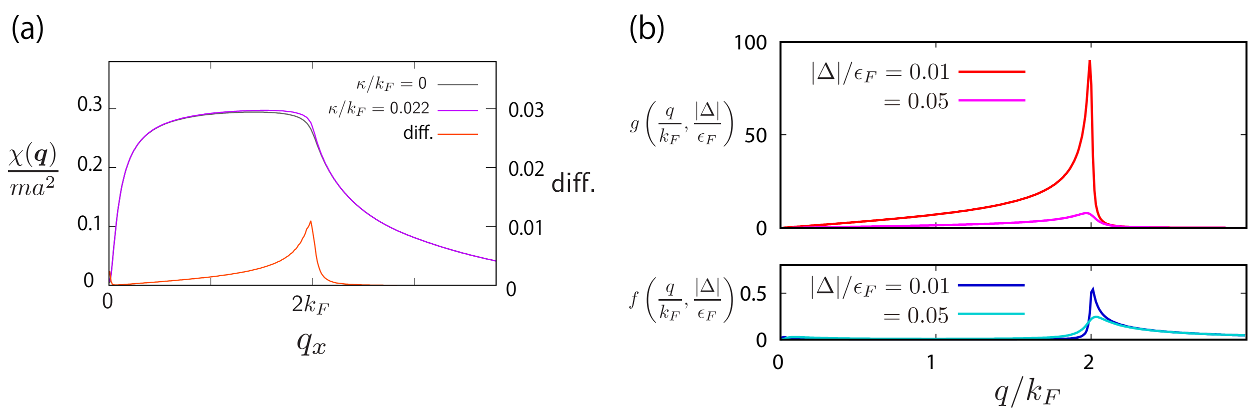

Figure 4.5: Increase in $\chi(\boldsymbol{q})$ induced by a supercurrent ($\boldsymbol{\kappa} = \kappa\hat{\boldsymbol{x}}$). (a) $\chi(\boldsymbol{q} \,||\boldsymbol{\kappa})$ without a supercurrent ($\kappa = 0$) and with a supercurrent $\kappa/k_F = 0.022$, and the difference (diff.) between them. The difference is largest at $q_x \sim 2k_F$. (b) $g\left(\frac{q}{k_F}, \frac{|\Delta|}{\varepsilon_F}\right)$ and $f\left(\frac{q}{k_F}, \frac{|\Delta|}{\varepsilon_F}\right)$ for different Δ/ε_F.

where we have defined the Green function with the spin-orbit coupling, the spin matrices in the Nambu representation, and the bare spin susceptibility as

$$(\mathcal{G}^{\mathrm{so}}_{\boldsymbol{k}}(\varepsilon_n))^{-1} = (\mathcal{G}_{\boldsymbol{k}}(\varepsilon_n))^{-1} - \begin{pmatrix} \alpha\mathbf{g}(\boldsymbol{k}+\boldsymbol{\kappa})\cdot\boldsymbol{\sigma} & \\ & -\alpha\mathbf{g}(-\boldsymbol{k}+\boldsymbol{\kappa})\cdot\boldsymbol{\sigma}^{\mathrm{T}} \end{pmatrix}, \tag{4.6.6}$$

$$S^{\mu} = \begin{pmatrix} \sigma^{\mu} & \\ & -(\sigma^{\nu})^{\mathrm{T}} \end{pmatrix}, \tag{4.6.7}$$

$$\chi^{\mu\nu}(\boldsymbol{q}) = -\frac{T}{2N}\sum_{n,\boldsymbol{k}} \mathrm{tr}[S^{\mu}\mathcal{G}^{\mathrm{so}}_{\boldsymbol{k}+\boldsymbol{q}}(\varepsilon_n)S^{\nu}\mathcal{G}^{\mathrm{so}}_{\boldsymbol{k}}(\varepsilon_n)]. \tag{4.6.8}$$

The bare spin susceptibility is the anisotropic tensor due to the broken spin rotational symmetry.

Let us focus on the first term in Eq. (4.6.5). We consider the continuum model with $\xi_{\boldsymbol{k}} = \frac{k^2}{2m} - \varepsilon_F$, $\mathbf{g}(\boldsymbol{k}) = (k_y a_0, -k_x a_0, 0)$, and the supercurrent $\boldsymbol{\kappa} = \kappa\hat{\boldsymbol{x}}$ ($\kappa a \ll 1$). We obtain

$$\frac{2U}{3}\frac{T}{N}\sum_{n,\boldsymbol{k}} \mathrm{tr}[S^{\mu}\mathcal{G}^{\mathrm{so}}_{\boldsymbol{k}}(\varepsilon_n)] = \mathcal{K}\delta_{\mu y}\kappa, \tag{4.6.9}$$

to the lowest order of κ, where

$$\mathcal{K} = -\frac{2U}{3}\frac{T}{N}\sum_{n,\boldsymbol{k}} \mathrm{tr}[S^{y}\mathcal{G}^{0}_{\boldsymbol{k}}(\varepsilon_n)\left(\partial_{\kappa_x}\mathcal{G}^{0}_{\boldsymbol{k}}(\varepsilon_n)^{-1}\right)\mathcal{G}^{0}_{\boldsymbol{k}}(\varepsilon_n)], \tag{4.6.10}$$

$$\tag{4.6.11}$$

with $\mathcal{G}^{0}_{\boldsymbol{k}}(\varepsilon_n) = \mathcal{G}^{\mathrm{so}}_{\boldsymbol{k}}(\varepsilon_n)|_{\kappa=0}$. $\mathcal{K}$ is the odd function of α, and the explicit form is given by

$$\mathcal{K} = -\frac{4U\alpha^3 a_0^5|\Delta|^2}{3}\int\frac{d^2k}{(2\pi)^2}\frac{k_y^2}{(\xi_{\boldsymbol{k}}^2+|\Delta|^2)^{5/2}}, \tag{4.6.12}$$

to the lowest order of α at low temperature $T \ll \Delta$. For the general direction of supercurrents, we have Eq. (4.4.3).

Chapter 5

Quantum effects on skyrmion texture

This chapter is going to present a future direction of this research. Thus far, we have discussed the *classical* spin textures, such as a domain wall, a skyrmion, and a vortexlike order. Now we are going to study quantum effects on spin textures, and show that they result in a new quantum phase and critical phenomena. We believe that intertwined with superconductivity, they will further give rise to versatile phenomena. We leave this for future work.

In this chapter, we study the quantum effects on magnetic skyrmions in the vicinity of the skyrmion crystal to ferromagnet phase boundary in two-dimensional magnets. Condensation of the skyrmions gives rise to an intermediate phase between the skyrmion crystal and ferromagnet: a quantum liquid, in which skyrmions are not spatially localized. We show that the critical behavior depends on the spin size S and the topological number of the skyrmion.

The organization of this chapter is as follows. In Sec. 5.1, we give the background and the aim of this chapter. In Sec. 5.2, starting from a two-dimensional spin model on a lattice, we derive the low energy effective action for single skyrmion excitations. We include the effect of the underlying lattice, which cannot be neglected for small skyrmions. Then, from the effective action, we calculate the energy dispersion of the low energy excitation. Section 5.3 presents the phase diagram and the critical phenomena in light of the skyrmion spectrum. In Sec. 5.4, we give a summary and discussion. Section 5.5 provides the detail of the calculations in this chapter.

5.1 Introduction to this chapter

As we have already introduced in Sec. 1.3.2, a magnetic skyrmion is a localized spin texture characterized by an integer topological index called the skyrmion number [Eq. 1.3.5]. Skyrmions have been recently discovered[159, 65, 67] in chiral magnets and have attracted broad interest due to the extraordinary properties.[193, 175, 194, 195, 196, 160] Typically they appear in a periodic SkX phase, examples of which are being continuously discovered. Some specific properties of the skyrmions, such as their size, vary from system to system. For instance, the size of skyrmions in $Fe_{0.5}Co_{0.5}Si$ thin films is ~ 90 nm ,[67] while skyrmions on Fe thin film deposited on the Ir surface are ~ 1 nm.[197] In addition, possible realizations of SkX phases in classical frustrated magnets have been studied theoretically [73, 74, 198]; their size is comparable to the lattice spacing.

In thin films of $Fe_{0.5}Co_{0.5}Si$, the SkX and adjacent phases have been observed by real-space imaging in the presence of a magnetic field [67]. In the high field region just below the phase boundary between the field-induced ferromagnetic (FM) phase and the SkX phase, a small number of skyrmions are nucleated in the FM state. On reducing the field, the number of skyrmions increases, and they eventually form a dense crystal. It is known that skyrmions in thin films including this material remain stable in the wide range of temperature from the order of $\sim$ 100K[69] to nearly zero temperature[67, 199].

In the work discussed above, a classical description of the spins is sufficient, and skyrmions may simply be regarded as textures of quasi-static vector moments. Here, we pursue the possibility of observing skyrmions in the quantum realm. Several basic theoretical questions arise: What are the quantum states of a skyrmion? What is the corresponding spectrum, and what are the quantum numbers associated with a skyrmion? Is a skyrmion a quasiparticle? How do quantum effects change universal properties of skyrmion systems? Are there new skyrmion phases besides the SkX one induced by quantum dynamics? Practically, we would also like to understand observable consequences of quantum skyrmions, and when they should be visible. Clearly, quantum effects are strongest when the spin quantum number S and the skyrmion diameter L_s is small. One would like to understand their magnitude, and how it scales with these parameters. We address these questions and provide some first answers in this work.

First, we argue that a skyrmion indeed becomes a quasiparticle in the appropriate quantum regime. This occurs close to the phase boundary between the FM and SkX phases, at zero temperature. Here, for systems with large skyrmions such as $Fe_{0.5}Co_{0.5}Si$, the FM/SkX transition is understood to be of the so-called "nucleation" type [200, 201]; it is not associated with a small order parameter. This implies that a small deviation of the order parameter, like a magnon, costs more energy than the excitation of a skyrmion, at least close to the phase boundary of the FM state (Fig. 5.2.1). This allows, in a quantum description, the skyrmion to become a stable quasiparticle. In this limit, we show that a skyrmion excitation has a non-trivial band structure, which depends on the spin S and the skyrmion number $\mathcal{N}$. This structure is the quantum descendent of the well-known Magnus force dynamics of classical skyrmions. The skyrmion states can be probed by inelastic neutron scattering within the FM phase. They are clearly distinct from magnons in possessing many bands (while a FM state has a single magnon branch), with particle dispersion and spectral weight characteristic of skyrmions.

Next, we consider how quantum dynamics modifies the classical nucleation transition. The nucleation scenario works well if skyrmions are fully classical, in other words, the size of a skyrmion is much larger than the lattice spacing of the underlying lattice. However, the fate of this transition is nontrivial when the skyrmion develops a quantum nature, which can be prominent for small skyrmions, especially when the density is low enough so that they do not form a classical crystal. We find that skyrmions can undergo a variant of *Bose condensation* to form a quantum liquid phase between the FM and SkX phases. We also show that this phase is connected to the FM phase via a phase transition or a crossover depending on the parity of $2S\mathcal{N}$.

5.2 Single particle excitation in the saturated phase

In this section, we study a single particle excitation of a skyrmion in a quantum regime.

5.2.1 Effective Action

We first introduce the effective action for a single skyrmion excitation that includes the effects of the underlying crystal lattice.

We start with the quantum counterpart of an effective Hamiltonian for two dimensional chiral magnets.

$$\hat{H} = -J\sum_{\langle i,j\rangle}\hat{\boldsymbol{S}}_i\cdot\hat{\boldsymbol{S}}_j + D\sum_i\sum_{\mu=x,y}\boldsymbol{e}_\mu\cdot\left(\hat{\boldsymbol{S}}_i\times\hat{\boldsymbol{S}}_{i+\boldsymbol{e}_\mu}\right) - B\sum_i\hat{S}^z_i - K\sum_i(\hat{S}^z_i)^2. \tag{5.2.1}$$

Here, $\hat{\boldsymbol{S}}$ is the spin operator for spin size S, the first term is the ferromagnetic ($J > 0$) exchange coupling between the nearest neighbor spins, taken for simplicity on a square lattice, and the second term is the Dyaloshinskii-Moriya coupling. B is the external magnetic field perpendicular to the plane, and the last term is an uniaxial anisotropy.

In this work, we focus on the vicinity of the phase boundary between the FM and SkX phase. While a skyrmion has a large energy under a very high field as $\sim BS(L_s/a)^2$, with the size of a skyrmion L_s and the lattice spacing a, it has the lower energy than a magnon close to the phase boundary of the SkX phase (Fig. 5.2.1). We thus only consider a skyrmion excitation as the low energy excitation.

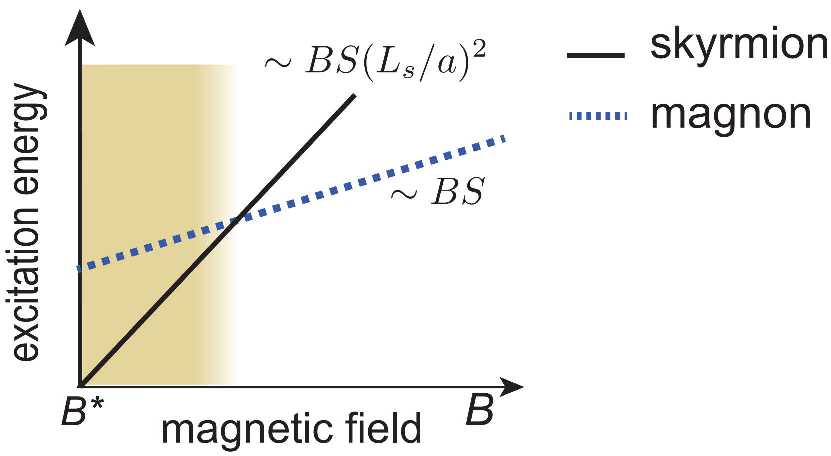

Figure 5.1: Schematic field dependence of the excitation energy. L_s is the characteristic length of skyrmions, and a is the lattice spacing. Our low energy effective theory focuses on the colored region, where a skyrmion is the lowest excitation.

To obtain the effective action for single skyrmion, we use the path integral formalism. At each site labeled by i, the state $|\boldsymbol{n}_i\rangle$ is parametrized by a unit vector $\boldsymbol{n}_i = (\sin\theta_i \cos\phi_i, \sin\theta_i \sin\phi_i, \cos\theta_i)$ to give $\langle \boldsymbol{n}_i|\hat{\boldsymbol{S}}_i|\boldsymbol{n}_i\rangle = S\boldsymbol{n}_i$. The whole system is represented by a product state of all the sites: $|\Psi(\tau)\rangle = \otimes_i |\boldsymbol{n}_i(\tau)\rangle$. The distribution function and the action are given by,

$$Z = \int \prod_i \mathcal{D}\boldsymbol{n}_i(\tau) \exp(-\mathcal{S}[\{\boldsymbol{n}_i\}]), \tag{5.2.2}$$

$$\mathcal{S}(\{\boldsymbol{n}_i\}) = iS \int d\tau \sum_i \dot{\boldsymbol{n}}_i \cdot \boldsymbol{A}(\boldsymbol{n}_i) + \int d\tau H(\{\boldsymbol{n}_i\}). \tag{5.2.3}$$

The first term in the action is the Berry phase term, where the explicit form of $\boldsymbol{A}(\boldsymbol{n}_i)$ depends on the gauge choice, e.g. $\dot{\boldsymbol{n}}_i \cdot \boldsymbol{A}(\boldsymbol{n}_i) = \dot{\phi}_i(1 - \cos\theta_i)$ for a certain gauge. The second term is $\mathrm{H}(\{\boldsymbol{n}_i\}) = \langle \Psi(\tau)|\hat{H}|\Psi(\tau)\rangle$.

To study the skyrmion excitations, we consider a single skyrmion configuration of $\boldsymbol{n}_i$: $\boldsymbol{n}_i = \boldsymbol{n}_{sk}(\boldsymbol{r}_i - \boldsymbol{R}(\tau))$. $\boldsymbol{n}_{sk}(\boldsymbol{r})$ is the unique continuous $O(3)$ vector field with a skyrmion centered at the origin that minimizes the classical energy in the continuum limit. While it cannot be obtained explicitly, $\boldsymbol{n}_{sk}(\boldsymbol{r})$ is fully specified in this way and we can use it successfully. $\boldsymbol{R}(\tau) = (X(\tau), Y(\tau))$ is the position of the skyrmion.

The resulting effective action for single skyrmion is given by

$$\mathcal{S}_{\text{eff}}(\boldsymbol{R}) = \int d\tau \left[\frac{2\pi i S\mathcal{N}}{a^2}(Y\dot{X} - X\dot{Y}) + g\left(\cos\left(\frac{2\pi X}{a}\right) + \cos\left(\frac{2\pi Y}{a}\right)\right)\right], \tag{5.2.4}$$

where $\dot{X}$ ($\dot{Y}$) is the imaginary time derivative of X (Y), g is the magnitude of the periodic potential that arises from the underlying lattice, and $\mathcal{N}$ is the skyrmion number defined by

$$\mathcal{N} = \frac{1}{4\pi} \int d^2r \; \boldsymbol{n}_{sk}(\boldsymbol{r}) \cdot [\partial_x \boldsymbol{n}_{sk}(\boldsymbol{r}) \times \partial_y \boldsymbol{n}_{sk}(\boldsymbol{r})]. \tag{5.2.5}$$

The time derivative term arises from the Berry phase term, and has been derived by many authors.[161, 162, 163] It makes X and Y canonically conjugate, and yields the Magnus force in the classical motion of a skyrmion.

We obtain the periodic potential by considering the leading corrections to the continuum limit beginning with the lattice model. Under some assumptions, the magnitude is

$$g \sim \frac{2C}{\pi} \varepsilon L_s^2 \exp\left(-C\frac{L_s^2}{a^2}\right), \tag{5.2.6}$$

where ε ($\sim JS^2/a^2$) is the "energy density" of a skyrmion in the continuous limit, and $C \sim \mathcal{O}(1)$ is a dimensionless constant.

5.2.2 Energy spectrum

From the effective action in Eq. (5.2.4), we obtain the effective Hamiltonian of skyrmion via canonical quantization:

$$\hat{H}_{\text{eff}} = g\left(\cos\left(\frac{2\pi\hat{X}}{a}\right) + \cos\left(\frac{2\pi\hat{Y}}{a}\right)\right), \tag{5.2.7}$$

$$[\hat{X}, \hat{Y}] = \frac{ia^2}{4\pi S\mathcal{N}} \equiv \frac{ia^2}{2\pi \mathrm{p}}, \tag{5.2.8}$$

where $2SN_{sk} \equiv \mathrm{p} \in \mathbb{Z}$. The two position operators of skyrmion, X and Y, become commutative in the classical limit, $S \to \infty$, or in the large skyrmion limit, $a/L_s \to 0$.

To calculate the eigenstate, we first introduce the translation operators $T_1 \equiv e^{-2\pi i\hat{Y}/a}$ and $T_2 \equiv e^{2\pi i\hat{X}/a}$. These operators shift the position of a skyrmion by

$$T_1^\dagger \hat{X} T_1 = \hat{X} + \frac{a}{\mathrm{p}}, \tag{5.2.9}$$

$$T_2^\dagger \hat{Y} T_2 = \hat{Y} + \frac{a}{\mathrm{p}}, \tag{5.2.10}$$

due to the commutation relation in Eq. (5.2.8). These operators are non-commutative, $T_1T_2 = \exp(-2\pi i/\mathrm{p})\, T_2T_1$, but T_1 commutes with T_2^{p} (translation over the lattice spacing) and vice versa. In particular this implies further that T_1^{p} and T_2^{p} commute, which is a mathematical expression of the fact that the effective flux per unit cell is an integer multiple (p) of the flux quantum. Using these operators, the Hamiltonian is given by

$$\hat{H}_{\text{eff}} = \frac{g}{2}(T_1 + T_2) + \text{h.c.}. \tag{5.2.11}$$

To calculate the energy eigenstates, it is convenient to use a basis given by simultaneous eigenstates of T_1^{p} and T_2,

$$T_1^{\mathrm{p}}|k_x, k_y\rangle = e^{ik_x a}|k_x, k_y\rangle, \tag{5.2.12}$$

$$T_2|k_x, k_y\rangle = e^{ik_y a/\mathrm{p}}|k_x, k_y\rangle, \tag{5.2.13}$$

with $|k_x| \leq \pi/a$ and $|k_y| \leq |\mathrm{p}|\,\pi/a$. We choose a boundary condition such that the operation of T_1 on $|k_x, k_y\rangle$ yields

$$T_1|k_x, k_y\rangle = e^{ik_x a/\mathrm{p}}|k_x, k_y + 2\pi/a\rangle, \tag{5.2.14}$$

which implies that $|k_x, k_y + 2\pi\mathrm{p}/a\rangle = |k_x, k_y\rangle$. We also define $|k_x + 2\pi/a, k_y\rangle = |k_x, k_y\rangle$.

In this basis, the Hamiltonian is

$$\hat{H}_{\mathrm{eff}} = g \sum_{k_x, k_y} \cos\left(\frac{k_y a}{\mathrm{p}}\right) |k_x, k_y\rangle\langle k_x, k_y| + \frac{g}{2} \sum_{k_x, k_y} \left(e^{ik_x a/\mathrm{p}}|k_x, k_y + 2\pi/a\rangle\langle k_x, k_y| + \mathrm{h.c.}\right), \tag{5.2.15}$$

which is the same form as Harper's equation. [202] There are $|\mathrm{p}| = 2S|\mathcal{N}|$ split bands, and the eigenstates are given by

$$|\psi_{\alpha\boldsymbol{k}}\rangle = \sum_{\ell=0}^{\mathrm{p}-1} c_{\alpha,\boldsymbol{k}}(\ell)|k_x, k_y + 2\pi\ell/a\rangle, \tag{5.2.16}$$

where $\alpha = 0, \cdots, |\mathrm{p}| - 1$ is the band index, and their eigenenergies are $\mathcal{E}_{0,\boldsymbol{k}} \leq \cdots \leq \mathcal{E}_{|\mathrm{p}|-1,\boldsymbol{k}}$. The crystal momentum is restricted to $\{|k_x| \leq \pi/a, |k_y| \leq \pi/a\}$. Note that these states are the eigenstates of the lattice translation operators: $T_1^{\mathrm{p}}|\psi_{\alpha\boldsymbol{k}}\rangle = e^{ik_x a}|\psi_{\alpha\boldsymbol{k}}\rangle$ and $T_2^{\mathrm{p}}|\psi_{\alpha\boldsymbol{k}}\rangle = e^{ik_y a}|\psi_{\alpha\boldsymbol{k}}\rangle$.

The eigenenergies of Harper's equation are well studied.[203] In Fig. 5.2, we show the energy spectrum of the Hamiltonian (Eq. (5.2.15)). Fig. 5.3 shows the lowest band dispersion, which has a single minimum at $\boldsymbol{k}_{\min} = (0, 0)$ [$\boldsymbol{k}_{\min} = (\pm\pi, \pm\pi)$] when $\mathrm{p} = 2S\mathcal{N}$ is even (odd). The value of $\boldsymbol{k}_{\min}$ alters the critical behavior, which will be discussed in the next subsection.

5.2.3 Experimental signature

In this section, we discuss how single skyrmion excitations can be observed in the FM state. We first introduce an approximated wave function for a single skyrmion excitation:

$$b_{\boldsymbol{k}}^{\dagger}|\mathrm{FM}\rangle \sim \frac{1}{N} \sum_{s} e^{-i\boldsymbol{k}\cdot\boldsymbol{R}_s} \psi_{\boldsymbol{R}_s}^{\dagger}|\mathrm{FM}\rangle, \tag{5.2.17}$$

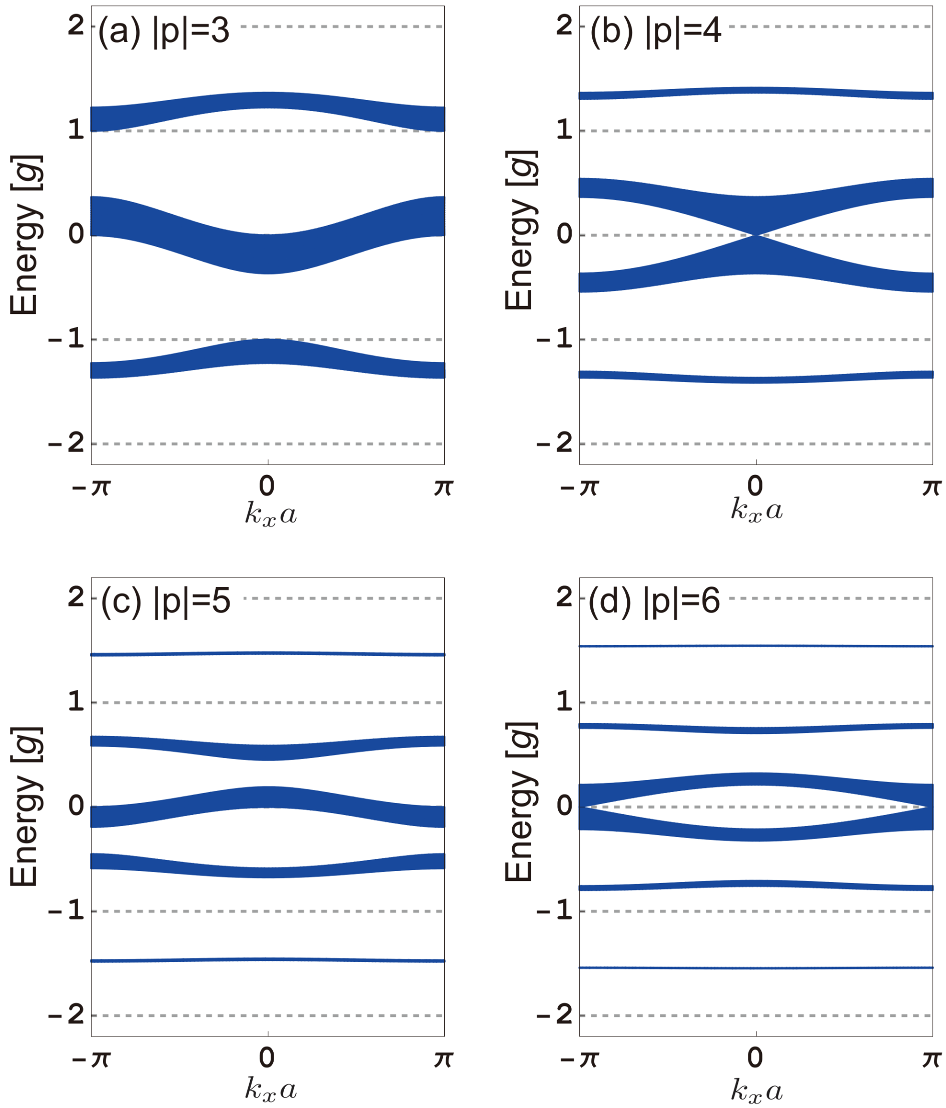

Figure 5.2: Energy spectrum of a single skyrmion excitation for (a) $|\mathrm{p}| \equiv 2S|\mathcal{N}| = 3$, (b) $|\mathrm{p}| = 4$, (c) $|\mathrm{p}| = 5$, and (d) $|\mathrm{p}| = 6$. The vertical axis represents energy in the unit of g, and the energy is measured from the energy in the continuum limit. Eigenenergies for different k_y are plotted.

where $\boldsymbol{R}_s = (a/2, a/2) + (s_x a, s_y a)$ with $s_x, s_y \in \mathbb{Z}$, $|\mathrm{FM}\rangle$ denotes a FM state, $b_{\boldsymbol{k}}$ is the operator for a skyrmion excitation, and

$$\psi^{\dagger}_{\boldsymbol{R}_s}|\mathrm{FM}\rangle = \otimes_i |\boldsymbol{n}_{sk}(\boldsymbol{r}_i - \boldsymbol{R}_s)\rangle, \tag{5.2.18}$$

is a state with a skyrmion excited at $\boldsymbol{R}_s$.

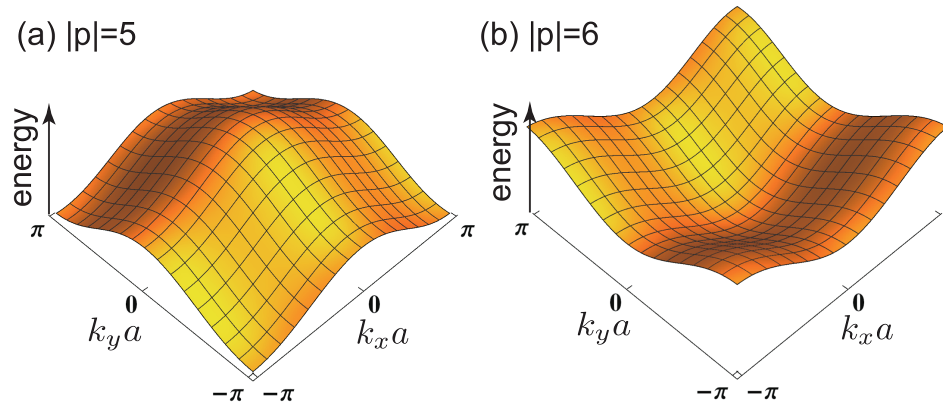

Figure 5.3: Band dispersion of the lowest bands for (a) p is odd (|p| = 5) and (b) p is even (|p| = 6).

Recall that a spin coherent state at each site can be represented by

$$|\boldsymbol{n}_i\rangle = e^{iS_z\phi}e^{iS_y\theta}e^{iS_z\chi}|S,S\rangle, \tag{5.2.19}$$

$$= \left(\cos\frac{\theta_i}{2}\right)^{2S}\sum_{m=0}^{2S}\frac{1}{m!}\left(\tan\frac{\theta_i}{2}\right)^m e^{im\phi_i}(\hat{S}_i^-)^m|S,S\rangle, \tag{5.2.20}$$

where we have chosen the gauge as $\chi = -\phi$, $\boldsymbol{n}_i = (\sin\theta_i\cos\phi_i, \sin\theta_i\sin\phi_i, \cos\theta_i)$ and $|S,S\rangle$ is the maximally polarized state of a single spin. The skyrmion configuration $\boldsymbol{n}_i = \boldsymbol{n}_{sk}(\boldsymbol{r}_i - \boldsymbol{R}_s \equiv \delta\boldsymbol{r}_i)$ can be simply represented with a polar coordinate $\delta\boldsymbol{r} = (\delta r_i, \Theta_i)$ centered at $\boldsymbol{R}_s$ (Fig. 5.4):

$$\theta_i = \theta(\delta r_i), \tag{5.2.21}$$

$$\phi_i = \Theta_i + \alpha, \tag{5.2.22}$$

where $\theta(0) = \pi$ and $\theta(\delta r \gg L_s) \sim 0$. Here we consider a configuration stabilized by the DM interaction, i.e. $\mathcal{N} = -1$ with the fixed "helicity" α.

As is clear from Eq. (5.2.20), a skyrmion state is a superposition of states with different numbers, m_{tot} of bound magnons: $m_{tot} \equiv \sum_i(S - S_i^z)$, which includes a state with $m_{tot} = 1$. This state can be captured by inelastic neutron scattering measurements, which measures the dynamical spin correlation

$$\mathrm{Im}\ \chi^{+-}(\boldsymbol{\kappa},\omega) = \mathrm{Im}\left[i\int_0^\infty dt e^{i\omega t}\langle\hat{S}_{\boldsymbol{\kappa}}^+(t)\hat{S}_{-\boldsymbol{\kappa}}^-(0)\rangle\right]. \tag{5.2.23}$$

Let us estimate the magnitude of the signal of a single skyrmion excitation:

$$\mathrm{Im}\ \chi^{+-}(\boldsymbol{\kappa},\omega) \sim \pi\sum_{\boldsymbol{k}}|\langle\mathrm{FM}|b_{\boldsymbol{k}}\hat{S}_{-\boldsymbol{\kappa}}^-|\mathrm{FM}\rangle|^2\delta(\omega - \xi_{\boldsymbol{k}}). \tag{5.2.24}$$

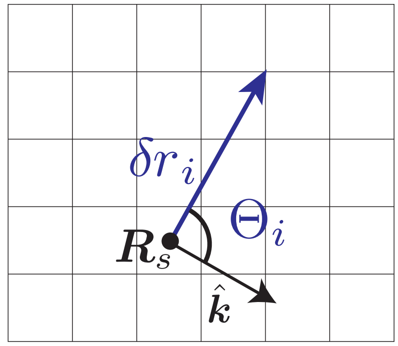

Figure 5.4: Polar coordinate for a skrymion configuration. $\boldsymbol{R}_s$ is the center of the skyrmion.

Using the explicit configuration $\boldsymbol{n}_i$ in Eqs. (5.2.21) and (5.2.22), we obtain

$$|\langle \mathrm{FM}|b_{\boldsymbol{k}}\hat{S}^{-}_{-\boldsymbol{\kappa}}|\mathrm{FM}\rangle| = \frac{S}{N}\left(\prod_{j\in A}\cos\frac{\theta(\delta r_j)}{2}\right)^{2S}\left|\sum_{i\in A}\tan\frac{\theta(\delta r_i)}{2}e^{i(Q\delta r_i\cos\Theta_i-\Theta_i)}\right|\delta_{\boldsymbol{\kappa},\boldsymbol{k}}, \tag{5.2.25}$$

where A is the region such that $\theta(\delta r_{i\in A}) \neq 0$; the region where a skyrmion spreads over. The number of sites in A is $\sim (L_s/a)^2$.

For $L_s^{-1} \ll Q \ll a^{-1}$, we can further estimate Eq. (5.2.25) with a continuous approximation

$$\mathrm{Im}\ \chi^{+-}(\boldsymbol{\kappa},\omega) \sim \frac{1}{a^2Q^2}\exp\left(-(\ln 2)S(L_s/a)^2\right)\delta(\omega-\xi_{\boldsymbol{\kappa}}), \tag{5.2.26}$$

where ξ_Q is the excitation energy of a skyrmion defined in the last section. Although the intensity remains weak, it should be distinct from the signal of a magnon; skyrmion excitations have multiple bands, and the dispersion is much smaller.

5.3 Many body phase diagram

In this section, we study the phase diagram in the presence of interactions between skyrmions (Fig. 5.5). Focusing on the lowest energy band, we consider a many body action: $\mathcal{S} = \mathcal{S}_0 + \mathcal{S}'$ with

$$\mathcal{S}_0 = \int d\tau \left[\sum_{\boldsymbol{k}} \bar{b}_{\boldsymbol{k}}(\partial_\tau + \xi_{\boldsymbol{k}})b_{\boldsymbol{k}} + \sum_{\boldsymbol{k},\boldsymbol{k}',\boldsymbol{q}} U_{\boldsymbol{k},\boldsymbol{k}',\boldsymbol{q}}\bar{b}_{\boldsymbol{k}+\boldsymbol{q}}\bar{b}_{\boldsymbol{k}'-\boldsymbol{q}}b_{\boldsymbol{k}'}b_{\boldsymbol{k}}\right]. \tag{5.3.1}$$

$b_{\boldsymbol{k}} = b_{\boldsymbol{k}}(\tau)$ and $\bar{b}_{\boldsymbol{k}} = b^*_{\boldsymbol{k}} = \bar{b}_{\boldsymbol{k}}(\tau)$ are canonical Bose operators that annihilate and create the skyrmion excitations obtained in the last section.

$$\xi_{\boldsymbol{k}} = \mathcal{E}_{0,\boldsymbol{k}} + E_0 - E_{\mathrm{FM}} \tag{5.3.2}$$

is the single particle energy of skyrmions measured from the FM energy, where E_0 is the energy of a single skyrmion in the continuum limit, and E_{FM} is the energy of a FM state. The last term is a short range repulsive interaction, which eventually leads to the crystallization of skyrmions. $\mathcal{S}'$ represents the terms that do not conserve the number of skyrmions, which are allowed due to the DM interaction; it breaks the U(1) spin rotation symmetry about the applied field, and hence violates conservation of S^z. Thus although a skyrmion possesses flipped spins in its core, its spin is not a good quantum number and cannot microscopically protect skyrmion number. The processes that changes the skyrmion number may be considered as tunneling events which can occur due to lattice scale physics [204]. In a high field with $E_0 \gg E_{FM}$, the density of skrymions is suppressed

$$\langle n_{\boldsymbol{k}} \rangle \equiv \langle \bar{b}_{\boldsymbol{k}} b_{\boldsymbol{k}} \rangle \sim 0. \tag{5.3.3}$$

In a lower field with $\xi_{\boldsymbol{k}_{\min}} \sim 0$, the density of skyrmions increases, with the first skyrmions entering being those with $\boldsymbol{k} = \boldsymbol{k}_{\min}$:

$$\langle n_{\boldsymbol{k}_{\min}} \rangle \gg 1. \tag{5.3.4}$$

The resulting quantum state is a quantum liquid of skyrmions, where skyrmions "condense" at $\boldsymbol{k} = \boldsymbol{k}_{\min}$, and they are not spatially localized. We note that this condensation differs from ideal Bose Einstein condensation since the action does not conserve skyrmion number.

To clarify the nature of the condensation, we focus on the states around the minimum of $\xi_{\boldsymbol{k}}$, and define a new field $b(\boldsymbol{r},\tau) \sim \eta(\boldsymbol{r},\tau) e^{i\boldsymbol{k}_{\min}\cdot\boldsymbol{r}}$, where $b(\boldsymbol{r},\tau)$ is the inverse Fourier transform of $b_{\boldsymbol{k}}(\tau)$, and $\eta(\boldsymbol{r})$ has small space time gradients. Then we obtain

$$\mathcal{S} \sim \int d\tau d^2 r \left[\bar{\eta}\partial_\tau \eta + r|\eta|^2 + c_0|\boldsymbol{\nabla}\eta|^2 + c_1|\eta|^4\right] + \mathcal{S}', \tag{5.3.5}$$

where $r = \xi_{\boldsymbol{k}_{\min}}$, $c_0 = \frac{1}{2}\partial^2_{k_\mu}\xi_{\boldsymbol{k}_{\min}}$, and c_1 is a constant given by the interaction.

For odd p $= 2S\mathcal{N}$, there is a continuous phase transition. Since the energy minimum is at $\boldsymbol{k}_{\min} = (\pi,\pi)$, the odd order terms of $\eta, \bar{\eta}$ are forbidden in $\mathcal{S}'$ by translational symmetry/momentum conservation:

$$\mathcal{S}' \sim \int d\tau d^2 r \left[f^{(2)}\eta\eta + (f^{(4a)}\eta\eta\eta\eta + \cdots) + \text{c.c.}\right]. \tag{5.3.6}$$

To obtain the critical theory, we define $\eta(\boldsymbol{r},\tau) = \varphi_R(\boldsymbol{r},\tau) + i\varphi_I(\boldsymbol{r},\tau)$. Up to quadratic order, the total action is given by

$$\begin{aligned}\mathcal{S} \sim \int d\tau d^2 r \Big[&-2\varphi_I(i\partial_\tau + F_1)\varphi_R + \varphi_R(r + F_0 - c_0\partial_\mu^2)\varphi_R \\ &+\varphi_I(r - F_0 - c_0\partial_\mu^2)\varphi_I\Big].\end{aligned} \tag{5.3.7}$$

We have defined $F_1 = 2\mathrm{Im} f^{(2)}$ and $F_0 = 2\mathrm{Re} f^{(2)} (> 0)$, whose sign can be arbirarily chosen by redefining η. In the critical region where the single particle energy gap of φ_I becomes small ($r - F_0 \sim 0$), we can integrate out φ_R, which has the energy gap $\sim 2F_0$. Then, the critical behavior is described by the following action:

$$\mathcal{S} \sim \int d\tau d^2 r \left(\frac{1}{2} \left((\partial_\tau \varphi_I)^2 + r' \varphi_I^2 + v(\partial_\mu \varphi_I)^2 \right) + \frac{u}{4!} \varphi_I^4 \right), \tag{5.3.8}$$

where v, u and $r' = (r + F_0)(r - F_0) - F_1^2$ are constants, and φ_I is redefined to absorb some constants. This is the standard φ^4 action describing to the Ising phase transition, e.g. in the three-dimensional ferromagnetic classical Ising model. The zero temperature transition in 2+1 space-time dimensions has quantum critical behavior in this universality class. The phase transition is described by the order parameter $\langle \varphi_I \rangle$ that breaks the symmetry $\varphi_I \to -\varphi_I$. Thus, the condensation of skyrmions is accompanied by the phase transition at B^* with the critical behavior given by Eq. (5.3.8).

On the other hand, for even p, the energy minimum is at $\boldsymbol{k}_{\min} = (0, 0)$, and we have

$$\mathcal{S}' \sim \int d\tau d^2 r \left[f^{(1)} \eta + f^{(2)} \eta \eta + \cdots + \text{c.c.} \right]. \tag{5.3.9}$$

The first order terms, $f^{(1)} \eta + f^{(1)*} \bar{\eta}$ give rise to $-h\varphi_I$ in the final action (Eq. (5.3.8)) with a constant h. It results in a crossover, which is the same as the Ising model under a magnetic field. In this case, there is no true quantum phase transition corresponding to the condensation of skyrmions. Instead, some virtual skyrmions are present in the ground state at all fields, even above the naïve condensation point. A level crossing of the physical excited state consisting of a real (not virtual) skyrmion with the ground state cannot occur due to level repulsion, which explains the absence of a condensation phase transition. However, at lower fields, a transition to a SkX state still occurs.

Next we discuss this phase transition from the quantum liquid state to the SkX phase, which occurs at the even lower field ($B = B_c$). Let us define the typical magnitude of the two-body repulsive interaction $\bar{U}(n)$, which depends on the distance between skyrmions $\sim n^{-1/2}$. The band width W of the skyrmion excitation is bounded by g, where g is estimated in Eq. (5.5.6). For $W \gg \bar{U}(n)$, the kinetic energy is dominant, so that the skyrmions have itinerant properties (quantum liquid). When the density becomes large enough such that $W \ll \bar{U}(n)$, the repulsive interaction becomes dominant, and skyrmions form a density wave, i.e. a SkX, to minimize the interaction. The density-density correlation has the Fourier expansion

$$\langle n(\boldsymbol{r}) n(\boldsymbol{0}) \rangle = \text{const.} + \operatorname{Re} \sum_i A_i e^{i \boldsymbol{\kappa}_i \cdot \boldsymbol{r}} + \cdots, \tag{5.3.10}$$

where $n(\boldsymbol{r})$ is the local density for skyrmions, and $\boldsymbol{\kappa}_i$ are incommensurate wave vectors determined by the structure of the interaction. The amplitudes A_i are order parameters for the SkX phase, which breaks lattice translational invariance. The critical field B_c is determined by the critical density n_c that satisfies $\bar{U}(n_c) \sim W$. Thus, for smaller bandwidth, the region of the quantum liquid phase becomes narrower.

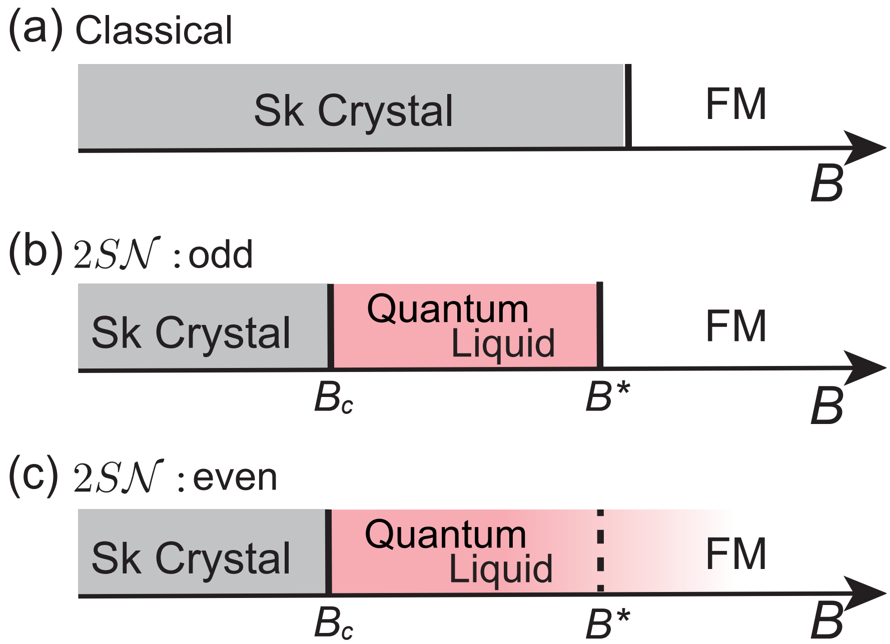

Figure 5.5: Schematic phase diagrams at zero temperature for (a) classical spins[201], (b) quantum spins with even $2S\mathcal{N}$, and (c) odd $2S\mathcal{N}$. S is the spin size and $\mathcal{N}$ is the skyrmion number of a single skyrmion. In (a), Skyrmions (Sk) are nucleated in the field induced ferromagnetic (FM) background below the critical magnetic field. In (b) and (c), the quantum liquid phase of skyrmions appears. It is connected to the FM phase via the continuous phase transition for (b) or the crossover for (c).

5.4 Summary and discussions

In this chapter, we have studied the quantum description of magnetic skyrmions in a two-dimensional chiral magnet. Such quantum mechanical properties may appear for small skyrmions, especially in the region close to a SkX phase. We have shown that a quantum liquid phase can appear as an intermediate phase.

A basic result is that the well-known classical Magnus force dynamics of skyrmions,[161, 162, 163] extends to the quantum level and dominates the band structure of skyrmion states, making them quantitatively very different from the usual magnon band(s) of a ferromagnet. While this is not surprising from a semi-classical point of view, it may raise flags for a many-body quantum physicist. The skyrmion is a local excitation (i.e. it does not affect spins far from its core) of a ferromagnetic state, which has only short-range entanglement: it is essentially a product state of up spins. The microscopic spin Hamiltonian for a chiral magnet is local and the spins are neutral and do not transform under any gauge symmetry. In general, we expect that a short-range entangled state of such a Hamiltonian would possess only neutral quasiparticles which could not experience any orbital magnetic fields (i.e. they do not couple to any gauge fields). More formally, a charged particle in a magnetic field transforms under translations differently from a neutral particle. The latter transforms under simple coordinate transformations only, while for the former particle, a coordinate transformation must be accompanied by a gauge transformation as the vector potential is not translationally invariant: such transformations are known as magnetic translations. It would be exceedingly strange (we believe impossible) for a skyrmion in a ferromagnet to truly exhibit such a gauge structure. In our calculations here we found a resolution to this dilemma. Specifically, taking into account even weak lattice effects, which are necessary for a finite quantum theory, the effective number of flux quanta per unit cell is found to be integer. Under this condition magnetic and ordinary translations coincide. Consequently, the bands of skyrmion states are not *qualitatively* distinct from those of magnons, although we find that quantitatively they are very different and should be easily differentiated in experiment.

In our study, we have not included a mass term $\sim (\dot{X}^2 + \dot{Y}^2)$ in the effective action. Microscopically it can arise from coupling to some gapped modes, such as the deformation of a skyrmion. [83] The mass term makes skyrmions form the Landau bands, which are flat without periodic potentials. Therefore the interaction between skyrmions immediately force them to form a crystal; this is consistent with the classical models. However, once the cosine potential is considered, it recovers the subbands structure with dispersion. [205, 206] From this point of view, our study corresponds to projection onto the lowest landau level.

Regarding experiments, hexagonal Fe film on Ir (111) surface [197] and thin films of $Fe_{0.5}Co_{0.5}Si$ and MnSi grown along $\langle 111 \rangle$ direction have lattice structures effectively modeled by triangular lattices. We, however, note that the triangular lattice also gives qualitatively same results; the band splits into $|\mathrm{p}| = 2S|\mathcal{N}|$ subbands, and a crossover to the quantum phase for even p, and a quantum phase transition for odd p.

Finally, we comment on skyrmions in frustrated spin systems. Theoretically it has been shown that SkX phases appear on a triangular lattice with frustrated interactions, which preserves spin U(1) symmetry along the field[73, 74, 198]. We showed that the quantum states of skyrmions in chiral magnets have crystal momentum as a good quantum number (Eq. (5.2.16)). On the other hand, skyrmions in frustrated magnets are have additional quantum numbers: the number of bound magnons m_{tot} and the discrete angular momentum related to the helicity of a skyrmion. The magnon number m_{tot} is related to the size of a classical configuration of a skyrmion. It would be interesting to investigate the quantum phase and critical theory for such skyrmions. We leave the detailed discussion for future work.

5.5 Details

In this section, we present the derivation and more detailed discussion on this chapter.

5.5.1 Derivation of Eq. (5.2.4)

We first show that the periodic potential in the effective action (Eq. (5.2.4)) is obtained from $H(\{\boldsymbol{n}_i\})$ in the original action (Eq. (5.2.3)). Let us define the "energy density" $h(\boldsymbol{r})$ as

$$\mathrm{H}(\{\boldsymbol{n}_i\}) \equiv a^2 \sum_i h\left(\boldsymbol{r}_i - \boldsymbol{R}\right), \tag{5.5.1}$$

$$h(\boldsymbol{r}-\boldsymbol{R}) = \frac{JS^2}{a^2} - \frac{JS^2}{2}\partial_\mu \boldsymbol{n}\cdot\partial_\mu \boldsymbol{n} + \frac{DS^2}{a}\sum_{\mu=x,y}\hat{\boldsymbol{e}}_\mu\cdot(\boldsymbol{n}\times\partial_\mu\boldsymbol{n}) - \frac{BS}{a^2}n^z - \frac{KS\left(S-\frac{1}{2}\right)}{a^2}(n^z)^2 + \mathcal{O}\left(\frac{Ja^2}{L_s^4}\right), \tag{5.5.2}$$

where $\boldsymbol{r}_i = (i_x a, i_y a)$ denotes the position of a site i, and $\boldsymbol{n}$ abbreviates $\boldsymbol{n}_{sk}(\boldsymbol{r}-\boldsymbol{R})$.

We consider skyrmions whose energy density $h(\boldsymbol{r})$ has the maximum at the center $\boldsymbol{r}=\boldsymbol{0}$, the center of the skyrmion. The characteristic length of $h(\boldsymbol{r})$ is given by the skyrmion configuration as $L_s(\gg a)$. We then expand the discrete summation with the Poisson summation formula $\sum_i \delta^{(2)}(\boldsymbol{r}-\boldsymbol{r}_i) = a^{-2}\sum_{l_x,l_y} e^{-\frac{2\pi i}{a}\boldsymbol{l}\cdot\boldsymbol{r}}$ as

$$\mathrm{H}(\{\boldsymbol{n}_i\}) \sim \int d^2r h(\boldsymbol{r}-\boldsymbol{R}) + 2\int d\boldsymbol{r}\left(\cos\left(\frac{2\pi x}{a}\right)+\cos\left(\frac{2\pi y}{a}\right)\right)h(\boldsymbol{r}-\boldsymbol{R}), \tag{5.5.3}$$

$$\sim E_0 + g\left(\cos\left(\frac{2\pi X}{a}\right)+\cos\left(\frac{2\pi Y}{a}\right)\right), \tag{5.5.4}$$

E_0 is the energy in the continuous limit, which is constant for $\boldsymbol{R}$. The second term in Eq. (5.5.3) gives the periodic potential for $\boldsymbol{R}$ with the coefficient

$$g \sim \frac{8\pi\ h(\boldsymbol{0})^2}{|\partial_\mu^2 h(\boldsymbol{0})|}\exp\left(-\frac{4\pi^2 h(\boldsymbol{0})}{a^2|\partial_\mu^2 h(\boldsymbol{0})|}\right), \tag{5.5.5}$$

$$= \frac{2C}{\pi}L_s^2 h(\boldsymbol{0})\exp\left(-C\frac{L_s^2}{a^2}\right). \tag{5.5.6}$$

Here we have assumed $h(\boldsymbol{r})$ has rotational symmetry, and expanded $h(\boldsymbol{r}) = \exp(\log h(\boldsymbol{r})) \sim h(0)\exp\left(\frac{1}{2h(0)}(x^2\partial_x^2 h(0) + y^2\partial_y^2 h(0))\right)$. We define a dimensionless constant

$$C \equiv 4\pi^2 h(\boldsymbol{0})/(L_s^2|\partial_\mu^2 h(\boldsymbol{0})|) \sim \mathcal{O}(1) \tag{5.5.7}$$

. The higher harmonics, which are dropped in Eq. (5.5.3), gives different periodic potentials, but their strength is higher order of $\exp\left(-CL_s^2/a^2\right)$. In Eq. (5.5.6), we denote $h(\boldsymbol{0})$ by ε.

Next we discuss the Berry phase terms. As in Eq. (5.5.3), we can expand the discrete summation over sites. To the lowest order, we obtain

$$iS\int d\tau \sum_i \dot{\boldsymbol{n}}_i \cdot \boldsymbol{A}(\boldsymbol{n}_i) \sim \frac{iS}{a^2}\int d\tau \int d\boldsymbol{r}\dot{\boldsymbol{n}} \cdot \boldsymbol{A}(\boldsymbol{n}), \tag{5.5.8}$$

$$= \frac{2\pi iS\mathcal{N}}{a^2}\int d\tau (Y\dot{X} - X\dot{Y}), \tag{5.5.9}$$

up to the surface terms in the time integral [161]. The rest of the terms in the harmonic expansion are smaller than Eq. (5.5.4) because of the time derivative, and thus we take only the lowest order, i.e. the continuous limit.

5.5.2 Derivation of Eq. (5.3.8)

We show the derivation of the effective action in the critical region for even $2S\mathcal{N}$ and odd $2S\mathcal{N}$. We consider the action up to quadratic order

$$\mathcal{S} \sim \int d\tau d\boldsymbol{r} \left[\bar{\eta}\partial_\tau \eta + r|\eta|^2 + c_0|\boldsymbol{\nabla}\eta|^2 + f^{(1)}\eta + f^{(1)*}\bar{\eta} + f^{(2)}\eta\eta + f^{(2)*}\bar{\eta}\;\bar{\eta}\right], \tag{5.5.10}$$

Note that $f^{(1)} = 0$ for odd $2S\mathcal{N}$. We now define $D_0 = 2\mathrm{Re}f^{(1)}$ and $D_1 = 2\mathrm{Im}f^{(1)}$, $F_0 = 2\mathrm{Re}f^{(2)} > 0$, $F_1 = 2\mathrm{Im}f^{(2)}$, and $\eta(\boldsymbol{r},\tau) = \varphi_R(\boldsymbol{r},\tau) + i\varphi_I(\boldsymbol{r},\tau)$, and obtain

$$\begin{aligned}\mathcal{S} = \int d\tau d\boldsymbol{r} \Big[&-2i\varphi_I\partial_\tau\varphi_R + \varphi_R(r - c_0\partial_\mu^2 + F_0)\varphi_R \\ &+\varphi_I(r - c_0\partial_\mu^2 - F_0)\varphi_I - 2F_1\varphi_R\varphi_I + D_0\varphi_R - D_1\varphi_I\Big].\end{aligned} \tag{5.5.11}$$

For $r \sim F_0$, we integrate out φ_R, and obtain

$$\mathcal{S} = \int d\boldsymbol{r} d\tau \left(\frac{1}{2}\left((\partial_\tau\varphi_I)^2 + r'\varphi_I^2 + v(\partial_\mu\varphi_I)^2\right) - h\varphi_I + \frac{u}{4!}\varphi_I^4\right), \tag{5.5.12}$$

where we redefine $\varphi \to \sqrt{\frac{2}{r+F_0}}\varphi_I$, and

$$r' = (r + F_0)(r - F_0) - F_1^2, \tag{5.5.13}$$

$$v = c_0\left(r + F_0 + \frac{F_1^2}{r + F_0}\right), \tag{5.5.14}$$

$$h = \sqrt{\frac{r + F_0}{2}}\left(D_1 - \frac{F_1 D_0}{r + F_0}\right). \tag{5.5.15}$$

We have recovered the interaction term in Eq. (5.5.12). For odd $2S\mathcal{N}$, we note that $h = 0$.

Chapter 6

Conclusion

In this thesis, we have studied physics emerged from the interplay between superconductivity and spin textures. Motivated by spintronics applications and considerable interest in topological phenomena, we have proposed spin-torques, control of magnetization, and topological states intertwined with superconductivity.

In Chap. 2, we have microscopically derived the spin-transfer torque induced by triplet supercurrents. Spin-triplet correlations change the properties of the spin-transfer torques from one in conventional systems, which is demonstrated in domainwall manipulation. With a triplet supercurrent, oscillatory motion of a domain wall can be avoided, and the threshold current density to drive its motion becomes zero in the absence of extrinsic pinning potentials. Our results found that a triplet correlation qualitatively changes the spin-transfer process, and efficient manipulation of a magnetic domain wall can be realized.

In Chap. 3, we have studied a spin torque induced by a singlet supercurrent in a cubic chiral magnet with a proximity-induced s-wave superconductivity. With the numerical and analytical calculation, we have derived the spin torque induced by a supercurrent. We have shown how it acts on magnetic skyrmions. Furthermore, we have also pointed out the existence of a pair of Weyl points in the BdG spectrum. The positions of the Weyl points are determined by the magnetization, and the resulting effective electromagnetic field may give rise to novel phenomena in spintronics. The tilt of the cones can also be changed by the magnitude of the spin-orbit coupling, and type-II Weyl points can be realized. We believe that the nontrivial band topology of Bogoliubov quasiparticles provides a new perspective in superconducting spintronics.

In Chap. 4, we have proposed a way to induce and control noncollinear spin textures by utilizing a supercurrent, in a correlated metal in proximity to a singlet superconductor. We showed that the proximity effect of supercurrents can lead to phase transitions from a paramagnetic state to noncollinear magnetic phases. Furthermore, we demonstrate that different types of noncollinear magnetic orders, such as helical and vortexlike orders, can be switched by the direction of the supercurrent. Our results open up the possibilities to use superconducting correlations as a “harness” for spin textures.

In Chap. 5, we have studied the quantum description of magnetic skyrmions in a two-dimensional chiral magnet. Such quantum mechanical properties may appear for small skyrmions. We have shown that condensation of the skyrmions can give rise to an intermediate phase between the skyrmion crystal and ferromagnet: a quantum liquid, in which skyrmions are not spatially localized. We also found that the critical behavior depends on the spin size S and the topological number of the skyrmion. We believe that, combined with superconductivity, these effects will further give rise to versatile phenomena.

Bibliography

[1] B. Kastening, D. K. Morr, D. Manske, and K. Bennemann, Phys. Rev. Lett. **96**, 047009 (2006).

[2] T. Yokoyama, Phys. Rev. B **84**, 132504 (2011).

[3] P. M. R. Brydon, D. Manske, and M. Sigrist, J. Phys. Soc. Jpn **77**, 103714 (2008).

[4] P. M. R. Brydon, Phys. Rev. B **80**, 224520 (2009).

[5] P. M. R. Brydon, Y. Asano, and C. Timm, Phys. Rev. B **83**, 180504 (2011).

[6] T. Yokoyama, Phys. Rev. B **92**, 174513 (2015).

[7] A. J. Leggett, Rev. Mod. Phys. **47**, 331 (1975).

[8] A. P. Mackenzie and Y. Maeno, Rev. Mod. Phys. **75**, 657 (2003).

[9] G. R. Stewart, Z. Fisk, J. O. Willis, and J. L. Smith, Phys. Rev. Lett. **52**, 679 (1984).

[10] N. T. Huy, A. Gasparini, D. E. De Nijs, Y. Huang, J. C. Klaasse, T. Gortenmulder, A. De Visser, A. Hamann, T. Görlach, and H. V. Löhneysen, Phys. Rev. Lett. **99**, 067006 (2007).

[11] M. S. Anwar, S. R. Lee, R. Ishiguro, Y. Sugimoto, Y. Tano, S. J. Kang, Y. J. Shin, S. Yonezawa, D. Manske, H. Takayanagi, T. W. Noh, and Y. Maeno, Nat. Commun. **7**, 13220 (2016).

[12] E. Bauer, G. Hilscher, H. Michor, C. Paul, E. W. Scheidt, A. Gribanov, Y. Seropegin, H. Noël, M. Sigrist, and P. Rogl, Phys. Rev. Lett. **92**, 027003 (2004).

[13] N. Kimura, K. Ito, K. Saitoh, Y. Umeda, H. Aoki, and T. Terashima, Phys. Rev. Lett. **95**, 247004 (2005).

[14] P. A. Frigeri, D. F. Agterberg, A. Koga, and M. Sigrist, Phys. Rev. Lett. **92**, 097001 (2004).

[15] J. Alicea, Rep. Prog. Phys. **75**, 076501 (2012).

[16] V. Edelstein, Solid State Commun. **73**, 233 (1990).

[17] N. Nagaosa, J. Sinova, S. Onoda, A. H. MacDonald, and N. P. Ong, Rev. Mod. Phys. **82**, 1539 (2010).

[18] F. S. Bergeret, A. F. Volkov, and K. B. Efetov, Rev. Mod. Phys. **77**, 1321 (2005).

[19] F. S. Bergeret and I. V. Tokatly, Phys. Rev. Lett. **110**, 117003 (2013).

[20] F. S. Bergeret and I. V. Tokatly, Phys. Rev. B **89**, 134517 (2014).

[21] R. S. Keizer, S. T. B. Goennenwein, T. M. Klapwijk, G. Miao, G. Xiao, and A. Gupta, Nature **439**, 825 (2006).

[22] M. S. Anwar, F. Czeschka, M. Hesselberth, M. Porcu, and J. Aarts, Phys. Rev. B **82**, 100501 (2010).

[23] T. S. Khaire, M. A. Khasawneh, W. P. Pratt, and N. O. Birge, Phys. Rev. Lett. **104**, 137002 (2010).

[24] J. W. A. Robinson, J. Witt, and M. Blamire, Science **329**, 59 (2010).

[25] D. Thouless, M. Kohmoto, M. Nightingale, and M. den Nijs, Phys. Rev. Lett. **49**, 405 (1982).

[26] M. Kohmoto, Ann. Phys. (N. Y). **160**, 343 (1985).

[27] C. L. Kane and E. J. Mele, Phys. Rev. Lett. **95**, 226801 (2005).

[28] C. L. Kane and E. J. Mele, Phys. Rev. Lett. **95**, 146802 (2005).

[29] A. Schnyder, S. Ryu, A. Furusaki, and A. Ludwig, Phys. Rev. B **78**, 195125 (2008).

[30] A. Kitaev, AIP Conf. Proc. **1134**, 22 (2009).

[31] G. E. Volovik, *The universe in a helium droplet* (Oxford University Press, Oxford, 2003).

[32] N. Read and D. Green, Phys. Rev. B **61**, 10267 (2000).

[33] M. Sato and S. Fujimoto, J. Phys. Soc. Jpn **85**, 072001 (2016).

[34] S. Murakami, New J. Phys. **9**, 356 (2007).

[35] X. Wan, A. M. Turner, A. Vishwanath, and S. Y. Savrasov, Phys. Rev. B **83**, 205101 (2011).

[36] A. A. Burkov and L. Balents, Phys. Rev. Lett. **107**, 127205 (2011).

[37] T. Mizushima, Y. Tsutsumi, M. Sato, and K. Machida, J. Phys. Condens. Matter **27**, 113203 (2015).

[38] C. Nayak, S. H. Simon, A. Stern, and M. Freedman, Rev. Mod. Phys. **80**, 1083 (2008).

[39] A. Y. Kitaev, Phys. -Usp. **44**, 131 (2001).

[40] R. M. Lutchyn, J. D. Sau, and S. Das Sarma, Phys. Rev. Lett. **105**, 077001 (2010).

[41] Y. Oreg, G. Refael, and F. Von Oppen, Phys. Rev. Lett. **105**, 177002 (2010).

[42] T.-P. Choy, J. M. Edge, A. R. Akhmerov, and C. W. J. Beenakker, Phys. Rev. B **84**, 195442 (2011).

[43] S. Nadj-Perge, I. K. Drozdov, B. A. Bernevig, and A. Yazdani, Phys. Rev. B **88**, 020407 (2013).

[44] J. Klinovaja, P. Stano, A. Yazdani, and D. Loss, Phys. Rev. Lett. **111**, 186805 (2013).

[45] M. M. Vazifeh and M. Franz, Phys. Rev. Lett. **111**, 206802 (2013).

[46] B. Braunecker and P. Simon, Phys. Rev. Lett. **111**, 147202 (2013).

[47] V. Mourik, K. Zuo, S. M. Frolov, S. R. Plissard, E. P. A. M. Bakkers, and L. P. Kouwenhoven, Science **336**, 1003 (2012).

[48] A. Das, Y. Ronen, Y. Most, Y. Oreg, M. Heiblum, and H. Shtrikman, Nat. Phys. **8**, 887 (2012).

[49] S. Nadj-perge, I. K. Drozdov, J. Li, H. Chen, and S. Jeon, Science **346**, 602 (2014).

[50] L. Fu and C. L. Kane, Phys. Rev. Lett. **100**, 096407 (2008).

[51] M. Sato, Y. Takahashi, and S. Fujimoto, Phys. Rev. Lett. **103**, 020401 (2009).

[52] S. Nakosai, Y. Tanaka, and N. Nagaosa, Phys. Rev. B **88**, 180503 (2013).

[53] W. Chen and A. P. Schnyder, Phys. Rev. B **92**, 214502 (2015).

[54] J. Li, T. Neupert, Z. Wang, A. H. MacDonald, A. Yazdani, and B. A. Bernevig, Nat. Commun. **7**, 12297 (2016).

[55] T. Meng and L. Balents, Phys. Rev. B **86**, 054504 (2012).

[56] Y. Kasahara, T. Iwasawa, H. Shishido, T. Shibauchi, K. Behnia, Y. Haga, T. D. Matsuda, Y. Onuki, M. Sigrist, and Y. Matsuda, Phys. Rev. Lett. **99**, 116402 (2007).

[57] G. Toulouse and M. Kléman, J. Phys. Lettres **37**, 149 (1976).

[58] N. Manton and P. Sutcliffe, *Topological Solitons* (Cambridge University Press, New York, 2004).

[59] S. S. P. Parkin, M. Hayashi, and L. Thomas, Science **320**, 190 (2008).

[60] P. Ao and D. J. Thouless, Phys. Rev. Lett. **70**, 2158 (1993).

[61] J. Zang, M. Mostovoy, J. H. Han, and N. Nagaosa, Phys. Rev. Lett. **107**, 136804 (2011).

[62] K. Everschor, M. Garst, B. Binz, F. Jonietz, S. Mühlbauer, C. Pfleiderer, and A. Rosch, Phys. Rev. B **86**, 054432 (2012).

[63] A. Neubauer, C. Pfleiderer, B. Binz, A. Rosch, R. Ritz, P. Niklowitz, and P. Böni, Phys. Rev. Lett. **102**, 186602 (2009).

[64] M. Lee, W. Kang, Y. Onose, Y. Tokura, and N. P. Ong, Phys. Rev. Lett. **102**, 1 (2009), arXiv:0811.3146 .

[65] S. Mühlbauer, B. Binz, F. Jonietz, C. Pfleiderer, A. Rosch, A. Neubauer, R. Georgii, and P. Böni, Science **323**, 915 (2009).

[66] W. Münzer, A. Neubauer, T. Adams, S. Mühlbauer, C. Franz, F. Jonietz, R. Georgii, P. Böni, B. Pedersen, M. Schmidt, A. Rosch, and C. Pfleiderer, Phys. Rev. B **81**, 041203 (2010).

[67] X. Z. Yu, Y. Onose, N. Kanazawa, J. H. Park, J. H. Han, Y. Matsui, N. Nagaosa, and Y. Tokura, Nature **465**, 901 (2010).

[68] M. Uchida, N. Nagaosa, J. P. He, Y. Kaneko, S. Iguchi, Y. Matsui, and Y. Tokura, Phys. Rev. B **77**, 184402 (2008).

[69] X. Z. Yu, N. Kanazawa, Y. Onose, K. Kimoto, W. Z. Zhang, S. Ishiwata, Y. Matsui, and Y. Tokura, Nat. Mater. **10**, 106 (2011).

[70] K. Shibata, X. Z. Yu, T. Hara, D. Morikawa, N. Kanazawa, K. Kimoto, S. Ishiwata, Y. Matsui, and Y. Tokura, Nat. Nanotechnol. **8**, 723 (2013).

[71] T. Adams, A. Chacon, M. Wagner, A. Bauer, G. Brandl, B. Pedersen, H. Berger, P. Lemmens, and C. Pfleiderer, Phys. Rev. Lett. **108**, 237204 (2012).

[72] S. Seki, X. Z. Yu, S. Ishiwata, and Y. Tokura, Science **336**, 198 (2012).

[73] T. Okubo, S. Chung, and H. Kawamura, Phys. Rev. Lett. **108**, 017206 (2012).

[74] A. O. Leonov and M. Mostovoy, Nat. Commun. **6**, 8275 (2015).

[75] R. Ozawa, S. Hayami, and Y. Motome, Phys. Rev. Lett. **118**, 147205 (2017).

[76] D. F. Agterberg and S. Yunoki, Phys. Rev. B **62**, 13816 (2000).

[77] S. Hayami and Y. Motome, Phys. Rev. B **90**, 060402 (2014).

[78] G. W. Chern and C. D. Batista, Phys. Rev. Lett. **109**, 156801 (2012).

[79] I. Martin and C. D. Batista, Phys. Rev. Lett. **101**, 156402 (2008).

[80] H. Chen, Q. Niu, and A. H. Macdonald, Phys. Rev. Lett. **112**, 017205 (2014).

[81] A. A. Thiele, Phys. Rev. Lett. **30**, 230 (1973).

[82] O. A. Tretiakov, D. Clarke, G. W. Chern, Y. B. Bazaliy, and O. Tchernyshyov, Phys. Rev. Lett. **100**, 127204 (2008).

[83] I. Makhfudz, B. Krüger, and O. Tchernyshyov, Phys. Rev. Lett. **109**, 217201 (2012).

[84] G. S. D. Beach, C. Nistor, C. Knutson, M. Tsoi, and J. L. Erskine, Nat. Mater. **4**, 741 (2005).

[85] J. Slonczewski, J. Magn. Magn. Mater. **159**, L1 (1996).

[86] L. Berger, Phys. Rev. B **54**, 9353 (1996).

[87] J. Katine, F. Albert, R. Buhrman, E. Myers, and D. Ralph, Phys. Rev. Lett. **84**, 3149 (2000).

[88] M. Kläui, C. A. F. Vaz, J. A. C. Bland, W. Wernsdorfer, G. Faini, E. Cambril, and L. J. Heyderman, Appl. Phys. Lett. **83**, 105 (2003).

[89] J. Grollier, P. Boulenc, V. Cros, A. Hamzić, A. Vaurès, A. Fert, and G. Faini, J. Appl. Phys. **95**, 6777 (2004).

[90] C. K. Lim, T. Devolder, C. Chappert, J. Grollier, V. Cros, A. Vaurès, A. Fert, and G. Faini, Appl. Phys. Lett. **84**, 2820 (2004).

[91] A. Yamaguchi, T. Ono, S. Nasu, K. Miyake, K. Mibu, and T. Shinjo, Phys. Rev. Lett. **92**, 077205 (2004).

[92] P. M. Haney, R. A. Duine, A. S. Núñez, and A. H. MacDonald, J. Magn. Magn. Mater. **320**, 1300 (2008).

[93] G. Tatara, H. Kohno, and J. Shibata, Phys. Rep. **468**, 213 (2008).

[94] Y. Tserkovnyak, A. Brataas, and G. E. W. Bauer, J. Magn. Magn. Mater. **320**, 1282 (2008).

[95] S. Zhang and Z. Li, Phys. Rev. Lett. **93**, 127204 (2004).

[96] J. Xiao, A. Zangwill, and M. D. Stiles, Phys. Rev. B **73**, 054428 (2006).

[97] A. Thiaville, Y. Nakatani, J. Miltat, and Y. Suzuki, Europhys. Lett. **69**, 990 (2005).

[98] A. Chernyshov, M. Overby, X. Liu, J. K. Furdyna, Y. Lyanda-Geller, and L. P. Rokhinson, Nat. Phys. **5**, 656 (2008).

[99] A. Manchon and S. Zhang, Phys. Rev. B **78**, 212405 (2008).

[100] I. Garate and A. H. MacDonald, Phys. Rev. B **80**, 134403 (2009).

[101] I. M. Miron, G. Gaudin, S. Auffret, B. Rodmacq, A. Schuhl, S. Pizzini, J. Vogel, and P. Gambardella, Nat. Mater. **9**, 230 (2010).

[102] L. Liu, O. J. Lee, T. J. Gudmundsen, D. C. Ralph, and R. A. Buhrman, Phys. Rev. Lett. **109**, 096602 (2012).

[103] L. Levitov, Y. Nazarov, and G. Eliashberg, Zh. Eksp. Teor. Fiz. **88**, 229 (1985).

[104] S. Fujimoto and S. K. Yip, *Chapter 8 in Non-centrosymmetric Superconductors*, edited by E. B. Sigrist and M. (Springer-Verlag, Berlin, 2012).

[105] V. M. Edelstein, Sov. Phys. JETP **68**, 1244 (1989).

[106] H. Kurebayashi, J. Sinova, D. Fang, A. C. Irvine, T. D. Skinner, J. Wunderlich, V. Novák, R. P. Campion, B. L. Gallagher, E. K. Vehstedt, L. P. Zârbo, K. Výborný, A. J. Ferguson, and T. Jungwirth, Nat. Nanotechnol. **9**, 211 (2014).

[107] J. Linder and J. W. A. Robinson, Nat. Phys. **11**, 307 (2015).

[108] M. Eschrig, Rep. Prog. Phys. **78**, 104501 (2015).

[109] H. Yang, S.-H. Yang, S. Takahashi, S. Maekawa, and S. S. P. Parkin, Nat. Mater. **9**, 586 (2010).

[110] C. H. L. Quay, D. Chevallier, C. Bena, and M. Aprili, Nat. Phys. **9**, 84 (2013).

[111] F. Hubler, M. J. Wolf, D. Beckmann, and H. Lohneysen, Phys Rev. B **109**, 207001 (2012).

[112] A. I. Buzdin, A. V. Vedyayev, and N. V. Ryzhanova, Europhys. Lett. **48**, 686 (1999).

[113] L. R. Tagirov, Phys. Rev. Lett. **83**, 2058 (1999).

[114] P. V. Leksin, N. N. Garif'Yanov, I. A. Garifullin, Y. V. Fominov, J. Schumann, Y. Krupskaya, V. Kataev, O. G. Schmidt, and B. Büchner, Phys. Rev. Lett. **109**, 057005 (2012).

[115] B. Li, N. Roschewsky, B. A. Assaf, M. Eich, M. Epstein-Martin, D. Heiman, M. Münzenberg, and J. S. Moodera, Phys. Rev. Lett. **110**, 097001 (2013).

[116] X. Waintal and P. W. Brouwer, Phys. Rev. B **65**, 054407 (2002).

[117] Y. Tserkovnyak and A. Brataas, Phys. Rev. B **65**, 94517 (2002).

[118] E. Zhao and J. A. Sauls, Phys. Rev. B **78**, 174511 (2008).

[119] V. Braude and Y. M. Blanter, Phys. Rev. Lett. **100**, 207001 (2008).

[120] F. Konschelle and A. Buzdin, Phys. Rev. Lett. **102**, 017001 (2009).

[121] J. Linder and T. Yokoyama, Phys. Rev. B **83**, 012501 (2011).

[122] J. Linder, A. Brataas, Z. Shomali, and M. Zareyan, Phys. Rev. Lett. **109**, 237206 (2012).

[123] A. Yamaguchi, K. Yano, H. Tanigawa, S. Kasai, and T. Ono, Jpn. J. Appl. Phys. **45**, 3850 (2006).

[124] V. A. Oboznov, V. V. Bol'ginov, A. K. Feofanov, V. V. Ryazanov, and A. I. Buzdin, Phys. Rev. Lett. **96**, 197003 (2006).

[125] L. Berger, Phys. Rev. B **33**, 1572 (1986).

[126] G. Volovik, H. Search, C. Journals, A. Contact, M. Iopscience, S. S. Phys, and I. P. Address, J. Phys. C Solid State Phys. **83**, L83 (1987).

[127] S. E. Barnes and S. Maekawa, Phys. Rev. Lett. **98**, 246601 (2007).

[128] R. A. Duine, Phys. Rev. B **79**, 014407 (2009).

[129] M. Z. Hasan and C. L. Kane, Rev. Mod. Phys. **82**, 3045 (2010).

[130] X. L. Qi and S. C. Zhang, Rev. Mod. Phys. **83**, 1057 (2011).

[131] G. Xu, H. Weng, Z. Wang, X. Dai, and Z. Fang, Phys. Rev. Lett. **107**, 186806 (2011).

[132] K. Y. Yang, Y. M. Lu, and Y. Ran, Phys. Rev. B **84**, 075129 (2011).

[133] G. B. Halász and L. Balents, Phys. Rev. B **85**, 035103 (2012).

[134] W. Witczak-Krempa and Y. B. Kim, Phys. Rev. B **85**, 045124 (2012).

[135] P. Hosur, S. A. Parameswaran, and A. Vishwanath, Phys. Rev. Lett. **108**, 046602 (2012).

[136] A. A. Zyuzin and A. A. Burkov, Phys. Rev. B **86**, 115133 (2012).

[137] V. Aji, Phys. Rev. B **85**, 241101 (2012).

[138] D. T. Son and N. Yamamoto, Phys. Rev. Lett. **109**, 181602 (2012).

[139] C.-X. Liu, P. Ye, and X.-L. Qi, Phys. Rev. B **87**, 235306 (2013).

[140] S. Y. Xu, I. Belopolski, N. Alidoust, M. Neupane, G. Bian, C. Zhang, R. Sankar, G. Chang, Z. Yuan, C. C. Lee, S. M. Huang, H. Zheng, J. Ma, D. S. Sanchez, B. K. Wang, A. Bansil, F. Chou, P. P. Shibayev, H. Lin, S. Jia, and M. Z. Hasan, Science **349**, 613 (2015).

[141] B. Q. Lv, H. M. Weng, B. B. Fu, X. P. Wang, H. Miao, J. Ma, P. Richard, X. C. Huang, L. X. Zhao, G. F. Chen, Z. Fang, X. Dai, T. Qian, and H. Ding, Phys. Rev. X **5**, 031013 (2015).

[142] L. X. Yang, Z. K. Liu, Y. Sun, H. Peng, H. F. Yang, T. Zhang, B. Zhou, Y. Zhang, Y. F. Guo, M. Rahn, D. Prabhakaran, Z. Hussain, S. K. Mo, C. Felser, B. Yan, and Y. L. Chen, Nat. Phys. **11**, 728 (2015).

[143] M. Hirschberger, S. Kushwaha, Z. Wang, Q. Gibson, S. Liang, C. A. Belvin, B. A. Bernevig, R. J. Cava, and N. P. Ong, Nat. Mater. **15**, 1161 (2016).

[144] H. Yang, Y. Sun, Y. Zhang, W.-J. Shi, S. S. P. Parkin, and B. Yan, New J. Phys. **19**, 015008 (2017).

[145] M. N. Ali, J. Xiong, S. Flynn, J. Tao, Q. D. Gibson, L. M. Schoop, T. Liang, N. Haldolaarachchige, M. Hirschberger, N. P. Ong, and R. J. Cava, Nature **514**, 205 (2014).

[146] A. A. Soluyanov, D. Gresch, Z. Wang, Q. Wu, M. Troyer, X. Dai, and B. A. Bernevig, Nature **527**, 495 (2015).

[147] Y. Wu, D. Mou, N. H. Jo, K. Sun, L. Huang, S. L. Bud'Ko, P. C. Canfield, and A. Kaminski, Phys. Rev. B **94**, 121113(R) (2016).

[148] L. Huang, T. M. McCormick, M. Ochi, Z. Zhao, M.-T. Suzuki, R. Arita, Y. Wu, D. Mou, H. Cao, J. Yan, N. Trivedi, and A. Kaminski, Nat. Mater. **15**, 1155 (2016).

[149] K. Deng, G. Wan, P. Deng, K. Zhang, S. Ding, E. Wang, M. Yan, H. Huang, H. Zhang, Z. Xu, J. Denlinger, A. Fedorov, H. Yang, W. Duan, H. Yao, Y. Wu, y. S. Fan, H. Zhang, X. Chen, and S. Zhou, arXiv:1603.08508 .

[150] S.-Y. Xu, N. Alidoust, G. Chang, H. Lu, B. Singh, I. Belopolski, D. S. Sanchez, X. Zhang, G. Bian, H. Zheng, M.-A. Husanu, Y. Bian, S.-M. Huang, C.-H. Hsu, T.-R. Chang, H.-T. Jeng, A. Bansil, T. Neupert, V. N. Strocov, H. Lin, S. Jia, and M. Z. Hasan, Sci. Adv. **3**, e1603266 (2017).

[151] Y. Xu, F. Zhang, and C. Zhang, Phys. Rev. Lett. **115**, 265304 (2015).

[152] Z. M. Yu, Y. Yao, and S. A. Yang, Phys. Rev. Lett. **117**, 077202 (2016).

[153] G. E. Volovik and K. Zhang, J. Low Temp. Phys. **189**, 276 (2017).

[154] M. Udagawa and E. J. Bergholtz, Phys. Rev. Lett. **117**, 086401 (2016).

[155] A. A. Zyuzin and R. P. Tiwari, JETP Lett. **103**, 717 (2016).

[156] M. Koshino, Phys. Rev. B **94**, 035202 (2016).

[157] T. E. O. Brien, M. Diez, and C. W. J. Beenakker, Phys. Rev. Lett. **116**, 236401 (2016).

[158] P. Goswami and A. H. Nevidomskyy, Phys. Rev. B **92**, 214504 (2015).

[159] U. K. Rössler, A. N. Bogdanov, and C. Pfleiderer, Nature **442**, 797 (2006).

[160] N. Nagaosa and Y. Tokura, Nat. Nanotechnol. **8**, 899 (2013).

[161] M. Stone, Phys. Rev. B **53**, 16573 (1996).

[162] F. Jonietz, S. Mühlbauer, C. Pfleiderer, A. Neubauer, W. Münzer, A. Bauer, T. Adams, R. Georgii, P. Böni, R. A. Duine, K. Everschor, M. Garst, and A. Rosch, Science **330**, 1648 (2010).

[163] X. Yu, N. Kanazawa, W. Zhang, T. Nagai, T. Hara, K. Kimoto, Y. Matsui, Y. Onose, and Y. Tokura, Nat. Commun. **3**, 988 (2012).

[164] J. Iwasaki, M. Mochizuki, and N. Nagaosa, Nat. Nanotechnol. **8**, 742 (2013).

[165] A. Fert, V. Cros, and J. Sampaio, Nat. Nanotechnol. **8**, 152 (2013).

[166] S.-Z. Lin, C. Reichhardt, C. D. Batista, and A. Saxena, Phys. Rev. B **87**, 214419 (2013).

[167] C. Schutte, J. Iwasaki, A. Rosch, and N. Nagaosa, Phys. Rev. B **90**, 174434 (2014).

[168] J. Slonczewski, J. Magn. Magn. Mater. **195**, L261 (1999).

[169] L. Berger, Phys. Rev. B **59**, 11465 (1999).

[170] A. V. Khvalkovskiy, V. Cros, D. Apalkov, V. Nikitin, M. Krounbi, K. A. Zvezdin, A. Anane, J. Grollier, and A. Fert, Phys. Rev. B **87**, 020402 (2013).

[171] K. M. D. Hals and A. Brataas, Phys. Rev. B **87**, 174409 (2013).

[172] K. M. D. Hals and A. Brataas, Phys. Rev. B **89**, 064426 (2014).

[173] K. Maki, Prog. Theor. Phys. **29**, 333 (1963).

[174] V. M. Edelstein, Phys. Rev. Lett. **75**, 2004 (1995).

[175] T. Schulz, R. Ritz, A. Bauer, M. Halder, M. Wagner, C. Franz, C. Pfleiderer, K. Everschor, M. Garst, and A. Rosch, Nat. Phys. **8**, 301 (2012).

[176] J. D. Sau, R. M. Lutchyn, S. Tewari, and S. Das Sarma, Phys. Rev. Lett. **104**, 040502 (2010).

[177] R. Combescot and T. Dombre, Phys. Rev. B **33**, 79 (1986).

[178] G. Volovik, Phys. B Condens. Matter **255**, 86 (1998).

[179] T. D. C. Bevan, A. J. Manninen, J. B. Cook, J. R. Hook, H. E. Hall, T. Vachaspati, and G. E. Volovik, Nature **386**, 689 (1997).

[180] P. M. R. Brydon, B. Kastening, D. K. Morr, and D. Manske, Phys. Rev. B **77**, 104504 (2008).

[181] R. Takashima, S. Fujimoto, and T. Yokoyama, Phys. Rev. B **96**, 121203 (2017).

[182] J. Alicea, Phys. Rev. B **81**, 125318 (2010).

[183] H. Ohno, D. Chiba, F. Matsukura, T. Omiya, E. Abe, T. Dietl, Y. Ohno, and K. Ohtani, Nature **408**, 944 (2000).

[184] T. Lottermoser, T. Lonkai, U. Amann, D. Hohlwein, J. Ihringer, and M. Fiebig, Nature **430**, 541 (2004).

[185] C. D. Stanciu, F. Hansteen, A. V. Kimel, A. Kirilyuk, A. Tsukamoto, A. Itoh, and T. Rasing, Phys. Rev. Lett. **99**, 047601 (2007).

[186] I. Radu, K. Vahaplar, C. Stamm, T. Kachel, N. Pontius, H. A. Dürr, T. A. Ostler, J. Barker, R. F. L. Evans, R. W. Chantrell, A. Tsukamoto, A. Itoh, A. Kirilyuk, T. Rasing, and A. V. Kimel, Nature **472**, 205 (2011).

[187] L. N. Bulaevskii and S. V. Panjukov, J. Low Temp. Phys. **52**, 137 (1983).

[188] L. N. Bulaevskii and A. I. Buzdin, Adv. Phys. **34**, 175 (1985).

[189] P. W. Anderson and H. Suhl, Phys. Rev. **116**, 898 (1959).

[190] R. Ozawa, S. Hayami, K. Barros, G.-W. Chern, Y. Motome, and C. D. Batista, J. Phys. Soc. Jpn **85**, 103703 (2016).

[191] M. Tinkham, *Introduction to superconductivity* (McGraw-Hill, New York, 1996).

[192] M. Xu, H. Kitazawa, Y. Takano, J. Ye, K. Nishida, H. Abe, A. Matsushita, N. Tsujii, G. Kido, M. Xu, H. Kitazawa, Y. Takano, J. Ye, K. Nishida, H. Abe, A. Matsushita, and N. Tsujii, Appl. Phys. Lett. **79**, 2779 (2001).

[193] N. Kanazawa, Y. Onose, T. Arima, D. Okuyama, K. Ohoyama, S. Wakimoto, K. Kakurai, S. Ishiwata, and Y. Tokura, Phys. Rev. Lett. **106**, 156603 (2011).

[194] M. Mochizuki, Phys. Rev. Lett. **108**, 017601 (2012).

[195] N. Romming, C. Hanneken, M. Menzel, J. E. Bickel, B. Wolter, K. von Bergmann, A. Kubetzka, and R. Wiesendanger, Science **341**, 636 (2013).

[196] J. Sampaio, V. Cros, S. Rohart, A. Thiaville, and A. Fert, Nat. Nanotechnol. **8**, 839 (2013).

[197] S. Heinze, K. von Bergmann, M. Menzel, J. Brede, A. Kubetzka, R. Wiesendanger, G. Bihlmayer, and S. Blügel, Nat. Phys. **7**, 713 (2011).

[198] S. Z. Lin and S. Hayami, Phys. Rev. B **93**, 064430 (2016).

[199] A. Tonomura, X. Yu, K. Yanagisawa, T. Matsuda, Y. Onose, N. Kanazawa, H. S. Park, and Y. Tokura, Nano Lett. **12**, 1673 (2012).

[200] P. G. de Gennes, *Fluctuations, Instabilities, and Phase Transitions*, edited by T. Riste (1975).

[201] U. K. Rößler, A. a. Leonov, and A. N. Bogdanov, J. Phys. Conf. Ser. **303**, 012105 (2011).

[202] P. G. Harper, Proc. Phys. Soc. Sect. A **68**, 874 (1955).

[203] D. R. Hofstadter, Phys. Rev. B **14**, 2239 (1976).

[204] S. A. Diaz and D. P. Arovas, arXiv:1604.04010 .

[205] N. Usov, Zh. Eksp. Teor. Fiz **94**, 305 (1988).

[206] D. Pfannkuche and R. R. Gerhardts, Phys. Rev. B **46**, 12606 (1992).

Acknowledgment

I would like to express my sincere gratitude to Prof. Satoshi Fujimoto, for the continuous support and invaluable discussions during the entire graduate course. His deep understanding of condensed matter physics and insightful suggestions have always inspired me, and I have learned a lot of things from him. I would also like to thank Prof. Norio Kawakami for his supervision and warm support. He has continuously encouraged and supported me during my graduate course. I am also very grateful to Prof. Yoichi Yanase for the collaboration and insightful discussions. I have obtained a vast knowledge from the discussions with him and meetings organized by him.

During my doctoral course, I have had great mentors outside Kyoto University. I am really indebted and thankful to Prof. Leon Balents, who welcomed me during one year at the Kavli Institute for Theoretical Physics (KITP) in Santa Barabara. He had warmly supported me during my stay in Santa Barbara, and I have enjoyed many stimulating discussions with him. Similarly, I am very grateful to Prof. Yukitoshi Motome, who welcomed me at the University of Tokyo. His enthusiasm for physics has stimulated me, and I was encouraged by his kind and earnest support many times.

I have learned many things from the collaborators. I would like to thank Dr. Takehito Yokoyama for invaluable discussions. Discussions with him deepen my understanding, and I learned lots of knowledge of the superconducting proximity effects from him. I am also grateful to Dr. Yuki Shiomi for collaborations on experiments and discussions. I learned various knowledge from him, and I always enjoy working with him. I would also like to thank Dr. Hiroaki Ishizuka for insightful discussions, patience and kind support in Santa Barabara. I am also grateful to Dr. Yasuyuki Kato for invaluable discussions and the hospitality at the University of Tokyo.

I would like to thank the faculty at Kyoto University, especially, Prof. Ryusuke Ikeda, Prof. Kenji Ishida, Prof. Yoshiteru Maeno, Prof. Masatoshi Sato, Prof. Yuji Matsuda, Dr. Masaki Tezuka, and Dr. Robert Peters, for the invaluable discussions and kind support in many occasions. I would also like to thank my great colleagues. I am grateful to Dr. Tsuneya Yoshida, Dr. Ken Shiozaki, Dr. Takuya Nomoto, Dr. Masaya Nakagawa, Dr. Hiroaki Sumiyoshi, Dr. Jun Ishizuka, Dr. Benedikt Lechtenberg, Mr. Fuyuki Matsuda, Mr. Kyosuke Adachi, Mr. Yuichiro Dan, Mr. Kazuaki Takasan, Mr. Akito Daido, Mr. Shuntaro Sumita, Mr. Yohei Ibe, Mr. Hikaru Watanabe, and other members in the condensed matter theory group at Kyoto University. I would also like to acknowledge the great hospitality and very inspiring atmosphere at KITP and the University of Tokyo. I am grateful to Dr. Jianpeng Liu, Dr. Louk Rademaker, Dr. Gabriel Wong, and other people at KITP and University of California in Santa Barbara. Similarly, I would also like to thank Dr. Ryo Ozawa, Dr. Ken Okada, Mr. Junki Yoshitake, Mr. Yusuke Sugita, Mr. Petr Mishchenko, Mr. Shun Okumura, Mr. Ryoya Sano and other members in Prof. Motome's group.

I appreciate financial support from the Japan Society for the Promotion of Science and the Kavli Institute for Theoretical Physics.

Finally, I would like to express my gratitude to my parents Katsuyoshi Takashima and Tamami Takashima for their continuous support and encouragement.